

**Big Bang Leftovers in the Microwave:
Cosmology with the Cosmic Microwave Background Radiation**

by

Eric Joseph Gawiser

A.B. (Princeton University) 1994

M.A. (University of California, Berkeley) 1996

A dissertation submitted in partial satisfaction of the
requirements for the degree of
Doctor of Philosophy

in

Physics

in the

GRADUATE DIVISION

of the

UNIVERSITY of CALIFORNIA at BERKELEY

Committee in charge:

Professor Joseph Silk, Chair
Professor George F. Smoot
Professor Thomas Broadhurst

Spring 1999

**Big Bang Leftovers in the Microwave:
Cosmology with the Cosmic Microwave Background Radiation**

Copyright Spring 1999

by

Eric Joseph Gawiser

Abstract

Big Bang Leftovers in the Microwave:
Cosmology with the Cosmic Microwave Background Radiation

by

Eric Joseph Gawiser

Doctor of Philosophy in Physics

University of California at Berkeley

Professor Joseph Silk, Chair

We combine detections of anisotropy in the Cosmic Microwave Background radiation with observations of inhomogeneity in the large-scale distribution of galaxies to test the predictions of models of cosmological structure formation. This combination probes spatial scales varying by three orders of magnitude, including a significant region where the two types of data overlap. We examine Cold Dark Matter models with adiabatic density perturbations, isocurvature models, and a topological defects model. We set upper limits on the neutrino mass and find the primordial power spectrum needed to reconcile an apparent disagreement between structure formation observations and direct observations of cosmological parameters.

Present and future observations of Cosmic Microwave Background anisotropy suffer from foreground contamination. We develop detailed predictions for microwave emission from radio and infrared-bright galaxies and the Sunyaev-Zeldovich effect from clusters. We present realistic simulations of the microwave sky, produced as part of the “WOMBAT Challenge” exercise, and introduce a pixel-space method for subtracting foreground contamination which can be tested on these simulations.

To everyone who has ever gazed at the sky and wondered how it all began: Do not fear. This dissertation will leave you with plenty still to wonder about!

Contents

List of Figures	vii
List of Tables	x
I Testing Models of Cosmological Structure Formation	1
1 Introduction: An Overview of Cosmic Microwave Background Anisotropy	2
1.1 Motivation of this Thesis	2
1.2 Origin of the Cosmic Background Radiation	4
1.2.1 Thermalization	6
1.3 CMB Spectrum	8
1.4 CMB Anisotropy	10
1.4.1 Reionization	12
1.4.2 Secondary Anisotropies	12
1.4.3 Polarization Anisotropies	13
1.4.4 Gaussianity of the CMB anisotropies	13
1.4.5 Foreground contamination	14
2 Current Status of Observations	15
2.1 Cosmic Microwave Background Anisotropy Observations	15
2.1.1 Window Functions	17
2.1.2 Sample and Cosmic Variance	18
2.2 Observations of Large-Scale Structure	19
2.3 Direct Observations of Cosmological Parameters	22
2.4 Sample Variance of Cosmological Surveys	23
3 Models Tested and Methodology	27
3.1 Structure Formation Models	27
3.1.1 Standard Cold Dark Matter And Its Variants	28
3.1.2 Isocurvature Models	30
3.1.3 Topological Defect Models	30
3.2 Comparison with Observations	31
3.2.1 Cosmic Microwave Background Anisotropy Detections	32

3.2.2	Observations of Large-Scale Structure	33
4	Results	41
4.1	Goodness of Fit	41
4.2	Evaluating the Models	42
4.3	Discussion	46
5	Cosmological Limits on the Neutrino Mass	59
5.1	Is Cold+Hot Dark Matter Compatible with a Cosmological Constant? . . .	59
5.2	Limits on the Neutrino Mass	60
6	Reconstructing the Primordial Power Spectrum	65
6.1	Motivation	65
6.2	Methodology	66
6.3	Discussion	67
6.4	The Primordial Power Ratio	68
II	Making Realistic Simulations of the Microwave Sky	78
7	The WOMBAT Challenge	79
7.1	Motivation	79
7.2	Microwave Foregrounds	80
7.3	Reducing Foreground Contamination	83
7.4	The WOMBAT Challenge Simulations	86
7.4.1	Constrained Realizations of CMB Anisotropy	87
7.4.2	Instrument Noise and Beam Convolution	87
7.4.3	Galactic foregrounds	88
7.4.4	Extragalactic foregrounds	89
7.5	A “Hounds and Hares” Exercise for Cosmology	91
7.6	Discussion	92
8	Low-redshift Infrared Galaxies	98
8.1	Motivation	98
8.2	Extragalactic Infrared Sources	99
8.3	Results	103
8.4	Discussion	107
9	Radio Galaxies	110
9.1	Motivation	110
9.2	Our Catalog	111
9.3	Spectral Fitting	111
9.4	Results	115
9.5	Improving Sky Coverage with the PMN Survey	117
9.6	Discussion	119

10	Observational Limits on Anisotropy from Point Sources	123
10.1	Motivation	123
10.2	Extragalactic Point Sources	125
10.3	Analysis	126
10.4	Results	128
10.5	Discussion	133
11	The Sunyaev-Zeldovich Effect	136
11.1	Theory	136
11.2	Simulations	137
12	A Pixel-space Method for Foreground Subtraction	143
12.1	Motivation	143
12.2	Cross-correlation of Foreground Templates	146
12.3	Testing for a Thermodynamic Spectrum	147
13	Conclusion	151
13.1	Prospects for Detecting Dusty High-Redshift Galaxies	151
13.2	Future Constraints on Structure Formation Models	152
13.3	Conclusions	153

List of Figures

1.1	Measurements of the CMB spectrum.	8
2.1	Compilation of CMB anisotropy observations.	25
2.2	Compilation of large-scale structure observations.	26
3.1	CMB anisotropy observations shown with SCDM power spectrum.	37
3.2	Compilation of large-scale structure observations with SCDM $P(k)$	38
3.3	SCDM compared to CMB and LSS data, after the LSS data have been corrected for redshift distortions, but not yet for non-linear evolution. This represents our reconstruction of the real-space non-linear power spectra, but it is compared with the linear theory prediction for the SCDM power spectrum.	39
3.4	The SCDM model compared to the data, which has undergone model-dependent corrections for redshift distortions, bias, and non-linear evolution. Beyond $k = 0.2$, the predicted matter power spectrum curve is dotted to indicate uncertainty in the data corrections.	40
4.1	Compilation of CMB anisotropy results compared to model C_ℓ	48
4.2	The Tilted CDM model compared with CMB and LSS data.	49
4.3	CHDM, our best-fit model. Note agreement even on non-linear scales.	50
4.4	Constraints from LSS and CMB on CHDM model expanded in region of highest precision LSS data near $k = 0.1$. The location and shape of the peak in the matter power spectrum and the steepness of its falloff towards higher k are the features that make this model by far the best fit to the data of those we have tested.	51
4.5	Constraints from LSS and CMB on the Open CDM model, with scale-invariance of potential perturbations causing an increase in the matter power spectrum beyond the curvature scale.	52
4.6	Constraints from LSS and CMB on Λ CDM model.	53
4.7	Constraints from LSS and CMB on ϕ CDM model.	54
4.8	The BCDM model. Note the poor agreement at the main peak of the power spectrum.	55
4.9	Constraints from LSS and CMB on Isocurvature CDM model.	56
4.10	Constraints from LSS and CMB on PBH BDM model.	57

4.11	Strings + Λ CDM. Notice the deficit of power versus the bias-independent observations at $k = 0.1$	58
5.1	Constraints from LSS and CMB on Λ CDM model.	62
5.2	Λ CDM model with $\Omega_\nu = 0.05$	63
5.3	Λ CDM model with $\Omega_\nu = 0.10$ and $n = 1.5$	64
6.1	Detailed constraints from LSS and CMB on Λ CDM model showing apparent misplacement of peak in the matter power spectrum.	70
6.2	Constraints from LSS and CMB on Λ CDM model with a broad enhancement centered at $k = 0.06h^{-1}\text{Mpc}$ added to the primordial power spectrum.	71
6.3	Detailed constraints from the peak of the matter power spectrum on Λ CDM model with a broad enhancement centered at $k = 0.06h^{-1}\text{Mpc}$ added to the primordial power spectrum.	72
6.4	Constraints from LSS and CMB on Tilted Λ CHDM model with a broad enhancement centered at $k = 0.06h^{-1}\text{Mpc}$ added to the primordial power spectrum.	73
6.5	Constraints from CMB on tilted Λ CHDM + BUMP models.	74
6.6	Primordial power constraints from LSS and CMB for SCDM model. The solid line is a scale-invariant primordial power spectrum, $n = 1$	75
6.7	Primordial power constraints from LSS and CMB for CHDM model.	76
6.8	Primordial power constraints from LSS and CMB for a high baryon-fraction model similar to BCDM.	77
7.1	Frequency spectra of microwave foregrounds.	83
7.2	Simulated CMB component for MAP 40 GHz channel with 28' FWHM.	94
7.3	Simulated Galactic and extragalactic foregrounds for MAP 40 GHz channel with 28' FWHM.	95
7.4	A realistic simulation of the microwave sky for MAP 40 GHz channel with 28' FWHM.	96
7.5	WOMBAT Challenge simulation of a MAXIMA dataset at 150 GHz, 11' FWHM, $10^\circ \times 10^\circ$	97
8.1	Galactic Far-IR Emission Spectrum	101
8.2	Microwave anisotropy from low-redshift infrared galaxies.	104
8.3	Confusion from low-redshift infrared galaxies	106
8.4	Skymap at 100 GHz of predicted contribution from IRAS 1.2 Jy sources.	109
9.1	Spectral indices α_1 from 1.4 to 10 GHz and α_2 from 10 to 90 GHz. Solid circles represent the brightest sources at 1.4 GHz; open squares represent dimmer sources at 1.4 GHz. Note the lack of clustering into distinct archetypal spectra.	112
9.2	Microwave anisotropy from radio sources	120
9.3	Plot of predicted $\log(\ell(\ell+1)C_\ell)$ vs. $\log_{10}\ell$ for the radio catalog extrapolated to 100 GHz and pixelized at HEALPIX level 1024 (3.4' pixels).	121

9.4	Sky map in Galactic coordinates of our catalog of radio sources (including PMN) extrapolated to 100 GHz and pixelized at HEALPIX level 128 ($0^{\circ}5$). The color table (in units of thermodynamic temperature fluctuations) reaches a maximum for all sources which will be directly detectable by future satellites.	122
10.1	Limits on flux anisotropy.	129
10.2	Limits on temperature anisotropy.	130
10.3	Net upper (solid line) and lower (dotted line) limits for $10'$ and 1°	134
11.1	Predicted SZ angular power spectra.	139
11.2	Angular power spectra from SZ effect in filaments and clusters.	140
11.3	Predicted temperature fluctuations at 90 GHz from filaments extending from and connecting XBACS clusters using the toy model described in the text.	141
11.4	Combined prediction of the SZ effect from XBACS clusters and a simulation of the filamentary structure connecting them.	142
12.1	C_{ℓ} for one of the WOMBAT Challenge simulations measured at $ b > 30$ compared to the expected C_{ℓ} for Λ CDM.	144
12.2	C_{ℓ} for 3 different WOMBAT Challenge simulations, measured at $ b > 30$ with 5σ pixels subtracted.	145
13.1	Prospects for submillimeter detection of high-redshift galaxies.	154
13.2	Simulation of high-precision future structure formation constraints.	155

List of Tables

- 3.1 Values of cosmological parameters for our models. 28
- 4.1 Best-fit normalizations and biases. The normalization of each model is given by σ_8 or the value of dT at $\ell = 10$, which can be compared to the COBE normalization of $dT = 27.9\mu\text{K}$ 42
- 4.2 Chi-squared values for our models. 43
- 9.1 Average Errors from Extrapolation. The average extrapolation error is the mean of $|(S_P - S_O)/S_P|$ where S_P is the predicted flux and S_O is the observation. The average error factor is the mean of S_P/S_0 114
- 9.2 Foreground Anisotropy in MAP & Planck channels after source removal. Sources which contribute to the anisotropies at the 5σ level or higher are considered detected and are removed by masking the pixels containing them. No attempt has been made to use multi-frequency information or further prior information to detect and remove dimmer sources. 117
- 9.3 Foreground Contamination in 13' MAP channel at 90 GHz. This analysis assumes that our catalog is used to identify sources whose fluxes will be above the threshold and that the pixels containing those sources are masked. The results given are for the northern celestial hemisphere, where our catalog is estimated to be complete for the brightest few hundred sources, so the final line is likely an underestimate of anisotropy. 118
- 10.1 Noise levels in high-resolution microwave observations. 131
- 10.2 Microwave source detections. 132

Acknowledgements

This research would not have been possible without the tireless efforts of hundreds of observers who gathered and analyzed the raw data on cosmological inhomogeneity and anisotropy. I have benefitted from discussions with dozens of researchers in person and by email and have tried to acknowledge their help in my published work. In particular, I want to thank Martin White, Helen Tadros, and Carlton Baugh for their patient and thorough responses to my email questions. Kris Gorski, Eric Hivon, and Ben Wandelt (HEALPIX) and Uros Seljak and Matias Zaldarriaga (CMBFAST) deserve tremendous credit for making their high-tech software packages available to the cosmology community.

I am grateful for research support from a variety of sources: an NSF Graduate Fellowship, the NASA AISRP grant (NAG-3941), a Phi Beta Kappa fellowship, a Department of Education-GANN fellowship, and a summer NASA grant. I want to acknowledge my co-authors (Joe Silk, George Smoot, Aaron Sokasian, Andrew Jaffe, and the WOMBAT Team) since much of the material contained herein is a mild modification of multiple-author works submitted for publication. I appreciate comments from Doug Finkbeiner and Andrew Jaffe that improved the material in Chapter 12. I thank Ted Bunn, Luis Tenorio, and Philip Stark for being my resources on statistics issues.

My advisor, Joe Silk, has been a tremendous supporter of my research efforts and has given me opportunities to travel widely through various fields of cosmology, both literally and figuratively. George Smoot got me started in the microwave foregrounds business the summer before graduate school; little did I know how much that field would grow! I owe a great debt to my officemates, Doug Finkbeiner, Lexi Moustakas, and Jeff Newman, for putting up with my whistling and yelling at the computer screen (it's all part of the creative process!) and for giving me so much remedial help with UNIX and IDL. I thank my parents for understanding that I really **was** working hard on my dissertation, but I didn't necessarily feel like discussing it. And for my sweetie: Sevil çok ama en çok seviyorum!

Part I

Testing Models of Cosmological Structure Formation

Chapter 1

Introduction: An Overview of Cosmic Microwave Background Anisotropy

1.1 Motivation of this Thesis

The Cosmological Principle holds that the universe is homogeneous and isotropic, i.e. that it looks roughly the same at every point and in every direction. We know that this holds true for the Cosmic Microwave Background (CMB) radiation, which has uniform intensity to a level of one part in one hundred thousand in every direction on the sky and is described in detail in the rest of this chapter. We believe that this is true for the distribution of galaxies as well, with each large-scale region of the universe containing a similar mix of galaxies and galaxy clusters. However, we have abundant evidence that the Cosmological Principle is not absolute: our very existence requires a highly inhomogeneous distribution of matter on small scales, in order to form galaxies and then stars and then planets containing the relatively heavy elements such as carbon and oxygen which are so critical for life as we know it. The average density of the universe is enough to have only a few hydrogen atoms per cubic meter, so everything that makes up our daily world is an aberration. On the larger scale, we can readily observe that galaxies are clustered at a level much greater than a Poissonian distribution would suggest and that these clusters are themselves clustered into superclusters of galaxies. This implies that density variations on very large scales existed

in the early universe.

Such density variations are most directly probed using the Cosmic Microwave Background radiation. Indeed, anisotropy (variation from one position on the sky to another) has now been seen in the CMB on scales corresponding to present-day superclusters. We believe that the formation of structure in the universe is described by the paradigm of gravitational instability, which states that sufficiently overdense regions overwhelm the universal expansion and collapse to form galaxies and clusters while underdense regions expand to form voids. Given the approximately 15 billion years since the Big Bang, gravity has been able to magnify density variations seen in the CMB at one part in a hundred thousand to the level needed to form galaxies today.

This connection between slight inhomogeneities in the early universe, seen as slight anisotropies in the CMB, and the clear inhomogeneity in the galaxy distribution today is the motivation for Part I of this thesis. We compile the current set of observations of CMB anisotropy and the large-scale structure of the galaxy distribution (Chapter 2). A careful method is presented for comparing these observations with the predictions of various models of cosmological structure formation (Chapter 3). The data are improving rapidly but the list of models which can be considered is growing even faster. For this reason, we do not attempt an exhaustive search of a particular parameter space but rather examine the most popular models and a few exotic ones in order to gain insight into what aspects are well constrained by observation (Chapter 4, see also Gawiser & Silk 1998). This allows us to identify two aspects for further analysis, the possibility of cosmologically significant neutrino mass (Chapter 5) and the possibility of a non-scale-free primordial power spectrum (Chapter 6).

While we attempt to correct for known systematic issues in the large-scale structure observations in Part I, the field of CMB anisotropy observation is still in its infancy, and so far there is no proof of systematic corrections needed for the data. The most likely source of such difficulties is foreground contamination due to Galactic and extragalactic microwave emission. Foreground contamination has been subtracted in a very primitive manner by most observing teams, and for the low level of precision of current observations this may be sufficient. However, the 1% level of precision in cosmological parameter estimation which is desired for future CMB observations will not allow for much error in foreground subtraction. In Part II, we describe the “WOMBAT Challenge” exercise (Chapter 7, see also Gawiser et al. 1998), which seeks to make realistic simulations of the microwave sky and test methods

of foreground subtraction. We describe detailed studies of how to predict the contribution to microwave anisotropy from low-redshift infrared-bright galaxies (Chapter 8, see also Gawiser & Smoot 1997) and radio galaxies (Chapter 9, see also Sokasian et al. 1998) and set limits on the level of foreground contamination which can be caused by high-redshift infrared-bright galaxies, dim radio sources, and undiscovered families of point sources (Chapter 10, see also Gawiser et al. 1998). We also give predictions for microwave anisotropy caused by the Sunyaev-Zeldovich effect in galaxy clusters and the filaments connecting them (Chapter 11) and present a pixel-space method for foreground subtraction which can be tested on the WOMBAT simulations (Chapter 12). As the quantity and quality of data are expected to improve rapidly in the coming decade, we will examine the prospects for detecting dusty high-redshift galaxies with forthcoming instruments and for setting improved constraints on models of structure formation and then conclude (Chapter 13). The rest of this chapter sets the stage by providing an overview of Cosmic Microwave Background anisotropy.

1.2 Origin of the Cosmic Background Radiation

Our present understanding of the beginning of the universe is based upon the remarkably successful theory of the Hot Big Bang. We believe that our universe began about 15 billion years ago at a minute fraction of its present size (formally an infinitesimal singularity) as a hot, dense, nearly uniform sea of radiation. If inflation occurred in the first fraction of a second, the universe became matter dominated while expanding exponentially and then returned to radiation domination by the reheating caused by the decay of the inflaton. Baryonic matter formed within the first second, and the nucleosynthesis of the lightest elements took only a few minutes as the universe expanded and cooled. The majority of the baryonic matter in the universe was in the form of plasma until about 300,000 years after the Big Bang, when the universe had cooled to a temperature of about 3000 K, sufficiently cool for protons to capture free electrons and form atomic hydrogen; this process is referred to as recombination. The recombination epoch occurred at an observed redshift of about 1100, meaning the universe is now over a thousand times larger than it was then. The ionization energy of a hydrogen atom is 13.6 eV, but recombination did not occur until the universe had cooled to a characteristic temperature (kT) of 0.3 eV (Padmanabhan 1993). This delay had several causes. The high entropy of the universe makes the rate of electron capture only marginally faster than the rate of photodissociation.

Moreover, each electron captured directly into the ground state emits a photon capable of ionizing another newly formed atom, so it was through recombination into excited states and the cooling of the universe to temperatures below the ionization energy of hydrogen that neutral matter finally condensed out of the plasma. Until recombination, the universe was opaque to electromagnetic radiation due to scattering of the photons by free electrons. As recombination occurred, the density of free electrons diminished greatly, leading to the decoupling of matter and radiation as the universe became transparent to light.

The Cosmic Background Radiation (CBR) released during this era of decoupling had a mean free path long enough to travel almost unperturbed until the present day, where we observe it peaked in the microwave region of the spectrum as the Cosmic Microwave Background (CMB). We see this radiation today coming from the surface of last scattering (which is really a spherical shell of finite thickness) at a distance of 15 billion light years. This Cosmic Background Radiation was predicted by the Hot Big Bang theory and discovered with an antenna temperature of 3K in 1964 by Penzias & Wilson (1965). Because of the expansion of the universe, each epoch in its history is observed today at a redshift which increases with the age of the epoch. The number density of photons in the universe at a redshift z is given by (Peebles 1993)

$$n_\gamma = 420(1+z)^3 \text{ cm}^{-3} \quad (1.1)$$

where $(1+z)$ is the factor by which the linear scale of the universe has expanded since then. The radiation temperature of the universe is given by $T = T_0(1+z)$ so it is easy to see how the conditions in the early universe at high redshifts were hot and dense.

The CBR is our best probe into the conditions of the early universe. Theories of the formation of large-scale structure predict the existence of slight inhomogeneities in the distribution of matter in the early universe which eventually underwent gravitational collapse to form galaxies, galaxy clusters, and superclusters. These density inhomogeneities lead to temperature anisotropies in the CBR because the radiation leaving a dense area of the last scattering surface is gravitationally redshifted to a lower apparent temperature and vice versa for an underdense region. The DMR (Differential Microwave Radiometer) instrument of the Cosmic Background Explorer (COBE) satellite discovered primordial temperature fluctuations on angular scales larger than 7° of order $\Delta T/T = 10^{-5}$ (Smoot et al. 1992). The subsequent observations of the CMB appear to reveal temperature anisotropies

on smaller angular scales which correspond to the physical scale of observed structures such as galaxies and clusters of galaxies.

1.2.1 Thermalization

There were three main processes by which this radiation interacted with matter in the first few hundred thousand years, Compton scattering, double Compton scattering, and thermal bremsstrahlung. The simplest interaction of matter and radiation is Compton scattering of a single photon off a free electron, $\gamma + e^- \rightarrow \gamma + e^-$. The photon will transfer momentum and energy to the electron if it has significant energy in the electron's rest frame. However, the scattering will be well approximated by the Thomson cross section if the photon's energy in the rest frame of the electron is significantly less than the rest mass, $h\nu \ll m_e c^2$. When the electron is relativistic, the photon is blueshifted by roughly a factor γ in energy when viewed from the electron rest frame, is then emitted at almost the same energy in the electron rest frame, and is blueshifted by another factor of γ when retransformed to the observer's frame. Thus, energetic electrons can efficiently transfer energy to the photon background of the universe. This process is referred to as Inverse Compton scattering. The combination of cases where the photon gives energy to the electron and vice versa allows Compton scattering to generate thermal equilibrium (which is impossible in the Thomson limit of elastic scattering). Compton scattering conserves the number of photons. There exists a similar process, double Compton scattering, which produces (or absorbs) photons, $e^- + \gamma \leftrightarrow e^- + \gamma + \gamma$.

Another electromagnetic interaction which occurs in the plasma of the early universe is Coulomb scattering. Coulomb scattering itself serves to establish and maintain thermal equilibrium within the photon-baryon fluid but does not affect the photons. However, when electrons encounter ions they experience an acceleration and therefore emit electromagnetic radiation. This is called thermal bremsstrahlung or free-free emission. For an ion X , we have $e^- + X \leftrightarrow e^- + X + \gamma$. The interaction can occur in reverse because of the ability of the charged particles to absorb incoming photons; this is called free-free absorption. Each charged particle emits radiation, but the acceleration is proportional to the mass, so we can usually view the electron as being accelerated in the fixed Coulomb field of the much heavier ion. Bremsstrahlung is dominated by electric-dipole radiation (Shu 1991) and can also produce and absorb photons.

The net effect is that Compton scattering is dominant for temperatures above 90 eV whereas bremsstrahlung is the primary process between 90 eV and 1 eV. At temperatures above 1 keV, double Compton is more efficient than bremsstrahlung. All three processes occur faster than the expansion of the universe and therefore have an impact until decoupling. A static solution for Compton scattering is the Bose-Einstein distribution,

$$f_{BE} = \frac{1}{e^{x+\mu} - 1} \quad (1.2)$$

where μ is a dimensionless chemical potential (Hu 1995). At high optical depths, Compton scattering can exchange enough energy to bring the photons to this Bose-Einstein equilibrium distribution. A Planckian spectrum corresponds to zero chemical potential, which will occur only when the number of photons and total energy are in the same proportion as they would be for a blackbody. Thus, unless the photon number starts out exactly right in comparison to the total energy in radiation in the universe, Compton scattering will only produce a Bose-Einstein distribution and not a blackbody spectrum. It is important to note, however, that Compton scattering can preserve a Planck distribution, which is given by

$$f_P = \frac{1}{e^x - 1}. \quad (1.3)$$

All three interactions will preserve a thermal spectrum if one is achieved at any point. It has long been known that the expansion of the universe serves to decrease the temperature of a blackbody spectrum,

$$B_\nu = \frac{2h\nu^3/c^2}{e^{h\nu/kT} - 1}, \quad (1.4)$$

but keeps it thermal (Tolman 1934). This occurs because both the frequency and temperature decrease as $(1+z)$ leaving the scaled variable x unchanged during expansion. Although Compton scattering alone cannot produce a Planck distribution, such a distribution will remain unaffected by electromagnetic interactions or the universal expansion once it is achieved. A non-zero chemical potential will be reduced to zero by double Compton scattering and, later, bremsstrahlung which will create and absorb photons until the number density matches the energy and a thermal distribution of zero chemical potential is achieved. This results in the thermalization of the CBR at redshifts much greater than that of recombination.

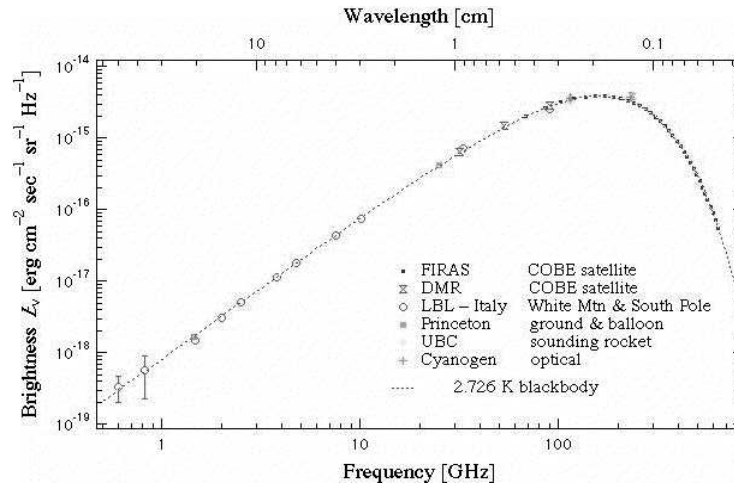


Figure 1.1: Measurements of the CMB spectrum.

Thermalization, of course, should only be able to create an equilibrium temperature over regions that are in causal contact. The causal horizon at the time of last scattering was relatively small, corresponding to a scale today of about 200 Mpc, or a region of angular extent of one degree on the sky. However, observations of the CMB show that it has an isotropic temperature on the sky to the level of one part in one hundred thousand! This is the origin of the Horizon Problem, which is that there is no physical mechanism expected in the early universe which can produce thermodynamic equilibrium on superhorizon scales. The inflationary universe paradigm (Guth 1981; Linde 1982; Albrecht & Steinhardt 1982) solves the Horizon Problem by postulating that the universe underwent a brief phase of exponential expansion during the first second after the Big Bang, during which our entire visible Universe expanded out of a region small enough to have already achieved thermal equilibrium.

1.3 CMB Spectrum

The CBR is the most perfect blackbody ever seen, according to the FIRAS (Far InfraRed Absolute Spectrometer) instrument of COBE, which measured a temperature of $T_0 = 2.726 \pm 0.010 K$ (Mather et al. 1994). The theoretical prediction that the CBR will have a blackbody spectrum appears to be confirmed by the FIRAS observation (see Figure 1.1). But this is not the end of the story. FIRAS only observed the peak of the blackbody. Other

experiments have mapped out the Rayleigh-Jeans part of the spectrum at low frequency. Most are consistent with a 2.73 K blackbody, but some are not. It is in the low-frequency limit that the greatest spectral distortions might occur because a Bose-Einstein distribution differs from a Planck distribution there. However, double Compton and bremsstrahlung are most effective at low frequencies so strong deviations from a blackbody spectrum are not generally expected. Possible spectral distortions in the Wien tail of the spectrum would need to be very significant to be observed above the foreground signal from interstellar dust at those high frequencies. For example, broad emission lines from electron capture at recombination are predicted in the Wien tail but cannot be distinguished due to foreground contamination (White et al. 1994).

Although Compton, double Compton, and bremsstrahlung interactions occur frequently until decoupling, the complex interplay between them required to thermalize the CBR spectrum is ineffective at redshifts below 10^7 . This means that any process after that time which adds a significant portion of energy to the universe will lead to a spectral distortion today. Neutrino decays during this epoch should lead to a Bose-Einstein rather than a Planck distribution, and this allows the FIRAS observations to set constraints on the decay of neutrinos and other particles in the early universe (Kolb & Turner 1990). The apparent impossibility of thermalizing radiation at low redshift makes the blackbody nature of the CBR strong evidence that it did originate in the early universe and as a result serves to support the Big Bang theory.

The process of Compton scattering can cause spectral distortions if it is too late for double Compton and bremsstrahlung to be effective. In general, low-frequency photons will be shifted to higher frequencies, thereby decreasing the number of photons in the Rayleigh-Jeans region and enhancing the Wien tail. This is referred to as a Compton- y distortion and it is described by the parameter

$$y = \int \frac{T_e(t)}{m_e} \sigma n_e(t) dt. \quad (1.5)$$

The apparent temperature drop in the long-wavelength limit is

$$\frac{\delta T}{T} = -2y. \quad (1.6)$$

The most important example of this is Compton scattering of photons off hot electrons in galaxy clusters, called the Sunyaev-Zeldovich (SZ) effect. The electrons transfer energy

to the photons, and the spectral distortion results from the sum of all of the scatterings off electrons in thermal motion, each of which has a Doppler shift. The SZ effect from clusters can yield a distortion of $y \simeq 10^{-5} - 10^{-3}$ and these distortions have been observed in several rich clusters of galaxies. The FIRAS observations place a constraint on any full-sky Comptonization by limiting the average y -distortion to $y < 2.5 \times 10^{-5}$ (Hu 1995). The integrated y -distortion predicted from the SZ effect of galaxy clusters and large-scale structure is over a factor of ten lower than this observational constraint (Refregier et al. 1998) but that from “cocoon” of radio galaxies (Yamada et al. 1999) is of the same order.

1.4 CMB Anisotropy

The temperature anisotropy at a point on the sky (θ, ϕ) can be expressed in the basis of spherical harmonics as

$$\frac{\Delta T}{T}(\theta, \phi) = \sum_{\ell m} a_{\ell m} Y_{\ell m}(\theta, \phi). \quad (1.7)$$

A cosmological model predicts the amplitude of the $a_{\ell m}$ coefficients over an ensemble of universes (or an ensemble of observational points within one universe, if the universe is ergodic). The assumptions of rotational symmetry and Gaussianity allow us to express this ensemble average in terms of the multipoles C_ℓ as

$$\langle a_{\ell m}^* a_{\ell' m'} \rangle \equiv C_\ell \delta_{\ell' \ell} \delta_{m' m}. \quad (1.8)$$

The predictions of a cosmological model can be expressed in terms of C_ℓ alone if that model predicts a Gaussian distribution of density perturbations, in which case the $a_{\ell m}$ will have mean zero and variance C_ℓ .

The conventional wisdom in cosmology holds that the temperature anisotropies detected by COBE are the result of inhomogeneities in the distribution of matter at the epoch of decoupling. Because Compton scattering is an isotropic process in the electron rest frame, any primordial anisotropies (as opposed to inhomogeneities) should have been smoothed out before decoupling. This lends credence to the interpretation of the observed anisotropies as the result of density perturbations which seeded the formation of galaxies and clusters. The discovery of temperature anisotropies by COBE provides evidence that such density inhomogeneities existed in the early universe due to quantum fluctuations in the scalar field of inflation or to topological defects caused by a phase transition. Gravitational

collapse of these primordial density inhomogeneities appears to have formed the large-scale structures of galaxies, clusters, and superclusters that we observe today.

There are now a plethora of theoretical models which predict the development of a primordial power spectrum of density perturbations into the radiation power spectrum of microwave background anisotropies. These models differ in their explanation of the origin of density inhomogeneities (inflation or topological defects), the nature of the dark matter (hot, cold, baryonic, or a mixture of the three), the curvature of the universe (Ω), the value of the cosmological constant (Λ), the value of Hubble's constant ($H = 100h$ km/s/Mpc), and the possibility of reionization at some redshift z which wholly or partially erased temperature anisotropies in the CMB on scales smaller than the horizon size. Available data does not allow us to constrain all (or even most) of these parameters, so it is clear that in analyzing new CMB anisotropy data we should seek a model-independent approach.

Anisotropy measurements on small angular scales (0.1 to 1°) are expected to reveal the so-called first acoustic peak of the CMB power spectrum. This acoustic peak corresponds to the scale where acoustic oscillations of the photon-baryon fluid caused by primordial density inhomogeneities are just reaching their maximum amplitude at the surface of last scattering. Further acoustic peaks occur at scales that are reaching their second, third, fourth, etc. antinodes of oscillation. For a given model, the size and location of the first acoustic peak can yield information about Ω , the ratio of the density of the universe to the critical density needed to stop its expansion, and Ω_b , the fraction of this critical density which is contained in baryonic matter. A precise measurement of all three acoustic peaks can reveal information on the fraction of hot dark matter and even potentially the number of neutrino species (Dodelson et al. 1996). It seems reasonable to view the mapping of the acoustic peaks as a means of determining the nature of parameter space before going on to fitting cosmological parameters directly. The CMB anisotropy damping tail on arcminute scales, where the fluctuations are decreased due to photon diffusion (Silk 1967) and the finite thickness of the last-scattering surface, is a sensitive probe of cosmological parameters and has the potential to break degeneracies between models which explain the larger-scale anisotropies (Hu & White 1997b; Metcalf & Silk 1998).

1.4.1 Reionization

The possibility that post-decoupling interactions between ionized matter and the CBR have affected the anisotropies on scales smaller than those measured by COBE is of great significance for current experiments. Reionization is inevitable but its effect on anisotropies depends significantly on when it occurs (see Haimann & Knox 1999 for a review). Early reionization leads to a larger optical depth and therefore a greater damping of the anisotropy power spectrum due to the secondary scattering of CMB photons off of the newly free electrons. Attempts to measure the temperature anisotropy on angular scales of less than a degree which correspond to the size of galaxies could lead to a surprise; if the universe was reionized after recombination to the extent that the CBR was significantly scattered at redshifts less than 1100, the small-scale primordial anisotropies will have been washed out. On arc-minute scales, the interaction of photons with reionized matter is expected to have eliminated the primordial anisotropies and replaced them with smaller secondary anisotropies from this new surface of last scattering (the Ostriker-Vishniac effect and patchy reionization, see next section and White et al. 1994). To have an appreciable optical depth for photon-matter interaction, reionization cannot have occurred much later than a redshift of 20 (Padmanabhan 1993). Large-scale anisotropies such as those seen by COBE are not expected to be affected by reionization because they encompass regions of the universe which were not yet in causal contact even at the proposed time of reionization.

1.4.2 Secondary Anisotropies

Secondary CMB anisotropies occur when the photons of the Cosmic Microwave Background radiation are scattered after the original last-scattering surface (see Refregier 1999 for a review). The shape of the blackbody spectrum can be altered through inverse Compton scattering by the thermal Sunyaev-Zeldovich (SZ) effect (Sunyaev & Zeldovich 1972), which will be discussed in more detail in Chapter 11. The effective temperature of the blackbody can be shifted locally by a doppler shift from the peculiar velocity of the scattering medium (the kinetic SZ and Ostriker-Vishniac effects) as well as by passage through the changing gravitational potential caused by the collapse of nonlinear structure (the Rees-Sciama effect) or the onset of curvature or cosmological constant domination (the Integrated Sachs-Wolfe effect). Simulations have been made of the impact of patchy reionization (Aghanim et al. 1996; Knox et al. 1998; Gruzinov & Hu 1998; Peebles & Juszkievicz 1998).

The SZ effect itself is independent of redshift, so it can yield information on clusters at much higher redshift than does X-ray emission. However, nearly all clusters are unresolved for $10'$ resolution so higher-redshift clusters occupy less of the beam and therefore their SZ effect is in fact dimmer. In the $4.5'$ channels of Planck this will no longer be true, and SZ detection and subtraction becomes more challenging and potentially more fruitful as a probe of cluster abundance at high redshift. An additional secondary anisotropy is that caused by gravitational lensing (see e.g. Cayon et al. 1993, 1994; Metcalf & Silk 1997; Martinez-Gonzalez et al. 1997). Gravitational lensing imprints slight non-Gaussianity in the CMB which can be cross-correlated with large-scale structure templates (Suginohara et al. 1998) or perhaps analyzed directly to determine the matter power spectrum (Seljak & Zaldarriaga 1999; Zaldarriaga & Seljak 1998).

1.4.3 Polarization Anisotropies

Polarization of the Cosmic Microwave Background radiation (Kosowsky 1994; Kamionkowski et al. 1997; Zaldarriaga & Seljak 1997) arises due to local quadrupole anisotropies at each point on the surface of last scattering (see Hu & White 1997a for a review). Scalar (density) perturbations generate linear (electric mode) polarization only, but tensor (gravitational wave) perturbations can generate circular (magnetic mode) polarization. Hence the polarization of the CMB is a potentially useful probe of the level of gravitational waves in the early universe (Seljak & Zaldarriaga 1997; Kamionkowski & Kosowsky 1998), especially since current indications are that the large-scale primary anisotropies seen by COBE do not contain a measureable fraction of tensor contributions (see Chapter 4).

1.4.4 Gaussianity of the CMB anisotropies

The processes turning density inhomogeneities into CMB anisotropies are linear, so cosmological models that predict gaussian primordial density inhomogeneities also predict a gaussian distribution of CMB temperature fluctuations. Several techniques have been developed to test COBE and future datasets for deviations from gaussianity (e.g. Kogut et al. 1996a; Ferreira & Magueijo 1997; Ferreira et al. 1997). Most tests have proven negative, but a few claims of non-gaussianity have been made. Gaztañaga et al. (1998) found a very marginal indication of non-gaussianity in the spread of results for degree-scale CMB anisotropy observations being greater than the expected sample variances. Ferreira et al.

(1998) have claimed a detection of non-gaussianity at multipole $\ell = 16$ using a bispectrum statistic, and Pando et al. (1998) find a non-gaussian wavelet coefficient correlation on roughly 15° scales in the North Galactic hemisphere. Both of these methods produce results consistent with gaussianity, however, if a particular beam-size area of several pixels is eliminated from the dataset (Bromley & Tegmark 1999). A different area appears to cause each detection, giving evidence that the COBE dataset had non-gaussian instrument noise in at least two areas of the sky (a true sky signal should be larger than several pixels so instrument noise is the most likely source of the non-gaussianity).

1.4.5 Foreground contamination

Of particular concern in measuring CMB anisotropies is the issue of foreground contamination (see Part II for a full discussion). Foregrounds which can affect CMB observations include galactic radio emission (synchrotron and free-free), galactic infrared emission (dust), extragalactic radio sources (primarily elliptical galaxies, active galactic nuclei, and quasars), extragalactic infrared sources (mostly dusty spirals and high-redshift starburst galaxies), and the Sunyaev-Zeldovich (SZ) effect which results from the Compton scattering of CMB photons by hot gas in galaxy clusters. The COBE team has gone to great lengths to analyze their data for possible foreground contamination and routinely eliminates everything within about 30° of the galactic plane.

An instrument with large resolution such as COBE is most sensitive to the large foreground structure of our Galaxy, but small-scale anisotropy experiments need to worry about extragalactic sources as well. Because they are now becoming critical, these extragalactic foregrounds are studied in detail in Part II. Because foreground and CMB anisotropies are assumed to be uncorrelated, they should add in quadrature, leading to an increase in the measurement of CMB anisotropy. Most CMB instruments, however, can identify foregrounds by their spectral signature across multiple frequencies or their display of the beam response characteristic of a point source. This leads to an attempt at foreground subtraction, which can cause an underestimate of CMB anisotropy if some true signal is subtracted along with the foreground.

Chapter 2

Current Status of Observations

2.1 Cosmic Microwave Background Anisotropy Observations

Since the COBE DMR detection of CMB anisotropy (Smoot et al. 1992), there have been over thirty additional measurements of anisotropy on angular scales ranging from 7° to 0.3° , and upper limits have been set on smaller scales. Shown in Figure 2.1 are COBE (Tegmark & Hamilton 1997), FIRS (Ganga et al. 1994), Tenerife (Gutierrez et al. 1997), South Pole (Gundersen et al. 1995), BAM (Tucker et al. 1997), ARGO (Masi et al. 1996), Python (Coble et al. 1999; Platt et al. 1997), MAX (Lim et al. 1996; Tanaka et al. 1996), MSAM (Wilson et al. 1999), SK (Netterfield et al. 1997), CAT (Scott et al. 1996; Baker et al. 1999), OVRO/RING (Leitch et al. 1998), WD (Tucker et al. 1993), OVRO (Readhead et al. 1989), SUZIE (Church et al. 1997), ATCA (Subrahmanyam et al. 1993), and VLA (Partridge et al. 1997)¹. This figure shows our compilation of CMB anisotropy observations without adding any theoretical curves to bias the eye. It is clear that a straight line is a poor but not implausible fit to the data. There is a clear rise around $\ell = 100$ and then a drop by $\ell = 1000$. This is not yet good enough to give a clear determination of the curvature of the universe, let alone fit several cosmological parameters. However, the data are good enough to prefer certain models of structure formation when a quantitative comparison is made, as will be discussed more in the next few chapters.

The COBE DMR observations were pixelized into a skymap, from which it is

¹CMB observations have also been compiled by Smoot & Scott (1998) and at <http://www.sns.ias.edu/~max/cmb/experiments.html> and <http://www.cita.utoronto.ca/~knox/radical.html>.

possible to analyze any particular multipole within the resolution of the DMR. Current small angular scale CMB anisotropy observations are insensitive to both high ℓ and low ℓ multipoles because they cannot measure features smaller than their resolution and are insensitive to features larger than the size of the patch of sky observed or the angle covered as they “chop” from one direction to another on the sky to eliminate instrumental and atmospheric systematics. The next satellite mission, NASA’s Microwave Anisotropy Probe (MAP), is scheduled for launch in fall of 2000 and will map angular scales down to $0^\circ 2'$ with high precision over most of the sky. An even more precise satellite, ESA’s Planck, is scheduled for launch in 2007. Because COBE observed such large angles, the DMR data can only constrain the amplitude A and index n of the primordial power spectrum in wave number k ($P_p(k) = Ak^n$), and these constraints are not tight enough to rule out very many classes of cosmological models. Throughout this thesis, k is given in its observed units of h/Mpc .

Until the next satellite is flown, the promise of microwave background anisotropy measurements to measure important cosmological parameters rests with a series of ground-based and balloon-borne anisotropy instruments which have already published results (shown in Figure 2.1) or will report results in the next few years (MAXIMA, BOOMERANG, TOPHAT, ACE, VIPER, MAT, VSA, CBI, DASI; see Lee et al. 1999 and Halpern & Scott 1999). Because they are not satellites, these instruments face the problems of shorter observing times and less sky coverage, although significant progress has been made in those areas. They fall into three main categories: high-altitude balloons, ground-based instruments, and interferometers. Past, present, and future balloon-based instruments are FIRS, MAX, MSAM, ARGO, BAM, MAXIMA, BOOMERANG, TOPHAT, and ACE. Ground-based interferometers include CAT, VSA, CBI, and DASI, and other ground-based instruments are TENERIFE, SP, PYTHON, SK, OVRO/RING, VIPER, and MAT. Taken as a whole, they have the potential to yield very useful measurements of the radiation power spectrum of the CMB on degree and subdegree scales. Ground-based non-interferometers have to discard a large fraction of data and undergo careful further data reduction to eliminate atmospheric contamination. Balloon-based instruments need to keep a careful record of their pointing to reconstruct it during data analysis. Interferometers may be the most promising technique at present but they are the least developed, and most instruments are at radio frequencies and have very narrow frequency coverage, making foreground contamination a major concern. In order to use small-scale CMB anisotropy measurements to constrain cosmological models

we need to be confident of their validity and to trust the error bars. This will allow us to discard badly contaminated data and to give greater weight to the more precise measurements in fitting models. Correlated noise is a great concern for instruments which lack a rapid chopping because the $1/f$ noise causes correlations on scales larger than the beam in a way that can easily mimic CMB anisotropies if not analyzed carefully. Additional issues are sample variance caused by the combination of cosmic variance and limited sky coverage and foreground contamination.

2.1.1 Window Functions

The sensitivity of these instruments to various multipoles is called their window function. These window functions are important in analyzing anisotropy measurements because the small-scale experiments do not measure enough of the sky to produce skymaps like COBE. Rather they yield a few “band-power” measurements of rms temperature anisotropy which reflect a convolution over the range of multipoles contained in the window function of each band. Some instruments can produce limited skymaps (White & Bunn 1995). The window function W_ℓ shows how the total power observed is sensitive to the anisotropy on the sky as a function of angular scale:

$$Power = \frac{1}{4\pi} \sum_{\ell} (2\ell + 1) C_{\ell} W_{\ell} = \frac{1}{2} (\Delta T / T_{CMB})^2 \sum_{\ell} \frac{2\ell + 1}{\ell(\ell + 1)} W_{\ell} \quad (2.1)$$

where the COBE normalization is $\Delta T = 27.9\mu K$ and $T_{CMB} = 2.73K$ (Bennett et al. 1996). This allows the observations of broad-band power to be reported as observations of ΔT , and knowing the window function of an instrument one can turn the predicted C_{ℓ} spectrum of a model into the corresponding prediction for ΔT . This “band-power” measurement is based on the standard definition that for a “flat” power spectrum, $\Delta T = (\ell(\ell + 1)C_{\ell})^{1/2} T_{CMB} / 2\pi$ (flat actually means that $\ell(\ell + 1)C_{\ell}$ is constant).

The autocorrelation function for measured temperature anisotropies is a convolution of the true expectation values for the anisotropies and the window function. Thus we have (White & Srednicki 1995)

$$\left\langle \frac{\Delta T}{T}(\hat{n}_1) \frac{\Delta T}{T}(\hat{n}_2) \right\rangle = \frac{1}{4\pi} \sum_{\ell=1}^{\infty} (2\ell + 1) C_{\ell} W_{\ell}(\hat{n}_1, \hat{n}_2), \quad (2.2)$$

where the Gaussian forms above give W_{ℓ} as a function of separation angle only. In general, the window function results from a combination of the directional response of the antenna,

the beam position as a function of time, and the weighting of each part of the beam trajectory in producing a temperature measurement (White & Srednicki 1995). Strictly speaking, W_ℓ is the diagonal part of a filter function $W_{\ell\ell'}$ that reflects the coupling of various multipoles due to the non-orthogonality of the spherical harmonics on a cut sky and the observing strategy of the instrument (Knox 1999a). It is standard to assume a Gaussian beam response of width σ , leading to a window function

$$W_\ell = \exp[-\ell(\ell + 1)\sigma^2]. \quad (2.3)$$

The low- ℓ cutoff introduced by a 2-beam differencing setup comes from the window function (White et al. 1994)

$$W_\ell = 2[1 - P_\ell(\cos \theta)] \exp[-\ell(\ell + 1)\sigma^2]. \quad (2.4)$$

2.1.2 Sample and Cosmic Variance

The multipoles C_ℓ can be related to the expected value of multipole moments by

$$\langle \sum_m a_{\ell m}^2 \rangle = (2\ell + 1)C_\ell \quad (2.5)$$

since there are $(2\ell + 1)$ $a_{\ell m}$ for each ℓ and each has an expected autocorrelation of C_ℓ . In a theory such as inflation, the temperature fluctuations follow a Gaussian distribution about these expected ensemble averages. This makes the $a_{\ell m}$ Gaussian random variables, resulting in a $\chi^2_{2\ell+1}$ distribution for $\sum_m a_{\ell m}^2$. The width of this distribution leads to a cosmic variance in the estimated C_ℓ of σ_ℓ^{cv} proportional to $(\ell + \frac{1}{2})^{-\frac{1}{2}}C_\ell$, which is much greater for small ℓ than for large ℓ (unless C_ℓ is rising in a manner highly inconsistent with theoretical expectations). So, although cosmic variance is an unavoidable source of error for small-scale anisotropy measurements, it is much less of a problem for small scales than for COBE.

Despite our conclusion that cosmic variance is a greater concern on large angular scales, Figure 2.1 shows a tremendous variation in the level of anisotropy measured by small-scale experiments. Is this evidence for a non-Gaussian cosmological model such as topological defects? Does it mean we cannot trust the data? Neither conclusion is justified (although either could be correct) because we do in fact expect a wide variation among these measurements due to their coverage of a very small portion of the sky. Just as it is difficult to measure the C_ℓ with only a few $a_{\ell m}$, it is challenging to use a small piece of the sky to measure multipoles whose spherical harmonics cover the sphere. It turns out that

limited sky coverage leads to a sample variance for a particular multipole related to the cosmic variance for any value of ℓ by the simple formula

$$\sigma_{sv}^2 \simeq \left(\frac{4\pi}{\Omega}\right) \sigma_{cv}^2, \quad (2.6)$$

where Ω is the solid angle observed (Scott et al. 1994).

2.2 Observations of Large-Scale Structure

Theories of structure formation predict that the matter power spectrum is given by $P(k) = T^2(k)P_p(k)$ for matter transfer function $T(k)$ and primordial power spectrum $P_p(k)$. The transfer function describes the processing of initial density perturbations from the Big Bang during the era of radiation domination; the earlier a spatial scale came within the horizon, the more its power was dissipated by radiation (and in the CHDM model, by relativistic neutrinos as well). If the baryon fraction is large, the same acoustic oscillations of the photon-baryon fluid that give rise to peaks in the radiation power spectrum are visible in the matter power spectrum, otherwise the baryons fall into the potential wells of the dark matter. Once matter domination and recombination arrive, $P(k)$ maintains its shape and grows as $(1+z)^{-2}$; hence determining its shape today allows us to extract the power spectrum of primordial density fluctuations that existed when the universe was over a thousand times smaller.

Figure 2.2 shows our compilation of observations of fluctuations in the large-scale distribution of galaxies and galaxy clusters. In this figure, none of the galaxy surveys have been corrected for bias, redshift distortions, or nonlinear evolution. This figure demonstrates impressive agreement among the current large-scale structure observations in terms of the shape of the uncorrected matter power spectrum. Clusters are biased compared to galaxies by about a factor of 3 (about a factor of 10 in $P(k)$) and appear to have a slightly steeper fall-off and a small-scale feature in their power spectrum which is possibly an artifact of the survey window function (Tadros 1999). There is no clear evidence, however, for scale-dependence in the bias of the various galaxy surveys on linear scales.

Figure 2.2 includes the determination of σ_8 , the rms density variation in spheres of radius $8h^{-1}$ Mpc, by Viana & Liddle (1996) based on the abundance of rich galaxy clusters with pre-collapse radii $8h^{-1}$ Mpc. The width of the box represents the range of spatial scales to which σ_8 is sensitive (the half-max window for σ_8 is from $k = 0.05$ to $k = 0.3$

but it has been narrowed for clarity) and the height shows the 68% confidence interval. As an observation of $P(k)$, this scales roughly as Ω_m^{-1} due to the relationship between the observed mass and the pre-collapse radius of rich clusters. Another measurement of σ_8 is shown; this analysis by Bahcall et al. (1997, see also Fan et al. 1997) is based upon the evolution of the abundance of rich clusters from redshift 0.3 until now and is essentially independent of Ω_m . Much attention has recently been paid to using the abundance of galaxy clusters at $z = 0.2 - 0.8$ as a probe of Ω_m (e.g. Carlberg et al. 1997). However, some authors (Colafrancesco et al. 1997; Viana & Liddle 1999) argue that the systematic uncertainties are too large at present for a clear determination of Ω_m . We account for this constraint by using both the value of σ_8 derived from the $z = 0$ cluster abundance and that preferred by the evolution of the cluster abundance; models with the preferred value of Ω_m will have these two observations of σ_8 agree. Both observations of σ_8 are bias-independent. However, it is important to remember that, unlike measurements of $P(k)$, this measurement of σ_8 depends on more than the second moment of the distribution of density variations. A non-gaussian model of structure formation will in general predict a different ratio of the rare overdensities which lead to clusters to the root mean square density variation which is described by the power spectrum. Hence the interpretation of this data is highly dependent on the assumption of gaussianity (see Robinson et al. 1998, 1999 for a full discussion).

Our compilation also includes a measurement of the power spectrum based on peculiar velocities (Kolatt & Dekel 1997). We plot only the point at $k = 0.1$ which is confirmed by the likelihood analysis of Zaroubi et al. (1997). A full discussion of peculiar velocity data is given by Gramann (1998). Peculiar velocities arise due to the gravitational potential of the underlying density field, so this observation is bias-independent. It scales as $\Omega_m^{-1.2}$ (the square of the growing mode) for different models.

In addition, Figure 2.2 shows power spectra from four redshift surveys, the Las Campanas Redshift Survey (LCRS, Lin et al. 1996), the real-space analysis of the IRAS PSCZ survey (Tadros et al. 1999), a cluster sample selected from the APM Galaxy Survey (Tadros et al. 1998), and the combined SSRS2+CfA2 survey (Da Costa et al. 1994). We use the $101h^{-1}$ Mpc version of the SSRS2+CfA2 survey to avoid luminosity bias present in the deeper sample noted by Park et al. (1994). We use the APM Clusters $P(k)$ only for $k \leq 0.12$ to avoid possible artifacts of the survey window function at higher k . The APM cluster $P(k)$ has been analyzed for several background cosmologies, and we use the version most appropriate to each model.

We also show the power spectrum resulting from the Lucy inversion of the angular correlation function of the APM catalog (Gaztañaga & Baugh 1998; Baugh & Efstathiou 1993). We drop the first 4 reported APM points because the analysis is biased compared to numerical simulations on such large scales, where plate matching and galactic extinction are also a concern (Gaztañaga & Baugh 1998). The APM power spectrum is measured in real space, as is the version of PSCZ we use, whereas the others are given in redshift space. Each of these power spectra can be scaled by the square of an unknown linear bias parameter, where the bias is the enhancement of galaxy (baryonic) density perturbations over the density variations in the underlying dark matter distribution. It is expected that the bias is near unity for each of the galaxy survey power spectra, with IRAS having the least bias because of the long correlation length of infrared-bright galaxies and with clusters having a large bias because they trace high density peaks of the primordial density distribution and such peaks are themselves highly clustered (see Kaiser 1984). We have purposely rebinned some of the galaxy survey data to make the points independent.

Structure formation observations at high redshift are improving rapidly and may soon be able to add an intermediate probe between low-redshift large-scale structure and the early universe density perturbations imprinted in the CMB. Observations of high-redshift damped Lyman α systems are a concern for models such as Cold+Hot Dark Matter and Tilted CDM, which have little small-scale power (Gardner et al. 1997; Ma et al. 1997). The improved hydrodynamic simulations of Haehnelt et al. (1998) indicate, however, that all typical structure formation models have enough small-scale power to produce the observations of high-redshift damped Lyman α absorption systems. Improved methods and observations of the Lyman α forest (Croft et al. 1998; Croft et al. 1999b; Hui 1998) have made measurements of the linear power spectrum on sub-Mpc scales possible, although there are significant uncertainties at present, particularly in the normalization of the measured power spectrum. The clustering of Lyman break galaxies observed at redshifts above $z = 3$ (Steidel et al. 1998; Giavalisco et al. 1998; Adelberger et al. 1998) indicates that these galaxies are highly biased, perhaps the precursors of present-day giant ellipticals in clusters. A wide range of cosmological models, however, are consistent with these observations, as the first galaxies that form should be highly biased in any hierarchical model of structure formation.

2.3 Direct Observations of Cosmological Parameters

Observations not based on structure formation can probe cosmological parameters without being dependent on the primordial power spectrum. These “direct” observations include classical cosmological tests of the expansion rate of the universe and its acceleration, the luminosity distance-redshift and angular size distance-redshift relations, and geometrical tests sensitive to the volume-redshift relationship. As is the nature of astronomy, almost all of these observations are really indirect, requiring the assumption of some set of objects as standard rods or candles and being dependent on various systematic uncertainties in those assumptions. This is the challenge of being an observational science where performing controlled experiments is far beyond human capabilities!

A Hubble constant of $65 \pm 15 \text{ km/s/Mpc}$ encompasses the range of systematic variations between different observational approaches (Branch 1998). The former age “crisis” has disappeared with recent recalibration of the distance to the oldest Galactic globular clusters leading to a new estimate of their age of $11.5 \pm 1.3 \text{ Gyr}$ (Chaboyer et al. 1998). Recent observations of primordial deuterium abundance place tight constraints on the baryon density from Big Bang nucleosynthesis, $0.012 < \Omega_b h^2 < 0.026$ (Tytler et al. 1996). Bartelmann et al. (1998) use numerical simulations to compare the observed abundance of arcs from strong lensing by galaxy clusters with the predictions of various models and conclude that only Open CDM works, and they find that critical density ($\Omega_m = 1$) models underpredict the number of arcs by orders of magnitude. Further support for low- Ω_m models comes from the cluster baryon fraction found by Evrard (1997), $\Omega_m/\Omega_b \leq 23h^{3/2}$ with a best fit value of $11.8h^{4/3}$. This favors the ratio of total matter to baryons in models with low matter density and appears to disallow models with $\Omega_m = 1$ and $\Omega_b \leq 0.05$ such as Standard CDM. Models with a high Hubble constant and high baryon fraction are also in trouble.

Observations of Type Ia supernovae at high redshift are progressing rapidly, and results argue in favor of a positive cosmological constant and appear to rule out $\Omega_m = 1$ (Garnavich et al. 1998; Perlmutter et al. 1998; Riess et al. 1998). The amount of cosmological constant, however, is constrained to be $\Omega_\Lambda \leq 0.7$ by QSO lensing surveys (Kochanek 1996), although other analyses of QSO lensing (e.g. Chiba & Yoshii 1997, 1999) support the supernova results. There are also a host of unresolved systematic concerns with the Type Ia supernova analysis, including possible evidence for evolution of the supernovae, the

presence of gray dust (Aguirre 1999a,b), and the need to account for mass inhomogeneities in using the magnitude-redshift relation (Kantowski 1998; Moffat & Tatarski 1995). While further consideration of systematic issues is needed, there is not yet any evidence that the results are biased, and the Type Ia supernovae observations are the strongest direct probe of cosmology available at present.

2.4 Sample Variance of Cosmological Surveys

Beyond the expected variations in Hubble's constant that have been calculated in the literature using analytic approximations and numerical simulations (Turner et al. 1992; Shi et al. 1996; Wu et al. 1996; Shi & Turner 1998; Wang et al. 1998), there are significant effects caused by both sample variance and cosmic variance on a number of measured cosmological parameters. Zehavi et al. (1998) find evidence from the velocity flow of local Type Ia supernovae that there is a large-scale void, a 20% underdensity, surrounding us. This underdensity causes the local value of H_0 to be higher than the global value by $\sim 6\%$. Whether this void is real or not, inhomogeneities at this level are expected in our universe, creating sample variance in measurements of the Hubble constant and the magnitude-redshift relation.

Cosmic variance is important when we have only a limited volume of the universe that can possibly be observed at a given epoch (at least without waiting a very long time to see a different region of the universe at that epoch.) For example the abundance of galaxy clusters at a given redshift is only measured for the portion of the universe we currently observe near that redshift. This turns out to be a small effect on the inferred number abundance for moderate to high redshifts, but it adds a few percent cosmic variance error to determination of σ_8 based on the $z = 0.05$ cluster number abundance.

Sample variance is a greater concern. The high redshift cluster abundance is determined from only a small fraction of the available volume at that redshift, although it turns out to be a sufficient volume for sample variance to be much less important than the Poissonian variance which is already taken into account in these analyses. In fact, the biggest uncertainty here is what actual volume has been surveyed, which is under some debate in the literature. None of these effects seems enough to reconcile $\Omega_m = 1$ with the very massive clusters seen at high redshift, as long as gaussianity is assumed (see Robinson et al. 1999 for the additional consideration of non-gaussianity).

Sample variance has been overlooked far too often in analyses of small regions of high-redshift sky, most egregiously the Hubble Deep Fields. Judging the cosmic star formation history from those regions is quite dangerous. The angular size is that of a cluster of galaxies, at basically all redshifts, so we expect significant density fluctuations at any coordinate distance into the field. The effect can be calculated for an assumed model of density inhomogeneities just as we calculate σ_8 but by using the Fourier transform of the survey volume in place of a spherical top-hat. For biased tracers of the dark matter such as galaxies, the expected density variation is just given by the bias times this σ so it is easy to make a prediction to within a factor of two. Such error bars should be added to any cosmological conclusions made using the Hubble Deep Field and similar surveys.

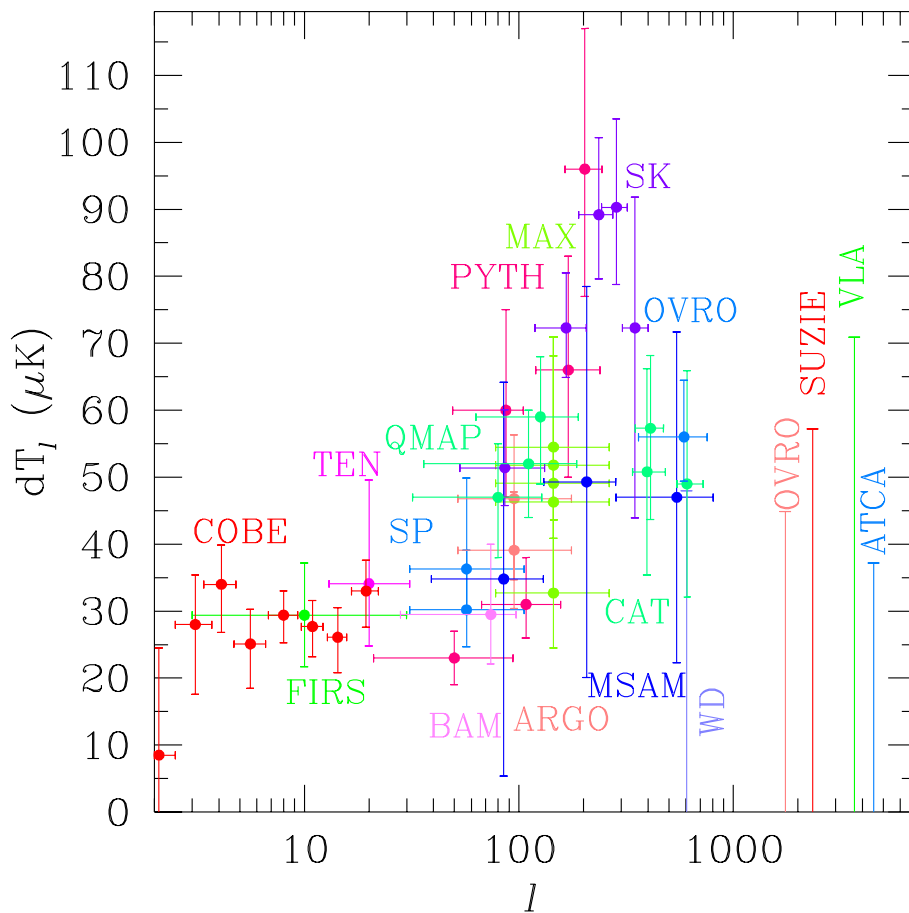


Figure 2.1: Compilation of CMB anisotropy observations.

Vertical error bars represent 1σ uncertainties (2σ for upper limits) and horizontal error bars show the full width at half maximum of each instrument's window function.

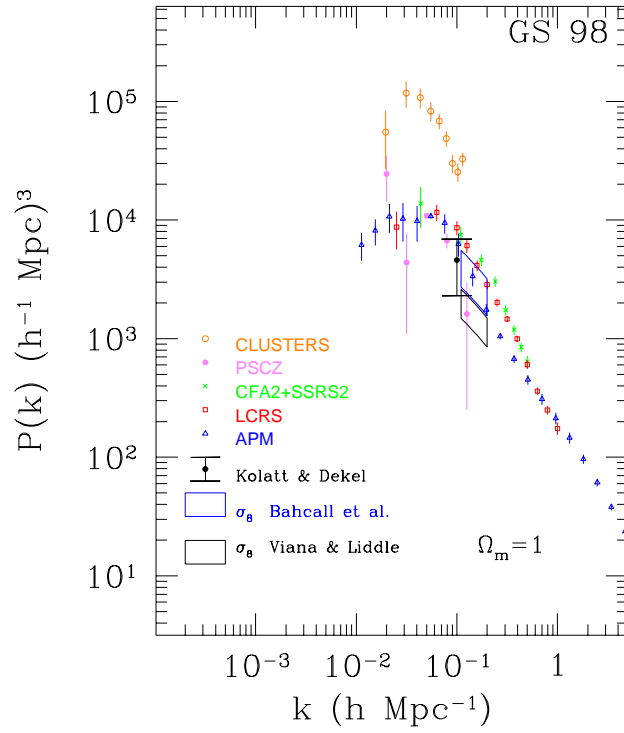


Figure 2.2: Compilation of large-scale structure observations.

No corrections for redshift distortions, non-linear evolution, or bias have been made. k is the wave number in comoving units of h/Mpc . The black and blue boxes are measurements of σ_8 from the present-day number abundance of rich clusters and its evolution (Viana & Liddle 1996; Bahcall et al. 1997, respectively) and the large black datapoint is from peculiar velocities (Kolatt & Dekel 1997). Power spectra shown are: the APM galaxy survey (blue triangles), Las Campanas (red squares), PSCZ (filled pink circles), APM clusters (orange circles), and SSRS2+CfA2 (green crosses).

Chapter 3

Models Tested and Methodology

3.1 Structure Formation Models

We examine ten models of structure formation, which represent the range of cosmological parameters currently considered viable. Due to theorists' productivity, there are an endless number of exotic models we could have used, but we include the most popular variations upon Standard Cold Dark Matter (SCDM) and a sampling of some promising alternatives. Starting from a primordial power spectrum of infinitesimal density perturbations in the early universe, each model predicts how those density perturbations create anisotropies in the Cosmic Microwave Background radiation and inhomogeneities in the distribution of galaxies. By comparing each model with both kinds of data, we investigate whether it provides a consistent picture of structure formation on scales ranging from galaxy clusters to the present horizon size.

Table 3.1 shows the cosmological parameters of our models, where $\Omega = \Omega_m + \Omega_\Lambda$ is the ratio of the energy density of the universe to the critical density necessary to stop its expansion, given by $\rho_c = 3H_0^2/8\pi G$ for a Hubble constant of $H_0 = 100h$ km/s/Mpc. The portion of this critical energy density contained in matter is $\Omega_m = \Omega_{CDM} + \Omega_\nu + \Omega_b$, the sum of the contributions from CDM, Hot Dark Matter (HDM) in the form of massive neutrinos, and baryonic matter. $\Omega_\Lambda = \Lambda/3H_0^2$ is the fraction of the critical energy density contained in a smoothly distributed vacuum energy referred to as a cosmological constant, Λ . The age of the universe in each model is a direct consequence of the values of h , Ω_m , and Ω_Λ ; for a critical matter density universe, it is $2H_0^{-1}/3$ (Weinberg 1972; Carroll et al. 1992). All of our models have an age of at least 13 Gyr except OCDM (12 Gyr).

Table 3.1: Values of cosmological parameters for our models.

τ is optical depth to the last-scattering surface due to reionization, and $x=0.001$ is the residual ionization fraction in the Λ CDM model after recombination. Parameters marked with a * were optimized.

Model	Ω	Ω_Λ	Ω_m	Ω_c	Ω_ν	Ω_b	h	n	Age (Gyr)
SCDM	1.0	0	1.0	0.95	0	0.05	0.5	1.0	13
TCDM	1.0	0	1.0	0.90	0	0.10*	0.5	0.8*	13
CHDM	1.0	0	1.0	0.70	0.2*	0.10*	0.5	1.0*	13
OCDM	0.5	0	0.5*	0.45	0	0.05*	0.6*	1.0*	12
Λ CDM	1.0	0.5	0.5*	0.45	0	0.05*	0.6*	1.0*	14
ϕ CDM	1.0	0	0.92	0.87	0	0.05	0.5	1.0	13
BCDM	1.0	0.88	0.12	0.08	0	0.04	0.8	1.6	15
ICDM	1.0	0.8	0.2	0.17	0	0.03	0.7	2.2	15
PBH BDM	1.0	0.6	0.4	0	0	0.10	0.7	2.0	13
Strings+ Λ	1.0	0.7	0.3	0.25	0	0.05	0.5	~ 1	19

Each model has a primordial power spectrum of density perturbations given by $P_p(k) = Ak^n$ where A is a free normalization parameter and n is the scalar spectral index. The primordial power spectrum does not have to be an exact power law; inflationary models predict slight variation of the power-law index with scale. Allowing this spectral index to vary freely makes it more difficult to constrain cosmological models, as shown by Gawiser (1998b) and discussed in detail in Chapter 6. We normalize to the dataset as a whole, except for the galaxy surveys whose free bias parameter gives them no impact on normalization. Scale-invariance corresponds to $n = 1$. Topological defect models have scaling solutions, so $n = 1$ is approximately correct in an $\Omega_m = 1$ model, but defects will deviate from this scaling in low-matter-density models such as the one considered here.

3.1.1 Standard Cold Dark Matter And Its Variants

The first seven models are based on the Standard Cold Dark Matter (SCDM) model (Davis et al. 1985) and assume that the initial density perturbations in the universe were adiabatic (constant entropy), as is generally predicted by the inflationary universe paradigm. Tilted CDM (TCDM) and Cold + Hot Dark Matter (CHDM) each correspond to changing the shape of the SCDM matter power spectrum to eliminate its well-known problem of excess power on small scales relative to large scales (White et al. 1995; Davis

et al. 1992; Klypin et al. 1993; Pogosyan & Starobinsky 1993; Choi & Ryu 1998). The CHDM model has one family of massive neutrinos which contributes 20% of the critical density. The neutrino mass is given by $m_\nu = 94h^2\Omega_\nu \text{ eV} = 4.7 \text{ eV}$. Strictly speaking, it is possible for particles other than neutrinos to comprise the hot dark matter; Brustein & Hadad (1999) offer a mechanism by which a single species of particles with a bimodal energy distribution can simultaneously comprise cold and hot dark matter. Setting $\Omega_b = 0.1$ helps TCDM and CHDM agree with the high level of CMB anisotropy observed by Saskatoon (SK, Netterfield et al. 1997; we use the recalibration of the SK data from Leitch 1997). The cosmological constant (Λ CDM) and open universe (OCDM) models are similarly motivated; $\Omega_m = 0.5, h = 0.6$ guarantees roughly the right shape of the matter power spectrum (Liddle et al. 1996a,c; Klypin et al. 1996).

We have optimized some parameters of these models: n for TCDM, Ω_ν, n , and the number of massive neutrino families for CHDM, and Ω_m, Ω_b, h and n for OCDM and Λ CDM. Primack et al. (1995) suggest using two equally massive neutrinos to meet the observed cluster abundance, but including the higher value of σ_8 implied by the observed cluster abundance at $z = 0.3$ makes a single massive neutrino slightly favored. For a single massive neutrino, we find $\Omega_\nu = 0.2$ preferable to $\Omega_\nu = 0.3$ by a small margin. The parameters for TCDM and CHDM are within the range found acceptable by Liddle et al. (1996b).

The ϕ CDM model of Ferreira & Joyce (1998) contains a significant energy density contribution from the vacuum energy of a late-time scalar field, $\Omega_\phi = 0.08$. This energy behaves like matter today, but during matter-radiation equality and recombination it alters the shape of the matter and radiation power spectra from the otherwise similar SCDM model. Several other types of scalar fields have been proposed recently (Caldwell et al. 1998; Viana & Liddle 1998; Hu 1998; Turner & White 1997; Coble et al. 1997), and this model is an example that appears to agree well with the observations.

The BCDM model is from Eisenstein et al. (1998a) and contains nearly equal amounts of baryonic and non-baryonic matter. Its parameters have been tuned to produce a peak due to baryonic acoustic oscillations in the matter power spectrum at $k = 0.05h/\text{Mpc}$, where a similar peak is seen in the 3-dimensional power spectrum of rich Abell clusters (Einasto et al. 1997) and the 2-dimensional power spectrum of the Las Campanas Redshift Survey (Landy et al. 1996). BCDM has a scalar spectral index of $n = 1.6$, which is barely consistent with constraints from the COBE FIRAS spectral distortion limits (Hu et al.

1994), although those limits come from small spatial scales so varying n could relax that constraint. To reduce the level of CMB anisotropy that results from this tilt, Λ CDM has reionization with optical depth to the last scattering surface of $\tau = 0.75$. The Tilted CDM model has scalar spectral index $n = 0.8$. The other Λ CDM variants have scale-invariant primordial power spectra with $n = 1$ (Harrison 1970; Zeldovich 1972; Peebles & Yu 1970). For the Open CDM model, we have used the primordial power spectrum from Liddle et al. (1996a), where the scale-invariance of gravitational potential perturbations causes a rise in the matter power spectrum beyond the curvature scale.

3.1.2 Isocurvature Models

The Isocurvature Cold Dark Matter (ICDM) model we consider has been proposed by Peebles (1997, see also Peebles 1999a,b). Its primordial power spectrum is tilted so that $\sigma_8 = 1$ when it is normalized to COBE. Early structure formation, in agreement with observations of galaxies at high redshift and the Lyman α forest, is caused by a non-Gaussian (χ^2) distribution of isocurvature (constant potential) density perturbations of the CDM produced by a massive scalar field frozen during inflation. This model has a residual ionization fraction $x = 0.001$ after decoupling.

The Primordial Black Hole Baryonic Dark Matter (PBH BDM) model of Sugiyama & Silk (1999) has isocurvature perturbations but no Cold Dark Matter. The primordial black holes form from baryons at high density regions in the very early universe during the quark-hadron phase transition and thereafter act like CDM. Only a tenth of the critical energy density remains outside the black holes to participate in nucleosynthesis. These black holes have the appropriate mass ($\sim 1M_\odot$) to be the Massive Compact Halo Objects (MACHOS) which have been detected in our Galaxy (Alcock et al. 1997).

3.1.3 Topological Defect Models

Rough agreement has now been reached on the radiation and matter power spectra predicted for models in which the primordial density perturbations are seeded by topological defects originating in a symmetry-breaking in the early universe. Topological defects are active sources and exist at low redshift, but they play a significant role in structure formation only at relatively early times. Thus their relative predictions for matter and radiation fluctuations are similar to inflationary models, although non-Gaussianity is expected in the

matter distribution. Albrecht et al. (1997) take a range of defect models in critical-density cosmologies and claim that standard topological defect models are ruled out. The Strings + Λ CDM model we use is from Battye et al. (1998, see also Avelino et al. 1997), where the change in cosmology causes a deviation from scaling and makes cosmic strings a viable model.

3.2 Comparison with Observations

In selecting these models, we have not used the current set of direct observations of cosmological parameters to eliminate critical density models, although the Type Ia supernovae results are strong enough to discriminate against even low-density non-cosmological constant models with good statistics. We are more interested at this point in seeing what the structure formation data say directly, and in seeing if there is agreement between the structure formation data and the direct observations of cosmological parameters. Steigman et al. (1999) combined a number of observational constraints and found that the strongest constraint comes from the shape parameter of the matter power spectrum, which we treat in much greater detail here. When they relaxed that constraint, all of our models were allowed at the 2σ level. We find that the current discriminatory power of observations of structure formation outweighs that of direct parameter observations other than the Type Ia supernovae observations and is roughly equal to that of the supernovae results.

Scott et al. (1995) illustrated the comparison between CMB anisotropy and fluctuations in the galaxy distribution. Several similar analyses (Taylor & Rowan-Robinson 1992; White & Scott 1996; Dodelson et al. 1996; Liddle et al. 1996a,c,b; White et al. 1996; Klypin et al. 1996; Hancock et al. 1997; Bond & Jaffe 1997; Lineweaver & Barbosa 1998) have been performed but have used only a portion of the compilation of observations that we present. Webster et al. (1998) includes a more detailed analysis of the galaxy distribution of the IRAS redshift survey than is performed here. When we restrict our analysis to the datasets they consider we find that several models are in good agreement with the data.

We have developed an expanded technique for testing models of structure formation. Our procedure is as follows: we start with a primordial power spectrum of density fluctuations imprinted during the Big Bang. Each cosmological model gives transfer functions that develop this primordial power spectrum into predictions for temperature fluctuations in the microwave background and fluctuations in the distribution of galaxies. We

use the CMBfast code developed by Seljak & Zaldarriaga (1996, see also Zaldarriaga et al. 1998) to calculate the predicted CMB angular power spectrum and matter power spectrum for the SCDM, TCDM, CHDM, OCDM, Λ CDM, and BCDM models and have obtained the power spectra for the other models from their authors. We are able to compare the two types of observations visually by plotting 35 detections of CMB anisotropy, ranging from COBE at 7° to CAT at 0.3° , as model-dependent estimates of the matter fluctuation power spectrum on the same spatial scales. We also derive the variance in density fluctuation amplitudes from the various galaxy redshift surveys. Several complications arise here, which we treat in detail, following the method developed by Peacock & Dodds (1994). The fluctuations are often in redshift space, which must therefore be corrected to physical space. On smaller scales, the effects of non-linearity are important. Finally there is selection bias: IRAS-selected galaxies are more uniformly distributed than galaxies selected optically, and each morphological type is expected to have a scale-independent bias which reflects the enhancement in clustering of density peaks of that mass versus the clustering of the underlying dark matter. Our assumption that bias is constant for a given morphology of galaxies except on non-linear scales is supported by Kauffmann et al. (1997), Mann et al. (1998), and Scherrer & Weinberg (1998). We address these issues by correcting the data for redshift distortions and non-linear clustering and finding the best-fit bias of each type of galaxies. These procedures are now well understood on scales above 10 Mpc ($k = 0.2$), so we retain information only on that scale and larger for our statistical analysis. We obtain information on the amplitude of matter density fluctuations from measurements of peculiar velocities and galaxy cluster abundances, which are expected to reflect the underlying dark matter distribution and are therefore bias-independent. We compare the predictions of each model with the corrected observations and compute the probability of obtaining the data given the model.

3.2.1 Cosmic Microwave Background Anisotropy Detections

In order to compare the predictions and observations for each structure formation model on one plot, we have translated these observations of the angular power spectrum into estimates of the matter power spectrum on the same range of spatial scales. We could instead compare both data sets as reconstructions of the primordial power spectrum which existed in the very early universe, but here we choose to plot the data as measurements

of the matter power spectrum, whose shape has been constant since the era of matter domination began. Due to projection effects, fluctuations at the last-scattering surface on a given angular scale, represented by a spherical harmonic multipole $\ell \simeq 180^\circ/\theta$, are generated by density perturbations from a range of spatial scales centered on a wavenumber k , where $\ell \simeq k\eta_0$ and the distance to the last scattering surface is given by $\eta_0 = 2cH_0^{-1}\Omega_m^{-\alpha}$; $\alpha \simeq 0.4$ in a flat universe and $\alpha = 1$ in an open universe (Vittorio & Silk 1992).

We use this correspondence to plot each CMB anisotropy detection as a box in Figure 3.1 where the width of the box represents the range of k to which that experiment is most sensitive, and the height of the box shows the 68% confidence interval. The boxes follow the local shape of each model's prediction for $P(k)$ to indicate that they are a model-dependent averaging of the power over a range of k . The range of uncertainty includes the statistical uncertainty in the detection, the calibration uncertainty of the instrument, the sample variance from observing only part of the sky, and the cosmic variance from observing at only one location within the universe. The calibration errors, although systematic, have been treated as statistical and added in quadrature. Although calibration errors are correlated for multiple observations by the same instrument, they have been treated as independent, which after the recalibration of SK by Leitch (1997) is a good approximation.

This translation from angular to spatial power spectra is model-dependent in two ways. Each model has a particular value of η_0 which moves the entire set of boxes horizontally. Additionally, each model gives a prediction for the angular power spectrum of CMB anisotropy whose comparison with observations gives the vertical placement of the box, showing the inferred amplitude of matter density fluctuations at that range of spatial scales.

3.2.2 Observations of Large-Scale Structure

We plot our large-scale structure data compilation in Figure 3.2, along with the theoretical matter power spectrum $P(k)$ of the Λ CDM model, with its best-fit normalization. The prediction of σ_8 is an integral over the matter power spectrum using a spherical top-hat window function given by Peacock & Dodds (1994)

$$\sigma_R^2 = \frac{1}{2\pi^2} \int dk k^2 P(k) \frac{9}{(kR)^6} (\sin kR - kR \cos kR)^2. \quad (3.1)$$

The boxes for σ_8 thus follow the local shape of each model's prediction for $P(k)$ to indicate that they are a model-dependent averaging of the power over a range of k . We use the

method proposed by Chiu et al. (1998) and generalized by Robinson et al. (1998) to interpret the observed cluster abundances and their evolution as measurements of σ_8 for the non-Gaussian Strings+ Λ CDM model. For Λ CDM, we use a single determination of $\sigma_8 = 0.9 \pm 0.1$ (Peebles 1999b). The error bars on the measurement of $P(k)$ from peculiar velocities include cosmic variance. To be precise, the cosmic variance should be calculated from the model, but in this case the cosmic variance of a model with the observed level of power has been added in quadrature into the error bars of the observation.

For each galaxy redshift survey, we perform the model-dependent redshift distortion and non-linear evolution corrections for a range of biases and find the best fit bias parameters for each model. The power spectrum observed in redshift space is related to that in real space by

$$\frac{P_z(k)}{P_{real}(k)} = (1 + \beta\mu^2)^2 D(k\mu\sigma_p), \quad (3.2)$$

where the first term gives the Kaiser distortion (Kaiser 1987) from coherent infall of galaxies with bias b as a function of $\beta = \Omega_m^{0.6}/b$ and the second term is the damping of such distortions by the rms pairwise galaxy velocity dispersion σ_p measured in units of H_0 . This velocity dispersion leads to the so-called fingers-of-God effect in redshift surveys. For an exponential velocity distribution,

$$D(k\mu\sigma_p) = (1 + (k\mu\sigma_p)^2/2)^{-1}. \quad (3.3)$$

We couple these terms and average over μ , the cosine of the angle between the line of sight and a given wave vector \mathbf{k} , to produce an estimate of the unbiased real-space spectrum $P_{real}(k) = P_z(k)/f(k, b)$. Defining $K = k\sigma_p/\sqrt{2}$, we have (Ballinger 1997)

$$f(k, b) = \frac{b^2}{K} \left[\tan^{-1}(K) \left(1 - \frac{2\beta}{K^2} + \frac{\beta^2}{K^4} \right) + \frac{2\beta}{K} + \frac{\beta^2}{3K} - \frac{\beta^2}{K^3} \right]. \quad (3.4)$$

For the pairwise velocity dispersion, we use the observation of Landy et al. (1998) of $\sigma_p = 3.63h^{-1}\text{Mpc}$; their determination that the velocity distribution is exponential motivates using that form for the damping term. We have tried this analysis using the higher value of $\sigma_p = 5.70h^{-1}\text{Mpc}$ claimed by Jing et al. (1998) and it makes only a small difference on quasi-linear scales; at $k = 0.2$ the scale-dependence of the redshift distortions is a 15% effect for the Landy et al. value and twice that for the higher one. This systematic uncertainty in the pairwise velocity dispersion makes the corrected real-space power spectrum somewhat unreliable on smaller scales. Smith et al. (1998) give a full discussion of the effects of varying σ_p and propagating this systematic uncertainty through the linearization

procedure; their results confirm that the systematic uncertainty is small up to $k = 0.2$. They also find good agreement between the linearized observations and linear theory under the CHDM model when optically-selected galaxies have bias $b = 1.1$.

After correcting for redshift distortions and bias, we have the unbiased real-space non-linear $P(k)$ represented by a given galaxy survey (shown in Figure 3.3). Next, we correct for non-linear evolution to produce estimates of the linear power spectrum from these galaxy surveys. Because collapsing structure leads to a change of physical scale, observed k_{nl} can be corrected to their linear values, given by

$$k_l = (1 + \Delta_{nl}^2)^{-\frac{1}{3}} k_{nl}, \quad (3.5)$$

using the observed power per logarithmic k -interval, $\Delta^2 = k^3 P(k)/2\pi^2$. The non-linear evolution from k_l to k_{nl} is given by $\Delta_{nl}^2 = f(\Delta_l^2)$. A semi-analytic fit for this function with 10% accuracy compared to numerical simulations is given by Peacock & Dodds (1996). By inverting their formula numerically, we linearize the unbiased real-space non-linear $P(k)$ to extract the primordial density fluctuations. The accuracy of this formula is confirmed by Smith et al. (1998).

This correction for non-linear evolution is model-dependent, as it assumes a local slope for the original linear power spectrum based on the model being tested. On scales $k \leq 0.2$ this linearization preserves the shape of the observed non-linear $P(k)$ while sliding the data points to smaller k values; the main effect of linearization is to shrink the error bars. The APM and PSCZ real-space galaxy power spectra are corrected for bias and then linearized. For the clusters, we use only the scale-independent Kaiser distortion term to correct for redshift distortions as the clusters are engaged in coherent infall onto superclusters. The magnitude of the variation due to systematic uncertainty in the pairwise velocity distribution at $k = 0.2$ is not changed by this linearization procedure, as $k = 0.2$ is roughly the scale where $\Delta^2 = 1$ and non-linear evolution is therefore significant only at smaller scales.

Figure 3.4 shows the reconstructed linear real-space power spectrum data for the SCDM model with CMB anisotropy constraints shown as well. The non-linear evolution causes a kink in the observed APM $P(k)$ at $k = 0.2$. We find that the lack of a kink in the observed LCRS and SSRS2+CfA2 data results from the rough cancellation of non-linear evolution and velocity dispersion damping on scales between $k = 0.2$ and $k = 1$. The high- k

end of the LCRS data shows that the combination of deconvolving the fingers-of-God and linearizing the data has kept the shape relatively the same but moved the points along that curve and reduced the error bars. The linearization of the APM dataset has removed the kink at $k = 0.2$ but gives a slight curve around $k = 1$, an indication of a problem in either the model or the procedure at those scales. The error bars are generally smaller between $k = 0.1$ and $k = 0.2$ than at larger scales, giving this region the most weight in selecting the best-fit biases. The dataset as a whole is rather smooth, showing no strong indications of peaks or troughs; this contradicts the finding of Einasto et al. (1997) based on the power spectrum of rich Abell clusters. As noted by Gaztañaga & Baugh (1998), a clear peak is taking shape in the matter power spectrum around $k = 0.03$, which constrains $\Omega_m h$ by identifying the epoch of matter-radiation equality. The large-scale structure observations contain too much information to be summarized by a single shape parameter; no value of the traditional CDM shape parameter, Γ (Efstathiou et al. 1992), can simultaneously match the location of this peak and its width.

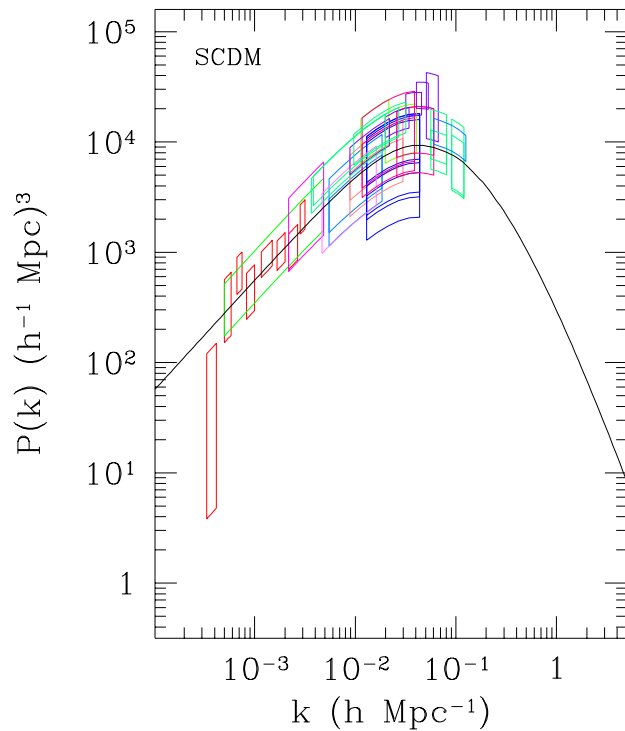


Figure 3.1: CMB anisotropy observations shown with SCDM power spectrum.

Each box has a width indicating the range of k to which the corresponding observation is sensitive and a height indicating the 1σ error bars of the band-power observed. The amount by which the box is above or below the curve indicates how much more or less power that observation prefers versus the normalization of the theory shown here.

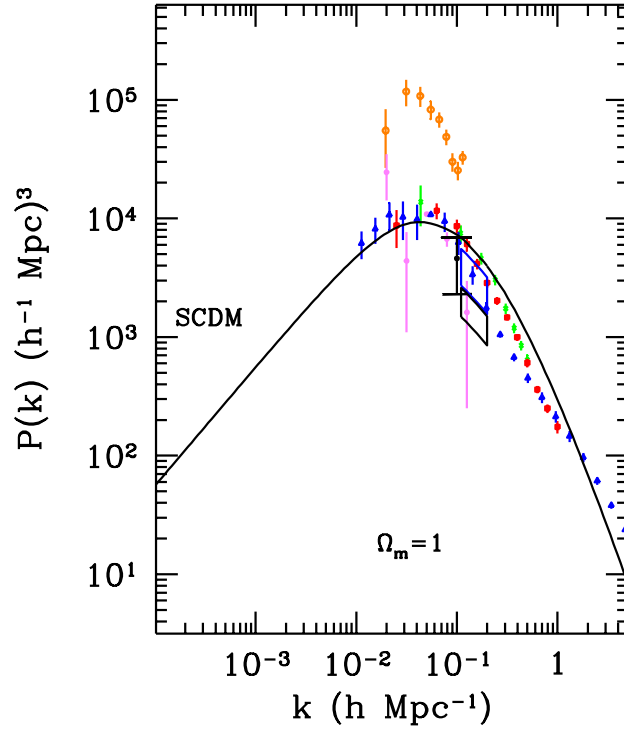


Figure 3.2: Compilation of large-scale structure observations with SCDM $P(k)$.

No corrections for redshift distortions, non-linear evolution, or bias have been made. Black and blue boxes are measurements of σ_8 and the large black point with error bars is from peculiar velocities. Power spectra shown are: the APM galaxy survey (blue triangles), Las Campanas (red squares), IRAS (pink circles), APM clusters (orange circles), and SSRS2+CfA2 (green crosses).

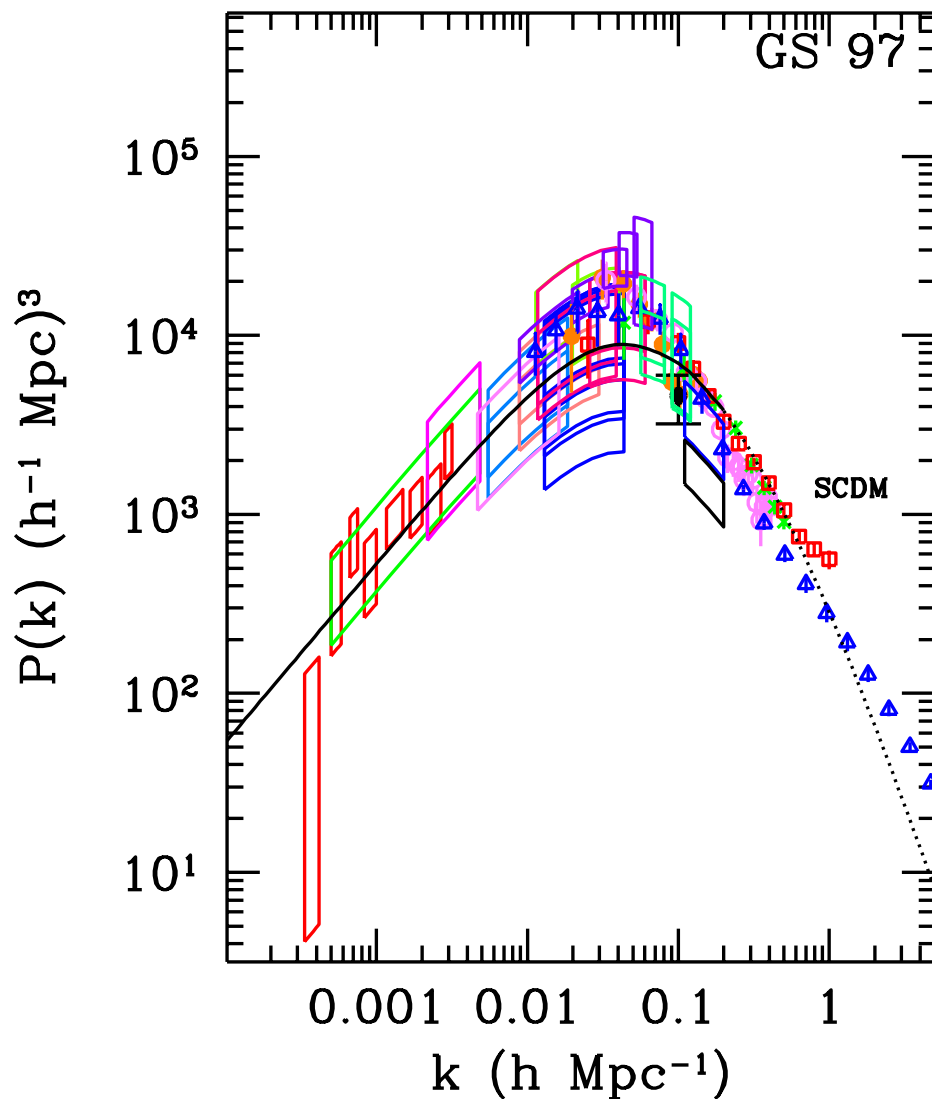


Figure 3.3: SCDM compared to CMB and LSS data, after the LSS data have been corrected for redshift distortions, but not yet for non-linear evolution. This represents our reconstruction of the real-space non-linear power spectra, but it is compared with the linear theory prediction for the SCDM power spectrum.

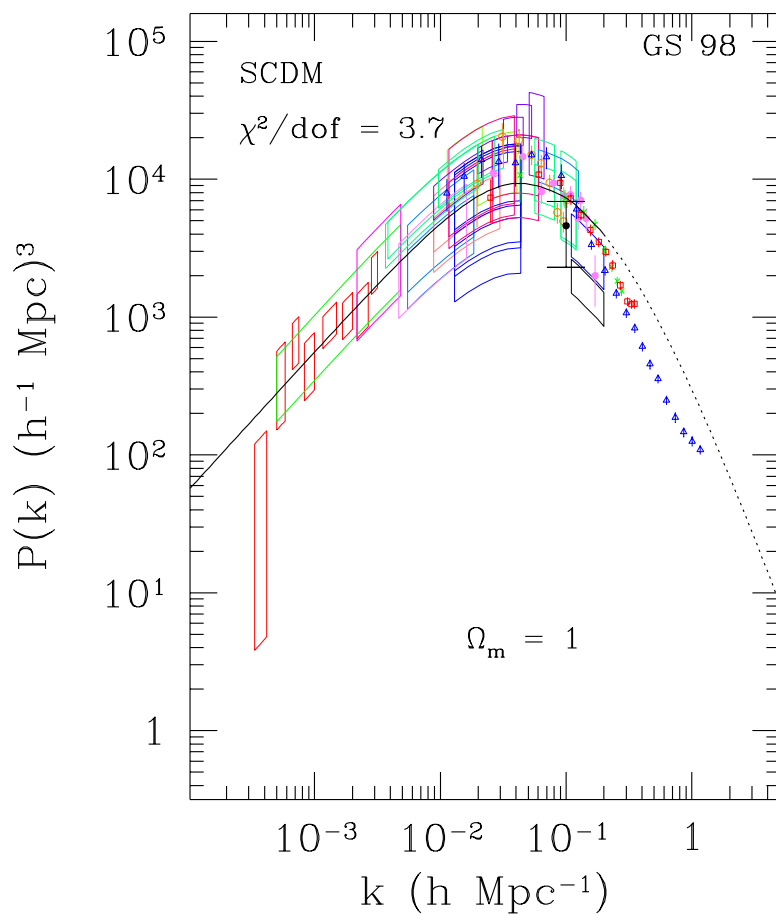


Figure 3.4: The SCDM model compared to the data, which has undergone model-dependent corrections for redshift distortions, bias, and non-linear evolution. Beyond $k = 0.2$, the predicted matter power spectrum curve is dotted to indicate uncertainty in the data corrections.

Chapter 4

Results

4.1 Goodness of Fit

Because we have predictions, observations, and error bars for each data point, it is straightforward to calculate the χ^2 value and the resulting probability of obtaining the data for each model. Only points observed at $k \leq 0.2$ are used in calculating χ^2 ; our conclusions are unaffected by varying this non-linear cutoff between $k = 0.15$ and $k = 0.25$. On smaller scales, the linearization process allows us to gain qualitative information despite the systematic uncertainties on smaller scales, and we show the model power spectrum as a dotted line on these scales to indicate that only qualitative comparison is possible. CMB predictions are calculated and compared to observations in ℓ -space but using the k -space boxes shown would yield an identical value for χ^2 . Instead of normalizing to the COBE result alone (Bunn & White 1997), we give each model a free normalization parameter. Our rationale is that COBE is just one subset of the available data, albeit with small error bars, and is in fact the data most likely to be affected by a possible contribution of gravitational waves to microwave background anisotropies. These gravitational waves from inflation would have a significant impact only on large angular scales and are not traced by the large-scale structure observations. By normalizing to the data set as a whole, we make our results relatively insensitive to the possible contribution of gravitational waves. Because of the range of spatial scales and amplitudes covered, our figures are log-log plots, so the models which seem by eye to be the best fits may not in fact have the best linear chi-squared value. We have tested the effect of asymmetry in the error bars by calculating χ^2 on the log of the data (which greatly overestimates that asymmetry), and we find no

significant change in our conclusions. The precision of the next generation of observations will require full knowledge of the covariance matrices of the observations and the asymmetry of the error bars (see Bond et al. 1998; Bartlett et al. 1999).

Table 4.1: Best-fit normalizations and biases. The normalization of each model is given by σ_8 or the value of dT at $\ell = 10$, which can be compared to the COBE normalization of $dT = 27.9\mu\text{K}$.

Model	dT_{10} (μK)	σ_8	b_{clus}	b_{cfa}	b_{lcrs}	b_{apm}	b_{iras}
SCDM	25.4	1.08	2.12	0.83	0.72	0.89	0.57
TCDM	31.2	0.79	2.73	1.13	1.01	1.18	0.83
CHDM	27.1	0.75	2.52	1.11	1.01	1.13	0.78
OCDM	29.0	0.77	2.67	1.25	1.11	1.10	0.93
Λ CDM	26.8	1.00	2.14	0.91	0.82	0.87	0.68
ϕ CDM	27.6	0.74	3.12	1.35	1.20	1.31	0.98
BCDM	24.8	1.76	1.30	0.48	0.40	0.41	0.37
ICDM	28.2	0.83	2.95	1.25	1.12	1.02	0.97
PBH BDM	29.9	0.78	2.74	1.21	1.09	1.10	0.92
Strings+ Λ	21.2	0.32	6.95	3.10	2.86	2.62	2.48

4.2 Evaluating the Models

Figure 4.1 contains nearly all of these detections and the theoretical curves of our models, with their best-fit normalizations (listed in Table 4.1). All of the theory curves are consistent with the upper limits, which we disregard hereafter. This figure shows that current CMB anisotropy detections by themselves cannot constrain models well, although the shape of the adiabatic radiation power spectra is preferred. Each of our models has a distinct curve; the first three acoustic peaks will be sufficient to distinguish them at the precision of forthcoming satellite observations.

Figures 4.2 through 4.11 show the large-scale structure data after model-dependent corrections compared with the CMB anisotropy observations and the theoretical matter power spectra $P(k)$ of each model.¹ The χ^2 values for each model versus subsets of the data compilation are given in Table 4.2. The present large-scale structure data have more power to discriminate among models of structure formation than do the present CMB anisotropy detections.

¹ Full-size color figures are also available at <http://cfpa.berkeley.edu/cmbserve/fluctuations/figures.html>

Table 4.2: Chi-squared values for our models.

Results are based on data at $k \leq 0.2h\text{Mpc}^{-1}$. The $\chi_{\sigma_8}^2$ category includes the contribution from peculiar velocity measurements. The degree of freedom used by normalizing is counted under χ_{CMB}^2 , and each galaxy survey loses one degree of freedom in choosing a best-fit bias. The Λ CDM model has one less degree of freedom in the $\chi_{\sigma_8}^2$ column and a total of 69. P is the probability of getting χ^2 greater than or equal to the observed value given that a model is correct.

Model d.o.f.	χ_{CMB}^2 34	$\chi_{\sigma_8}^2$ 3	χ_{clus}^2 8	χ_{cfa}^2 2	χ_{icrs}^2 5	χ_{apm}^2 9	χ_{iras}^2 9	χ_{total}^2 70	χ^2 /d.o.f.	P
SCDM	46	36	37	0.2	8	121	18	266	3.8	$< 10^{-7}$
TCDM	51	5	27	0.4	6	49	11	148	2.1	1.8×10^{-7}
CHDM	30	4	20	3	9	10	11	86	1.2	0.09
OCDM	36	2	24	2	11	42	12	128	1.8	2.9×10^{-5}
Λ CDM	30	3	26	2	12	46	13	132	1.9	1.1×10^{-5}
ϕ CDM	32	4	30	0.1	5	71	12	155	2.2	$< 10^{-7}$
BCDM	32	38	33	1	125	225	56	511	7.3	$< 10^{-7}$
ICDM	61	3	17	2	21	50	16	170	2.5	$< 10^{-7}$
PBH BDM	65	4	22	2	9	30	11	142	2.0	8.3×10^{-7}
Strings+ Λ	64	37	20	0.3	8	43	10	182	2.6	$< 10^{-7}$

We find a very poor fit for SCDM (shown in Figure 3.4), which is unsurprising given the difference in shape between the theory curve and the data and the disagreement with the bias-independent measurements at $k = 0.1$. The fit to the CMB is poor, because SK would prefer more power and the best-fit normalization is only 0.82 that of COBE. Figure 4.2 shows the TCDM model. The fit is drastically improved versus SCDM, although the peak of the matter power spectrum is still broader than that found in the data. The fit with the CMB is harmed by the high normalization versus COBE and by the tilt on medium scales, but reaching σ_8 without missing the peak of the matter power spectrum makes this the optimal amount of tilt for an $\Omega_m = 1$ CDM model.

The best-fit model, Cold + Hot Dark Matter, is shown in Figure 4.3 and in expanded detail in Figure 4.4. The agreement with the location and shape of the peak of the matter power spectrum is remarkable, with the exception of the APM cluster power spectrum, which seems to have a narrower peak than the other surveys. The agreement with CMB is excellent as well, although several other models do equally well. As noted

by Peacock (1997) and Smith et al. (1998), the theoretical curve for CHDM matches the APM galaxy power spectrum down to scales well into the non-linear regime, making this model a good explanation of structure formation far beyond the scales used for our statistical analysis. Small variations of the parameters of the model do not improve the fit. Observations of Damped Lyman α absorption systems at high redshift, which probe linear power on presently non-linear scales and are sensitive to the growth function of a particular cosmology, however, are much less favorable for CHDM.

The OCDM model is shown in Figure 4.5. The high value of Ω_m is favored by the location of the peak in the matter power spectrum and the constraints of the SK and CAT CMB anisotropy detections. However, the shape is still not right for the peak. The shape of the APM data is in good agreement with the model on non-linear scales although the data falls consistently below the prediction. $\Omega_m = 0.5$ generates excellent agreement between the two observations of σ_8 . This model is our second best fit, but it is statistically much worse than CHDM.

The Λ CDM model of Figure 4.6 is nearly as successful as OCDM. It is a slightly better fit to the CMB but is worse in comparison to large-scale structure. The observations of σ_8 are again in good agreement, but the location of the peak in the matter power spectrum appears wrong, and the shape does not compare well with that of the APM galaxy survey.

Figure 4.7 shows the ϕ CDM model, which is too broad at the peak and misses a number of APM datapoints. Its agreement with the other datasets is rather good; excluding the APM galaxy survey would make ϕ CDM a much better fit. It remains to be seen whether other variations of scalar field models can match the observations better (see Caldwell et al. 1998; Chiba et al. 1998; Viana & Liddle 1998; Hu et al. 1999).

By far the worst disagreement with the data is seen in Figure 4.8 for BCDM. Choosing parameters to place an acoustic oscillation peak near $k = 0.05$ has clearly generated the wrong shape, even though the APM galaxies and clusters seem to fit the first and second oscillations, respectively. We average the predictions of the matter power spectrum over the rough window function of the observations to take into account the possible smoothing of these oscillations during observation. In order to make the linearization procedure work smoothly, we fixed the local slope of the linear power spectrum; otherwise the oscillating slope produces a mess. It is not clear whether this is a flaw in the procedure, which was only tested on convex power spectra, or whether indeed the non-linear evolution predictions of such a model are in clear disagreement with the data. This issue has been

investigated by Meiksin et al. (1999). The critical problem with the model, however, is that its main peak is in the wrong place; no model with similar oscillations and a baryon content consistent with Big Bang Nucleosynthesis can fix that problem (Eisenstein et al. 1998a). In general, the data are smooth enough to set a limit on the baryon fraction Ω_b/Ω_m ; when that fraction gets higher than about 0.1 the fit worsens. Goldberg & Strauss (1998) discuss the future prospects of this constraint.

In the Isocurvature CDM model of Figure 4.9, the strong rise of the matter power spectrum is caused by the sharp tilt ($n = 2.2$) of the model away from scale-invariance. The fit to the CMB is poor, due to the rise of C_ℓ on COBE scales and too little power compared to Saskatoon. The fit to large-scale structure is mediocre as well, although the narrow peak agrees with the APM Clusters $P(k)$ as well as any model. The linearization procedure seems to work fine; although it was calibrated for Gaussian models, the linearization is expected to be rather similar under the χ^2 distribution (Stirling 1998).

Figure 4.10 shows that the PBH BDM model has similar problems to Λ CDM, although the placement of the peak is a bit improved. The more prominent acoustic oscillation in the matter power spectrum of this model is placed well compared to the data but fails to produce a good fit or break the linearization procedure. With its best-fit normalization, this model seriously underpredicts σ_8 . Overall, this model agrees with the data almost as well as Ω CDM and Λ CDM despite the difficulty of reconciling isocurvature perturbations with current CMB data. This success of isocurvature versus the large-scale structure data, however, implies that it is premature to restrict our consideration to adiabatic models at present.

The Strings + Λ CDM model (4.11) requires a very large bias for all types of galaxies; it is difficult to explain this bias. Correspondingly, the amplitude of bias-independent measurements at $k = 0.1$ is sorely underestimated, and the fit is not very good to the CMB or the APM galaxy survey. However, the model has roughly the right shape for the matter power spectrum. It is possible that the linearization procedure needs to be adjusted to account for the level of non-Gaussianity in the matter distribution, but that only affects the smallest scales considered in our statistical analysis, and the reduced power of this model weakens the effects of non-linear evolution. Overall, this model agrees with the data almost as well as Ω CDM and Λ CDM; if an explanation can be found for the large galaxy bias needed, topological defects may still be a viable paradigm for structure formation.

4.3 Discussion

Perhaps the most impressive result is the rough agreement of the two datasets over a wide range of models, giving strong evidence that the gravitational instability paradigm of cosmological structure formation is alive and well. Models in which the density perturbations arise from inflationary adiabatic, isocurvature, and topological defect initial conditions all succeed in meeting the qualitative standard of rough agreement with the data. The current set of CMB anisotropy detections may be a poor discriminator among adiabatic models, but it prefers them to non-adiabatic models.

Several models (SCDM, TCDM, BCDM, ICDM, PBH BDM, and Strings+ Λ) have a best-fit normalization significantly different from normalizing to COBE and would have been unfairly penalized if forced to that normalization. The Strings model already includes a tensor contribution, but SCDM, BCDM, and PBH would benefit from adding a gravitational wave component that brought them into better agreement with COBE without changing the amplitude of their smaller-scale scalar perturbations. Adding gravity waves is not, however, a panacea for any of those models. In general, the models which are the best fits to the shape of the matter power spectrum have chosen to be close to their COBE normalization, which argues against there being a significant tensor contribution to large-angle CMB anisotropies.

The average ratio of best-fit biases in Table 4.1 is $b_{clus} : b_{cfa} : b_{lcrs} : b_{apm} : b_{iras} = 3.4 : 1.4 : 1.2 : 1.1 : 1$; this is roughly consistent with the bias ratios found by Peacock & Dodds (1994). The CfA galaxies are more strongly clustered than other optically-selected galaxies, which could result from residual luminosity bias in the $101h^{-1}\text{Mpc}$ sample. Most models allow optical galaxies to be almost unbiased tracers of the dark matter distribution.

By restricting our analysis to the linear regime and carefully correcting for the minor effects of scale-dependent redshift distortions and non-linear evolution on those scales, we have made it possible to test models quantitatively. Because of the history of systematic errors in observational cosmology, our conclusions must in the end offer some qualitative interpretation. If all these models are a priori equally likely, the most likely cosmology by a tremendous factor is Cold + Hot Dark Matter, which is the only model consistent with the observations at the 95% confidence level. The disagreement between the data and the other models is sufficient to rule out all of them unless there are severe unanticipated systematic problems in the data. Undoubtedly, there are some small systematic errors; in trusting Gaussian statistics we are essentially relying on a central limit theorem for these

systematics. It is difficult to argue that the error bars have been severely underestimated; expanding them enough to bring Λ CDM into concordance at 5% confidence would make the data a better fit to CHDM than is expected 80% of the time. All models except CHDM are ruled out at above 99% confidence by our comparison, and the agreement of the SCDM variants cannot be improved by simple variations of their parameters.

As it stands, CHDM itself is not statistically very likely, but this is only because of the APM cluster survey, which no model fits much better, and which seems to disagree somewhat with the shape of the galaxy surveys. Dropping the APM cluster $P(k)$ would give CHDM a $\chi^2/\text{d.o.f.}$ of 1.06, which is within the 68% confidence level for the resulting 62 degrees of freedom. We cannot justify doing that, but it is worth investigating whether the APM Cluster survey contains a scale-dependent bias not accounted for by the non-linear evolution formula or if its errors have somehow been underestimated. The two-dimensional APM galaxy survey is by far the strongest discriminator between models; removing it would allow ϕ CDM, Λ CDM, and TCDM to be much better fits, although of those models only ϕ CDM would be allowed at 99% confidence.

Future observations may well show that a variation upon CHDM or a completely different model that imitates its predictions for structure formation is correct, but we find that the amplitude and shape of its spectrum of primordial density fluctuations agree well with the data. This does not provide direct evidence for the existence of hot dark matter, which requires experimental confirmation of neutrino mass (this issue will be discussed in more detail in the next chapter). The CHDM model has other observational hurdles to overcome, including indications of early galaxy formation for which this model has too little power on correspondingly small scales, although it is impressive that CHDM agrees with the linearized APM data so well out to $k = 1$.

If the current results from Type Ia supernovae observations hold up there will be enough statistical power in the direct observations of cosmological parameters to make Λ CDM and ϕ CDM preferred to CHDM, although in that case no model would be a satisfactory fit to both the supernovae and structure formation observations. The next two chapters explore possible resolutions of this conflict.

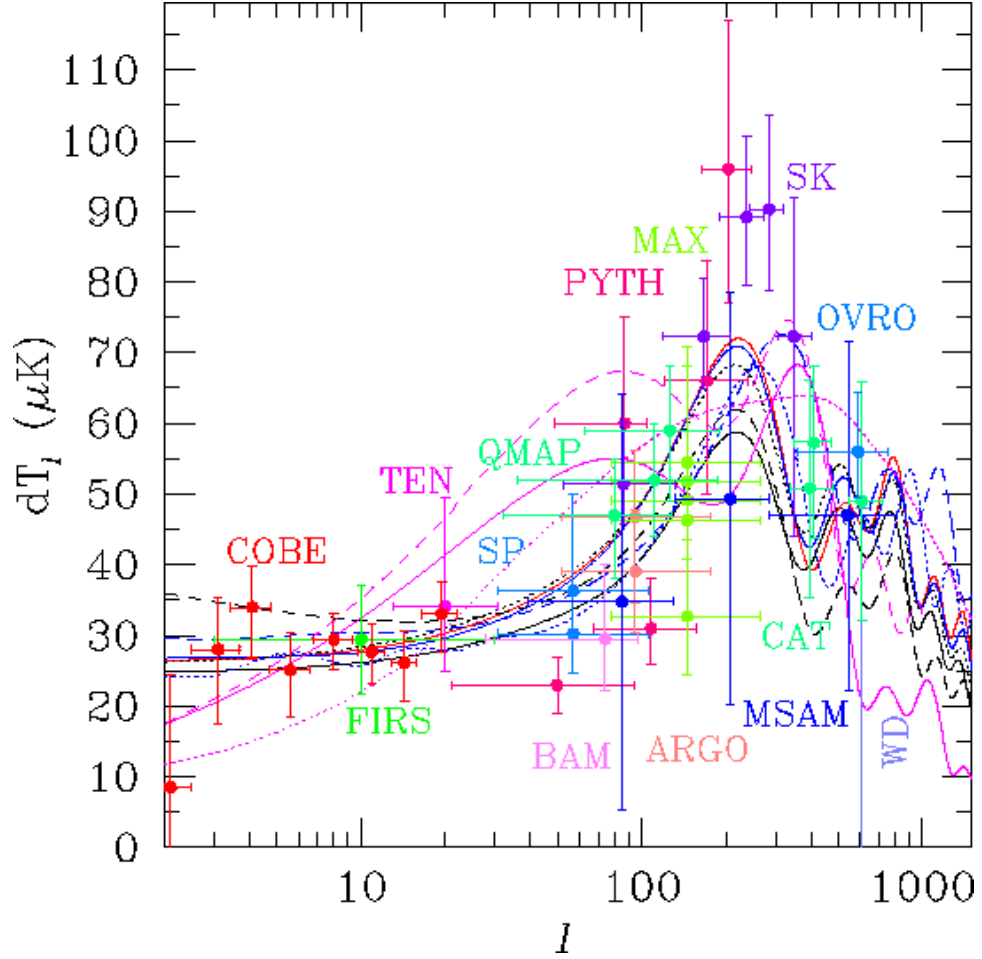


Figure 4.1: Compilation of CMB anisotropy results compared to model C_ℓ .

Vertical error bars represent 1σ uncertainties and horizontal error bars show the width at half maximum of each instrument's window function. Model predictions are plotted as $\Delta T_\ell = (\ell(\ell + 1)C_\ell/2\pi)^{1/2}T_{CMB}$. Models and curves are SCDM (solid black), TCDM (dashed black), CHDM (solid red), OCDM (dashed blue), Λ CDM (solid blue), ϕ CDM (dotted black), BCDM (dotted blue), ICDM (dashed magenta), PBH BDM (solid magenta), and Strings + Λ (dotted magenta).

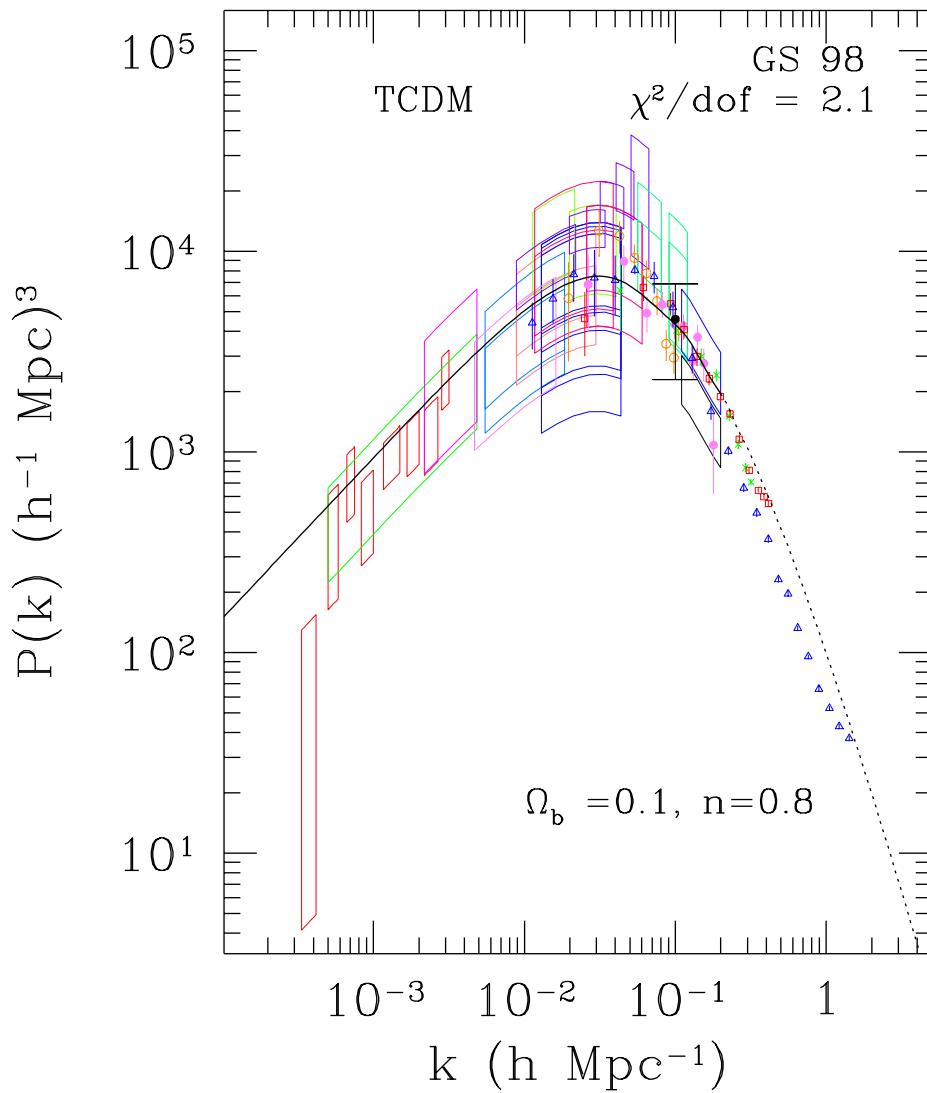


Figure 4.2: The Tilted CDM model compared with CMB and LSS data.

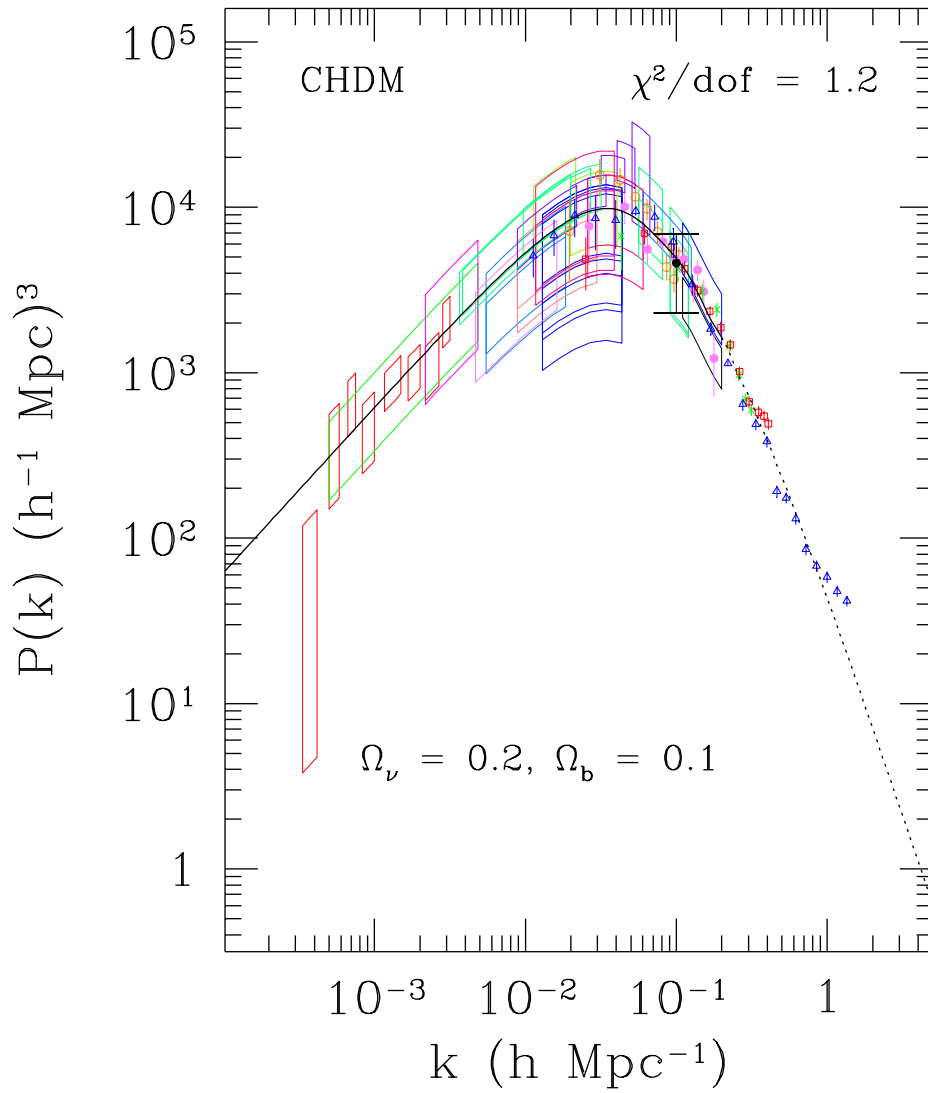


Figure 4.3: CHDM, our best-fit model. Note agreement even on non-linear scales.

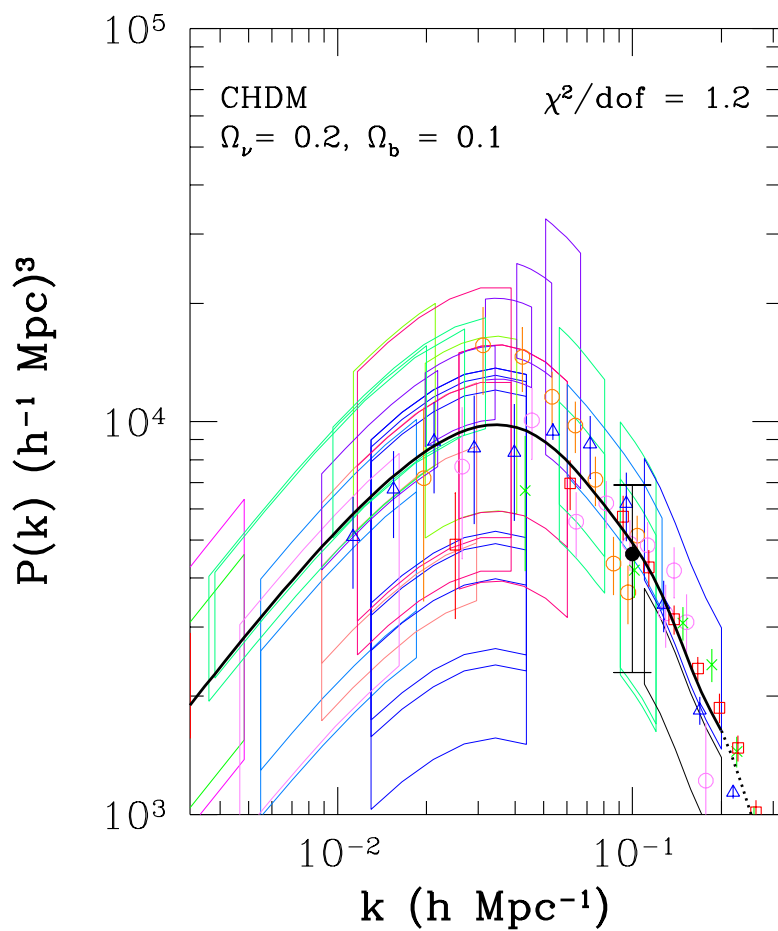


Figure 4.4: Constraints from LSS and CMB on CHDM model expanded in region of highest precision LSS data near $k = 0.1$. The location and shape of the peak in the matter power spectrum and the steepness of its falloff towards higher k are the features that make this model by far the best fit to the data of those we have tested.

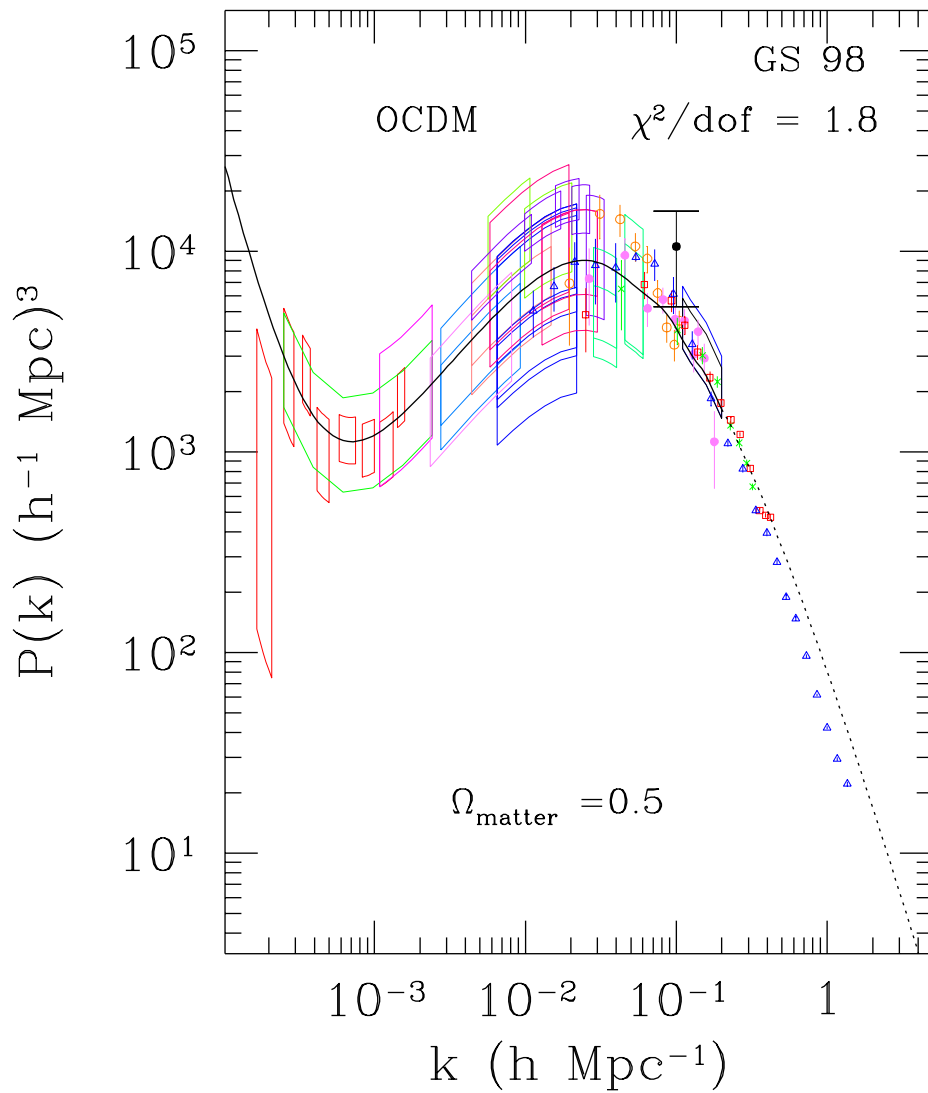


Figure 4.5: Constraints from LSS and CMB on the Open CDM model, with scale-invariance of potential perturbations causing an increase in the matter power spectrum beyond the curvature scale.

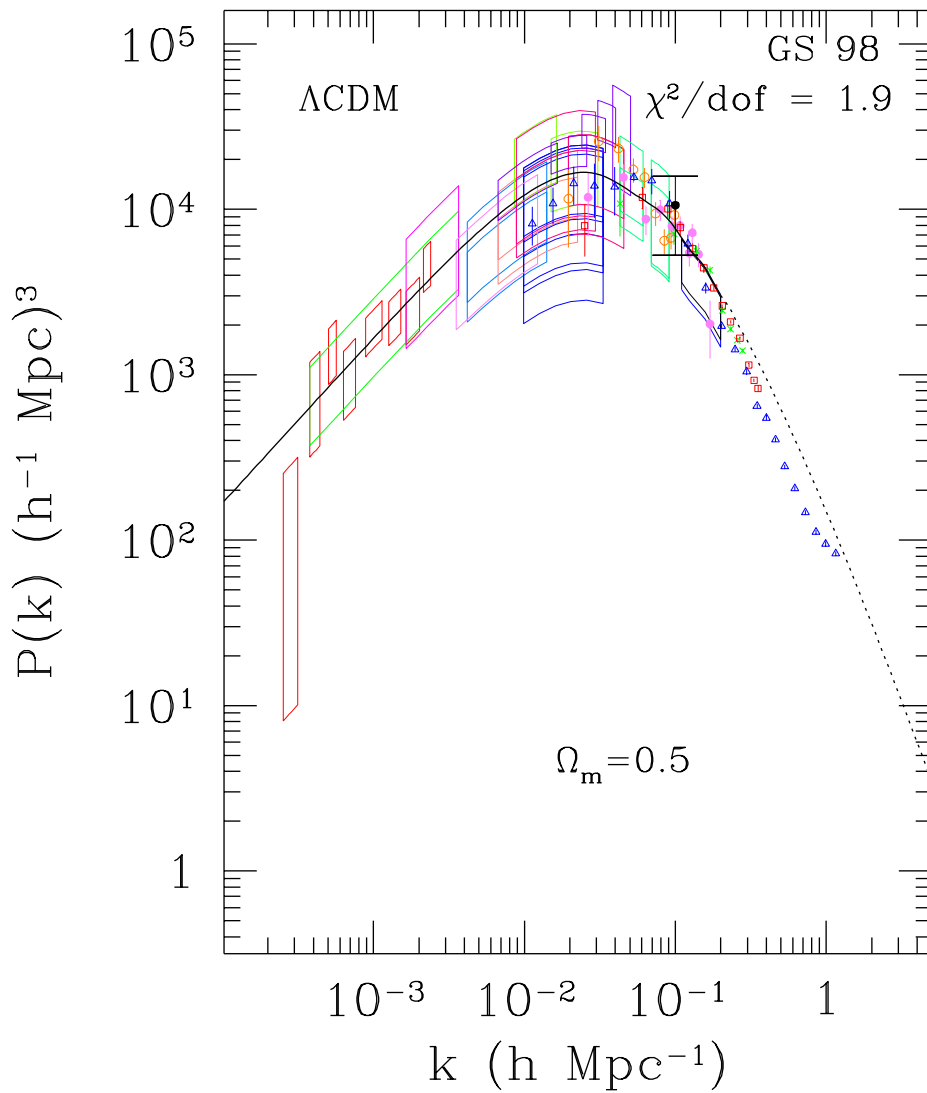


Figure 4.6: Constraints from LSS and CMB on Λ CDM model.

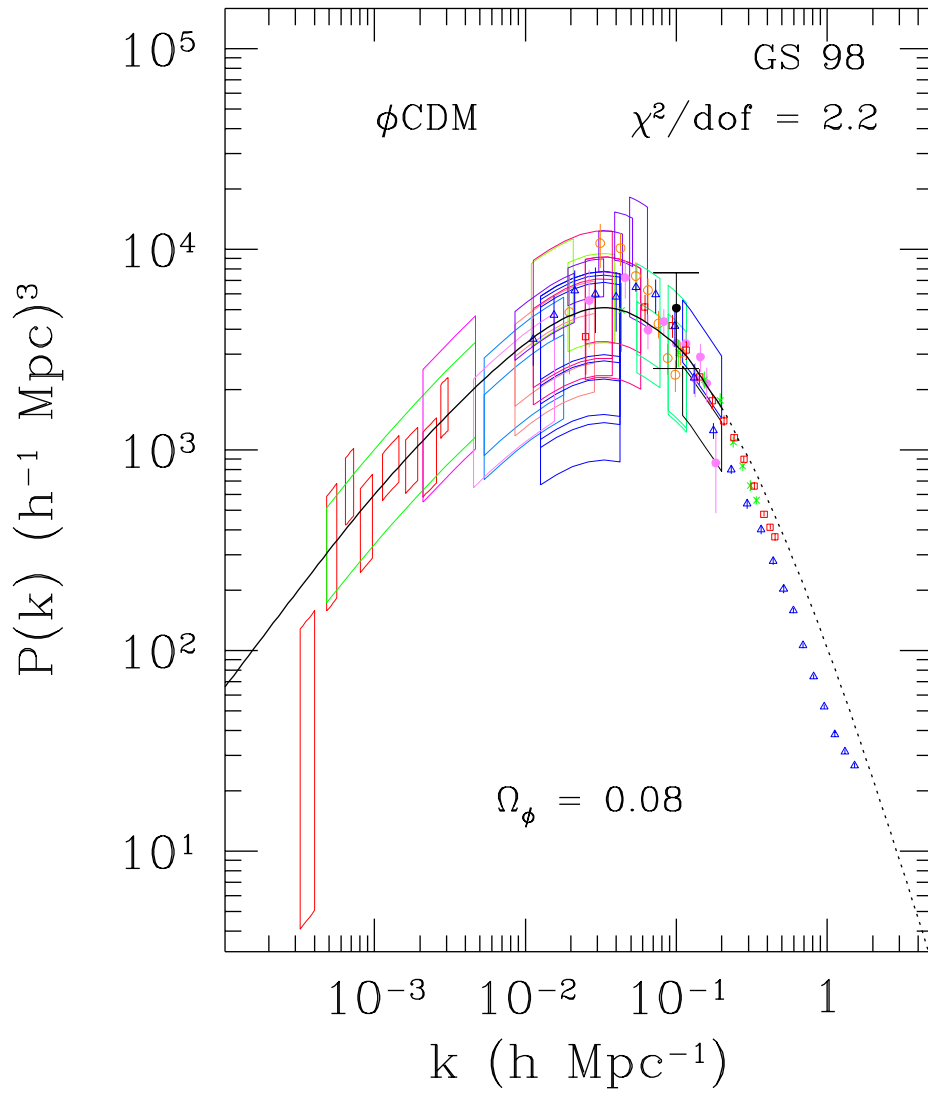


Figure 4.7: Constraints from LSS and CMB on ϕ CDM model.

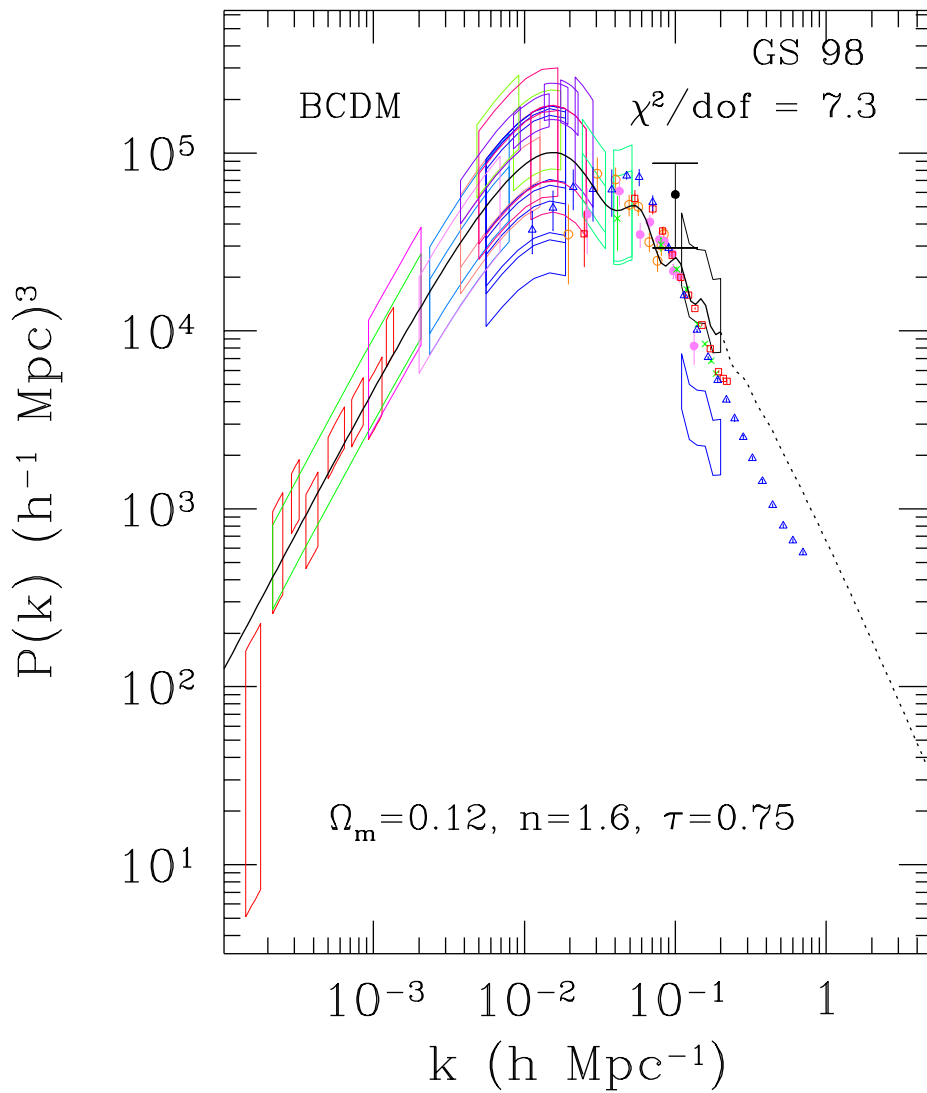


Figure 4.8: The BCDM model. Note the poor agreement at the main peak of the power spectrum.

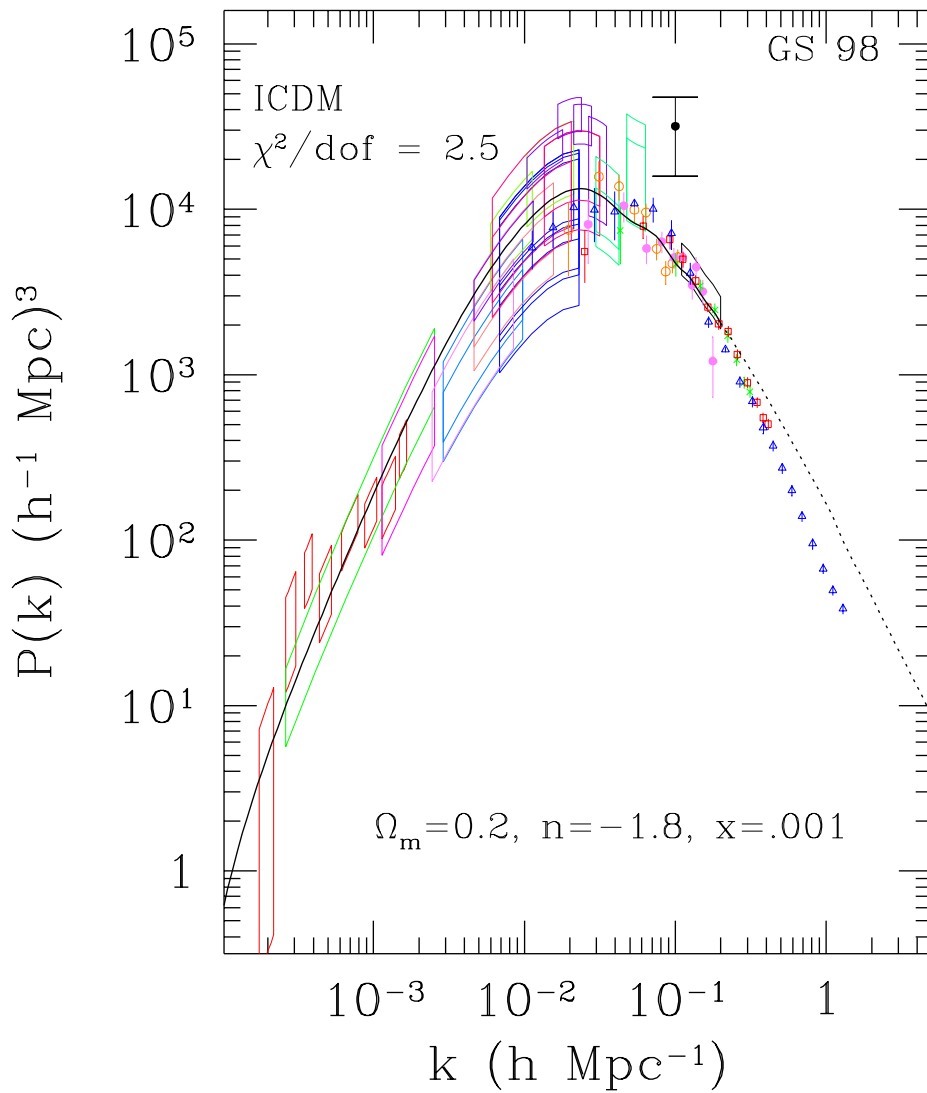


Figure 4.9: Constraints from LSS and CMB on Isocurvature CDM model.

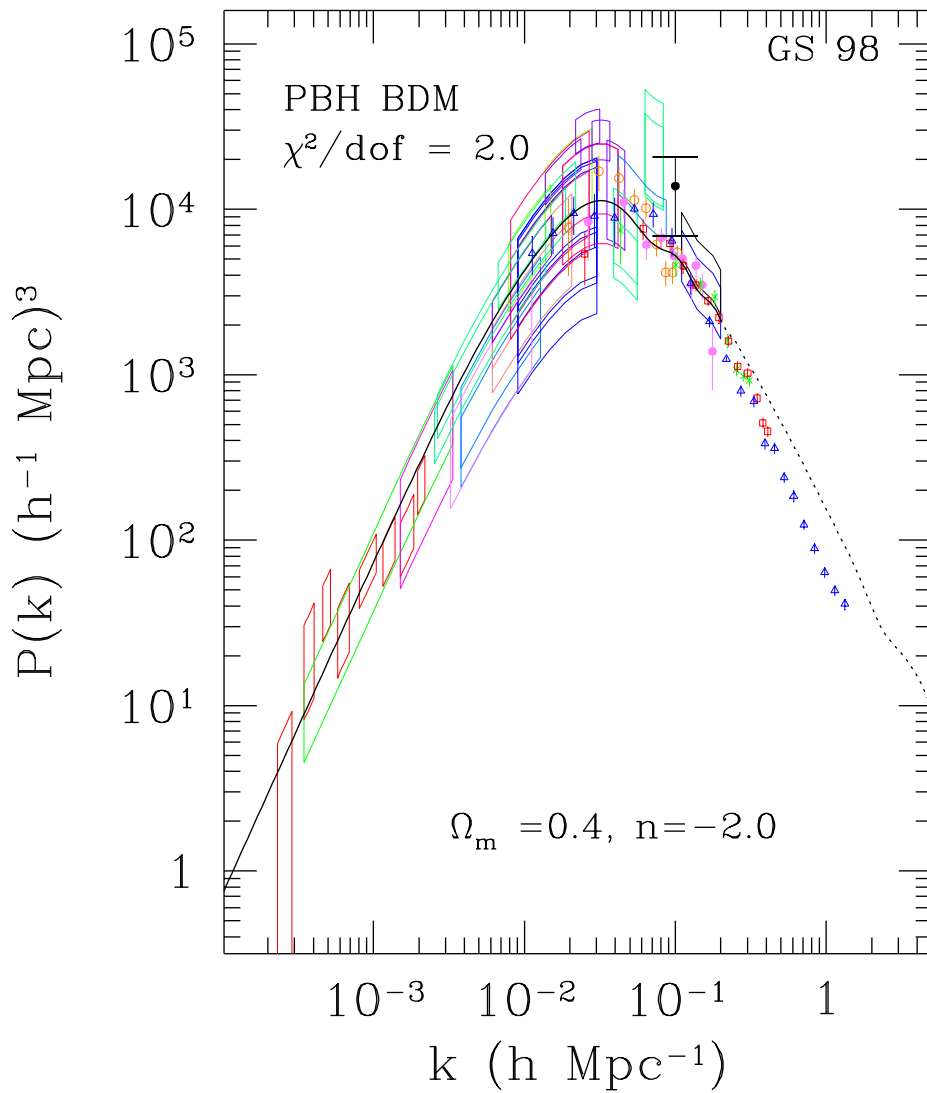


Figure 4.10: Constraints from LSS and CMB on PBH BDM model.

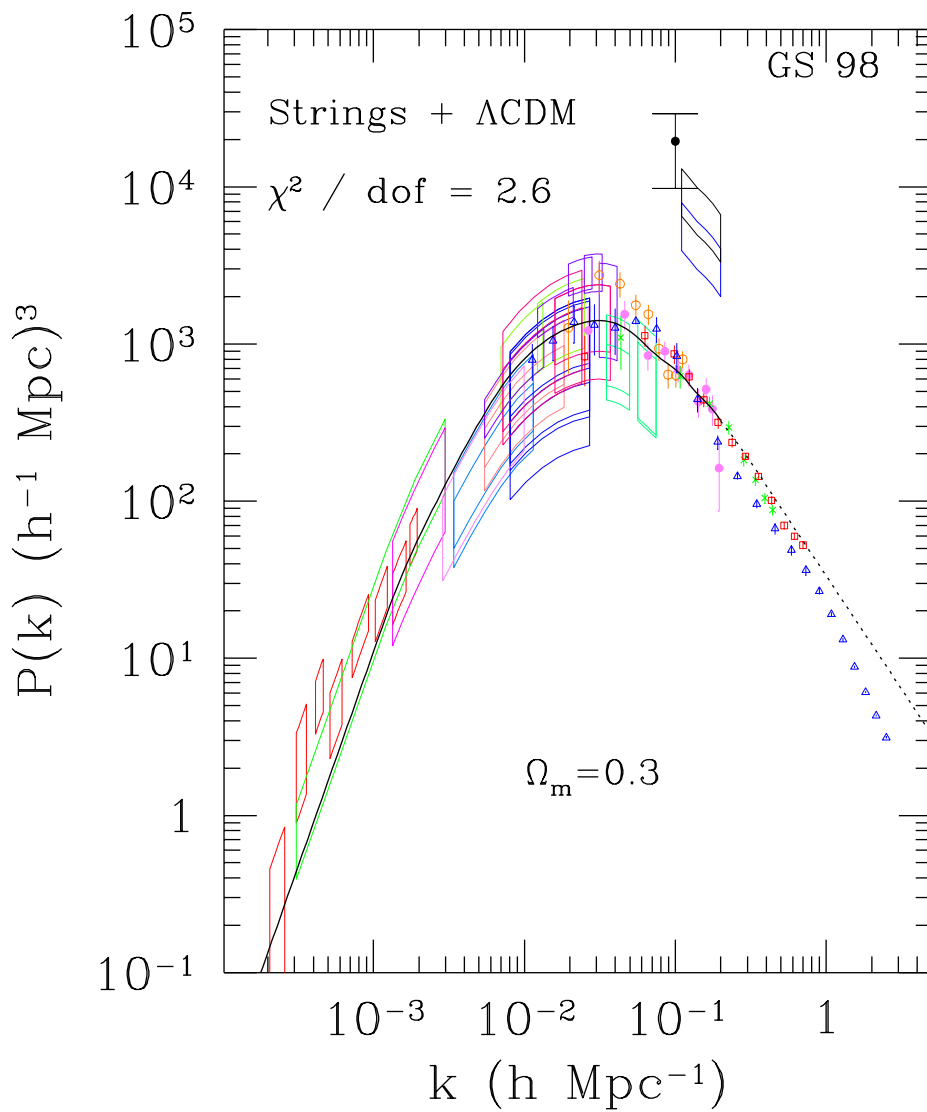


Figure 4.11: Strings + Λ CDM. Notice the deficit of power versus the bias-independent observations at $k = 0.1$.

Chapter 5

Cosmological Limits on the Neutrino Mass

5.1 Is Cold+Hot Dark Matter Compatible with a Cosmological Constant?

The conflict between the Λ CDM model favored by direct observations of cosmological parameters (especially the recent Type Ia supernovae results) and the current set of structure formation observations that we have found motivates us to explore whether there is a simple way to reconcile Λ CDM with those observations. We start with a version of Λ CDM which is in good agreement with all direct parameter observations, with $\Omega_m = 0.4$, $\Omega_b = 0.04$, and $h = 0.7$. Figure 5.1 shows the Λ CDM power spectrum compared with observations of Large-Scale Structure and CMB anisotropy. The problem of the peak location and shape of the matter power spectrum versus the data is the same as that identified in the preceding chapter; the era of matter-radiation equality occurs later in this Λ CDM model than the data appears to prefer, and improving this requires increasing Ω_m which is the opposite of what direct parameter observations recommend.

One can pose the following question: does adding a hot component improve the marginally acceptable LSS fit? We find that as HDM is added, the combined fit to CMB and LSS deteriorates (see Figures 5.2 and 5.3). This occurs because adding HDM reduces the power on physical scales shorter than the neutrino free-streaming length, which exacerbates the mismatch in peak locations that occurs for pure CDM low-density models. A blue tilt of

the primordial power spectrum ($n = 1.3$) is necessary to counteract the damping of small-scale perturbations by free-streaming of the massive neutrinos, which makes the peak of the model fall even farther below that of the data unless $n > 1$. Even with this best-fit value of n , the fit to the data is worse than with no HDM, because CMB observations disfavor such a high value of n . For a higher HDM fraction, an even higher value of n is required ($n = 1.5$ for the $\Omega_\nu = 0.10$ model of Figure 5.3), leading to an even worse fit to the data. Λ CHDM has also been explored by Valdarnini et al. (1998) and Primack & Gross (1998) with different analysis methods and significantly smaller data compilations.

5.2 Limits on the Neutrino Mass

Neutrino masses imprint a distinct signature on $P(k)$, the reduction in power on scales larger than the free-streaming length of 41 Mpc $(m_\nu/30\text{eV})^{-1}$ (Bond et al. 1980). Present cosmological bounds on the mass of a light neutrino are stricter than those from laboratory experiments; a 30eV neutrino would lead to $\Omega_\nu = 1$, so for a universe at less than critical density the neutrinos must all be lighter than this. The exception to this is if the neutrino is so massive that it was non-relativistic during matter-radiation equality, i.e. Cold Dark Matter. For massive CDM neutrinos, the abundance drops enough to no longer overclose the universe; however, laboratory limits rule out the possibility of an electron neutrino more massive than 15eV (Primack & Gross 1998). The shape of the radiation power spectrum of CMB anisotropies (Dodelson et al. 1996) and of the matter power spectrum from large-scale structure are both sensitive to the mass of neutrinos, and the LSS probe may potentially be more powerful (Hu et al. 1998). There is more dynamical range available in probing $P(k)$ with LSS on the neutrino free streaming scale, where the primary signature should be present. Even current data is sensitive to a neutrino mass of around an eV; we find that the fit changes significantly between 0.1 and 1 eV. While there are considerable systematic uncertainties in this approach, it is promising as a complement to the direct evidence for mass difference between neutrino species from SuperKamiokande (Fukuda et al. 1998) and the solar neutrino problem (Bahcall et al. 1998), and is already beginning to conflict with results from LSND (Athanasopoulos et al. 1996) that require a large mass difference.

We have assumed here that Λ CDM is the correct model of structure formation and that the primordial power spectrum is well-described by a power-law. Our limits on the

neutrino mass are based upon an attempt to search the reasonable parameter space around this fiducial model to produce the best fit possible to the data for a given neutrino mass. Since disagreement with CMB data is the main problem once a blue tilt is considered, we have tried to alleviate this by adding a significant tensor component or early reionization. Each of these effects reduces the small-scale CMB power relative to COBE scales, which helps to reconcile $n > 1$ with the CMB data. However, no parameter combination helps enough to make Λ CHDM a better fit than the fiducial Λ CDM model, and this allows us to set upper limits on the neutrino mass. For $n = 1$ we find that $\Omega_\nu < 0.05$ i.e. the mass of the most massive neutrino must be 2 eV or less (the limit is tighter, of course, if there are at least 2 massive neutrinos with nearly equal masses). For a scale-free primordial power spectrum, there is more freedom to increase n to counteract the effect of HDM but this leads to conflict with CMB anisotropy observations, limiting $\Omega_\nu < 0.1$ i.e. the mass of the most massive neutrino must be 4 eV or less. This is compatible with the recent claim by Croft et al. (1999a) that the Lyman α forest power spectrum limits the neutrino mass to 3 eV or less, but our method appears more robust as the normalization of the Lyman α forest power spectrum is quite uncertain and it covers a more narrow range of scales than our large-scale structure compilation. Future constraints from combining CMB and large-scale structure are discussed by Hu et al. (1998) and a more speculative method using weak gravitational lensing surveys is presented by Cooray (1999) .

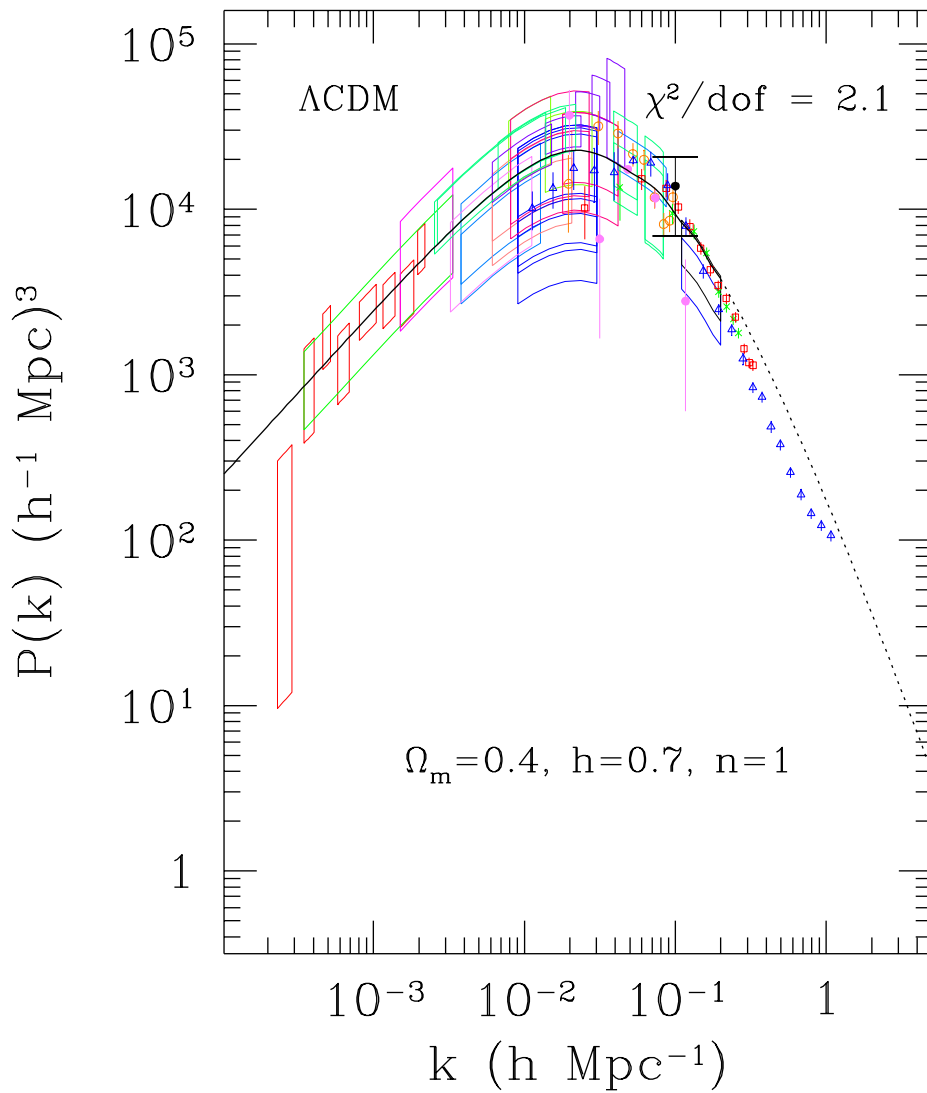


Figure 5.1: Constraints from LSS and CMB on Λ CDM model.

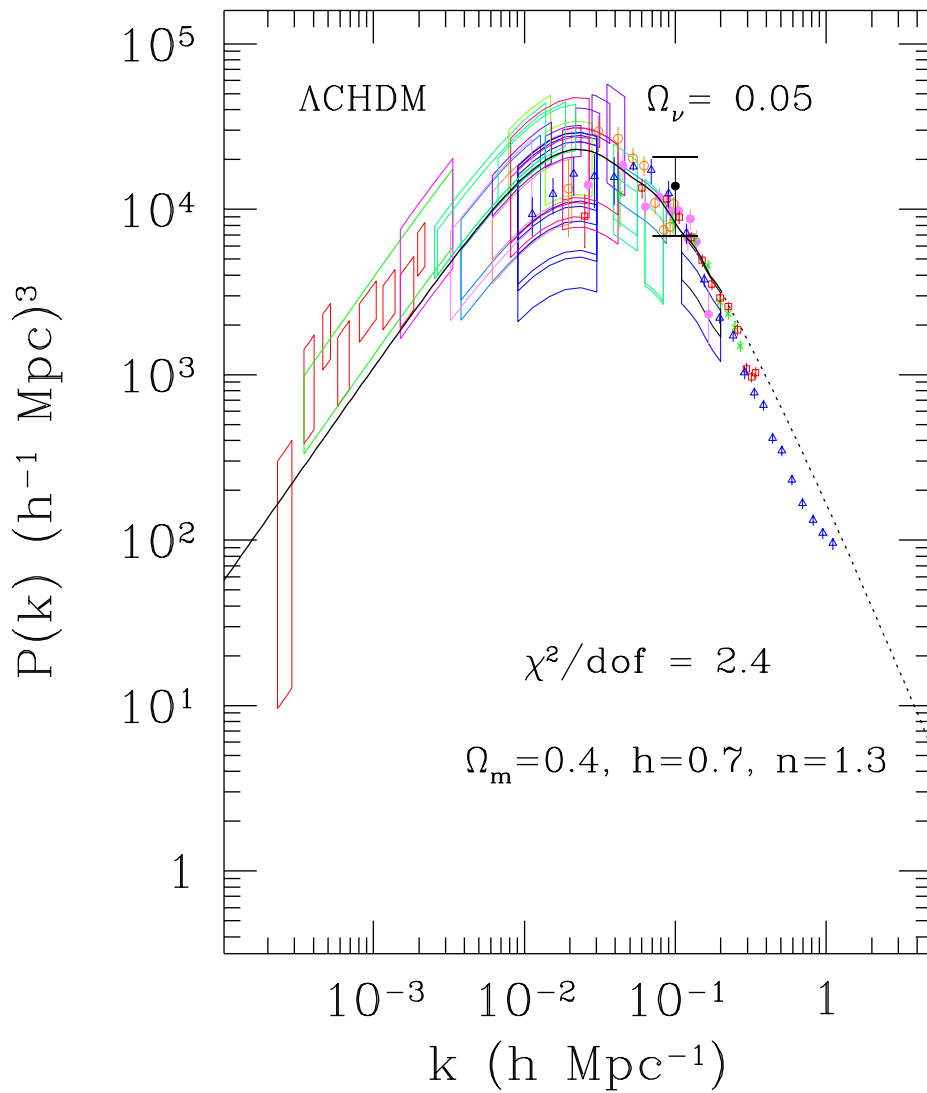


Figure 5.2: Λ CDM model with $\Omega_\nu = 0.05$.

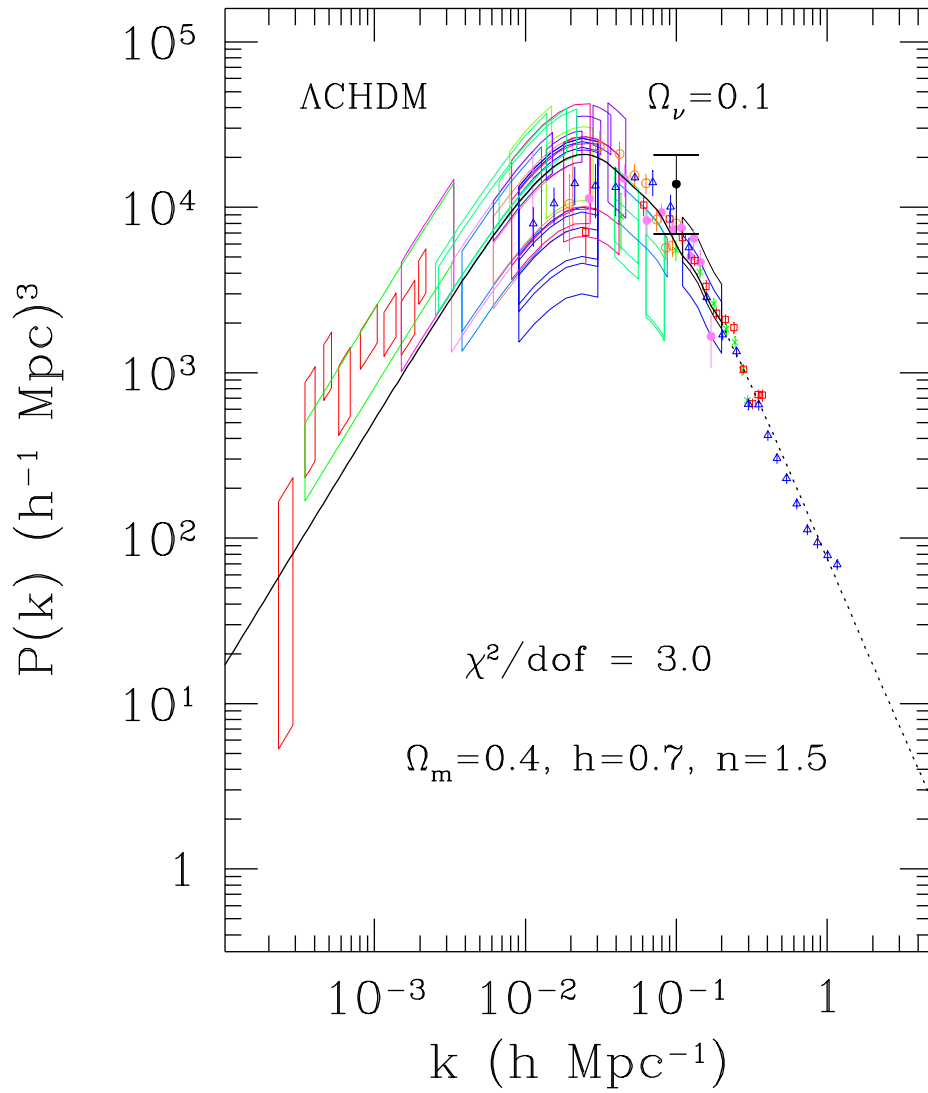


Figure 5.3: Λ CDM model with $\Omega_\nu = 0.10$ and $n = 1.5$.

Chapter 6

Reconstructing the Primordial Power Spectrum

6.1 Motivation

The initial density perturbations in the universe are believed to have originated from quantum fluctuations during inflation or from active sources such as topological defects. Inflationary models predict rough scale-invariance; the shape of the inflaton potential leads to tilting as well as variation of the degree of tilt with spatial scale. The assumption of scale-invariance (Harrison 1970; Zeldovich 1972; Peebles & Yu 1970) is no longer acceptable because the data are now accurate enough to reveal the predicted deviations from $n = 1$.

The combination of Cosmic Microwave Background (CMB) anisotropy measurements and Large-Scale Structure observations has for several years caused dissatisfaction with the standard Cold Dark Matter (sCDM) cosmogony, leading some to advocate a “tilt” of the primordial power spectrum away from scale-invariant ($n = 1$) to $n = 0.8 - 0.9$ (White et al. 1995). Other CDM cosmogonies have not commonly been tilted but their agreement with the data might also improve. Because the primordial power spectrum is an inherent set of degrees of freedom in all CDM cosmogonies, we can find the best-fit primordial power spectrum for any cosmological model. We have seen that adding Hot Dark Matter does not resolve the disagreement of Λ CDM with observations of structure formation, but utilizing a non-scale-free primordial power spectrum may be a solution.

6.2 Methodology

We can adopt a parameterization of the primordial power spectrum as a polynomial in log-log space versus wave number k (Kosowsky & Turner 1995; Gawiser 1998b; Copeland et al. 1998):

$$\log P_p(k) = \log A + n \log k + \alpha(\log k)^2 + \dots \quad (6.1)$$

Inflation predicts that successive terms will have rapidly diminishing coefficients, i.e. the deviation from a power-law should be even less than the deviation from scale-invariance. This is generally required by the slow-roll condition, however, hybrid inflationary models and phase transitions during inflation can introduce greater curvature and even rather sharp features into the resulting power spectrum of density perturbations. Hence, one can also consider a free-form primordial power spectrum, to be fitted by eye to the data, and schemes that bin the primordial power into “band-powers” (Wang et al. 1999; Souradeep et al. 1998).

Each cosmogony has transfer functions, $T(k)$ and $C_{\ell k}$. CMB anisotropies are given by

$$C_\ell = \sum_k d \log k C_{\ell k} P_p(k), \quad (6.2)$$

where $C_{\ell k}$ is the radiation transfer function after Bessel transformation into ℓ -space. The matter power spectrum is

$$P(k) = \frac{2\pi^2 c^3}{H_0^3} T^2(k) P_p(k). \quad (6.3)$$

We use the compilations of CMB anisotropy and large-scale structure observations introduced in Chapter 2. For a given $P_p(k)$, we compare predictions with observations using the χ^2 statistic using the analysis method described in Chapter 3. We can vary the coefficients of $P_p(k)$ given in Equation 6.1 to find the best fit for each cosmogony.

Figure 6.1 shows the detailed constraints on the Λ CDM model we adopted in the preceding chapter in order to fit direct observational constraints on cosmological parameters. It appears to have the wrong peak location and shape, but with our newfound freedom in the primordial power spectrum we can imagine changing the effective peak location and shape by adding a “bump” of primordial power near $k = 0.05$. We adopt the parameterization,

$$P_p(k) = Ak \left(1 + A_{bump} \exp \left(-\frac{(\log k - \log k_0)^2}{2(\sigma_k/k_0)^2} \right) \right), \quad (6.4)$$

and find the best-fit parameters $A_{bump} = 1$, $k_0 = 0.06$, and $\sigma_k = 0.03$, i.e. a Gaussian amplification of the primordial power spectrum of width $0.03 h^{-1}\text{Mpc}$ centered at $0.06 h^{-1}\text{Mpc}$

with peak amplification of a factor of 2 versus the best-fit overall normalization A . This is shown in Figures 6.2 and 6.3. The improvement is tremendous, from a χ^2 per degree of freedom of 2.1 to a reduced χ^2 of 1.4 using just three parameters (compared to 70 degrees of freedom in the data). While this is not quite as good of a fit to the structure formation data as CHDM, it is in good agreement with nearly all direct observations of cosmological parameters. Perhaps the primordial power spectrum is radically non-scale-invariant; if so, we appear to have reconciled the previous disagreement between direct parameter observations and the structure formation data. It is, however, a rather undesirable coincidence to be adding primordial power at scales so close to the horizon size at matter-radiation equality, so we will need to confirm this feature with improved future data before arguing that the model is really the answer.

An important consideration at this point is whether our newfound freedom in the primordial power spectrum has radically altered our limits on the neutrino mass of the previous chapter. At least for the Λ CDM+BUMP model, this is not the case, as shown in Figure 6.4, where the addition of HDM rapidly degrades the fit just like before. The impact of a bump in the primordial power spectrum on the CMB predictions of these models is shown in Figure 6.5, which illustrates that the enhancement in power actually helps reach towards the high SK data in the first acoustic peak and is not much higher than the CAT and OVRO measurements at smaller angular scales. Once HDM is added, the shape of the matter power spectrum must be restored with a blue tilt of $n = 1.2$ and this starts to lead to serious disagreement with the COBE results versus the amplitude of smaller-scale observations as discussed in Chapter 5. Once the precision of CMB anisotropy observations improves, it should be quite possible to constrain or detect this sort of enhancement in power on ~ 100 Mpc scales.

6.3 Discussion

This ad-hoc model, although not aesthetic, is physically possible. It could be generated, for example, by incomplete coagulation of bubbles of new phase in a universe that already has been homogenized by a previous episode of inflation (Amendola & Borgani 1994; Baccigalupi et al. 1997). One can tune the bubble size distribution to be sharply peaked at any preferred scale. In this case, voids of the observed sizes of tens of Mpc are sufficient to create roughly the right shape of the matter power spectrum. This results

in nongaussian features and excess power where needed. The non-gaussianity provides a distinguishing characteristic.

Other suggestions that might create such a “bump” appeal to an inflationary relic of excess power from broken scale invariance, arising from double inflation in a Λ CDM model, which results in a spike due to a sharp change in amplitude of the inflaton potential at the desired physical scale (Lesgourgues et al. 1998). This improves the fit in much the same way as adding a hot component to CDM improves the empirical fit. Such ad hoc fits may seem unattractive, but at present they are needed in order to fit the data. Moreover, there are interesting, testable predictions that arise from the tuned void approach. The bubble-driven shells provide a source of overdensities on large scales. Rare shell interactions could produce nongaussian massive galaxies or clusters at low or even high redshift: above a critical surface density threshold gas cooling would help concentrate gas and aid collapse. If massive galaxies were discovered at say $z > 5$ or a massive galaxy cluster at $z > 2$ this would be another indication that the current library of cosmological models is inadequate. If the data are accepted as mostly being free of systematics and ad hoc additions to the primordial power spectrum are avoided, there is no acceptable model for large-scale structure. No one LSS data set can be blamed. New data sets such as SDSS and 2DF are urgently needed to verify whether the shape discrepancies in $P(k)$ will persist; the good news is that the Sloan and 2DF surveys are already acquiring galaxy redshifts.

6.4 The Primordial Power Ratio

Figure 6.6 illustrates the difficulties of the SCDM model in a new form, that of the primordial power spectrum reconstructed from both CMB and large-scale structure data. The biases of redshift surveys in these plots have not been optimized, so it is their shape that is a strong constraint. For SCDM, the CMB is compatible with the scale-invariant primordial power spectrum shown, but the redshift surveys prefer a tilt around $n = 0.8$. Hence the Tilted CDM model is better, but this plot shows that a better fit still can be achieved by letting the scalar spectral index vary from about $n = 1.2$ on COBE scales to $n = 0.8$ around $k = 0.1h/\text{Mpc}$, as found by Gawiser (1998b). This added freedom in the primordial power spectrum makes SCDM a much better fit to the data, just as we have been able to make Λ CDM improve by adding a bump of primordial power. Figure 6.7 shows that a model like CHDM which is already a good fit to the data assuming a scale-invariant

primordial power spectrum is not helped by this added freedom, as a Harrison-Zeldovich form is a good fit to the data on all scales. Figure 6.8 shows the opposite case, however, a model with a very high baryon fraction where the predictions for the peak of the matter power spectrum differ from the data so strongly that there is no shape of the primordial power spectrum that can simultaneously agree with CMB and LSS data on large scales. This model can be falsified without assuming any particular shape for $P_p(k)$. This occurs because CMB anisotropy and large-scale structure data offer us two independent probes of the primordial density fluctuations. When they are sensitive to overlapping spatial scales, their reconstructed primordial power spectra can be compared to form the primordial power ratio, which should equal one on all scales if these density variations came from the same source. Thus with improved high-resolution data we can hope to expand the overlap range of CMB and LSS observations and discriminate among structure formation models using the primordial power ratio, which represents a model-independent method of testing the primordial power spectrum and structure formation models simultaneously.

More formally, the primordial power ratio $R(k)$ is formed from the ratio of these two independent reconstructions of the primordial power spectrum,

$$P_p^M(k) = \frac{H_0^3}{2\pi^2 c^3} \frac{P_p(k)}{T^2(k)} \quad (6.5)$$

and

$$P_p^R(k) = C_{\ell k}^{-1} C_\ell \quad (6.6)$$

where the latter is invertible as long as few enough k bins are desired and the bins have equal logarithmic width in k . We need to force $P_p^R(k)$ to be positive definite and smooth, however, so a regularization method is required. For gravitational instability resulting from passive sources that generate density perturbations long before recombination, $R(k)$ is a very simple function; it should equal one for the entire overlap range of CMB and LSS data where it can be defined.

We have seen that assumptions about the primordial power spectrum make a tremendous difference in testing theories of structure formation. Combining Large-Scale Structure observations with CMB anisotropy data gives us a long lever arm in k -space with which to reconstruct the primordial power spectrum. With the next generation of observations, we hope that our technique will prove powerful enough to either discredit inflation or reconstruct the inflaton potential.

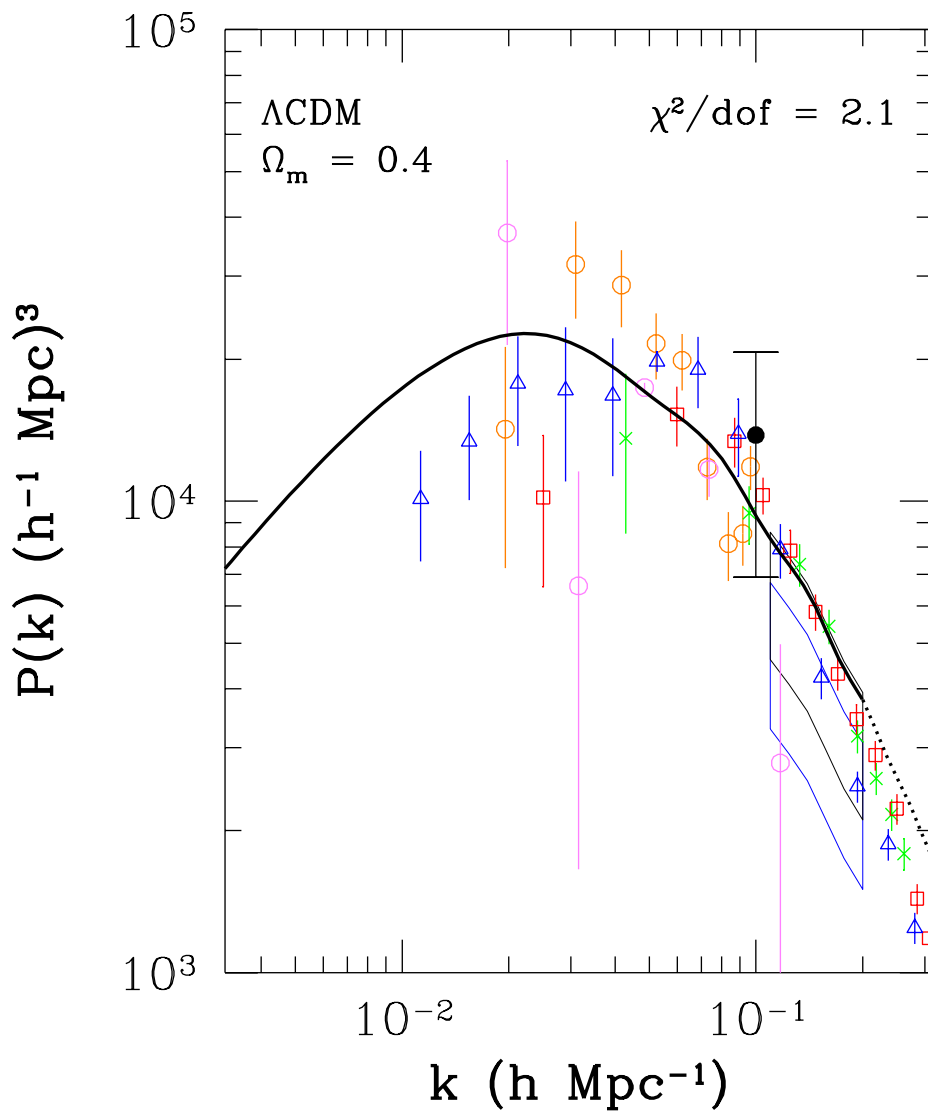


Figure 6.1: Detailed constraints from LSS and CMB on Λ CDM model showing apparent misplacement of peak in the matter power spectrum.

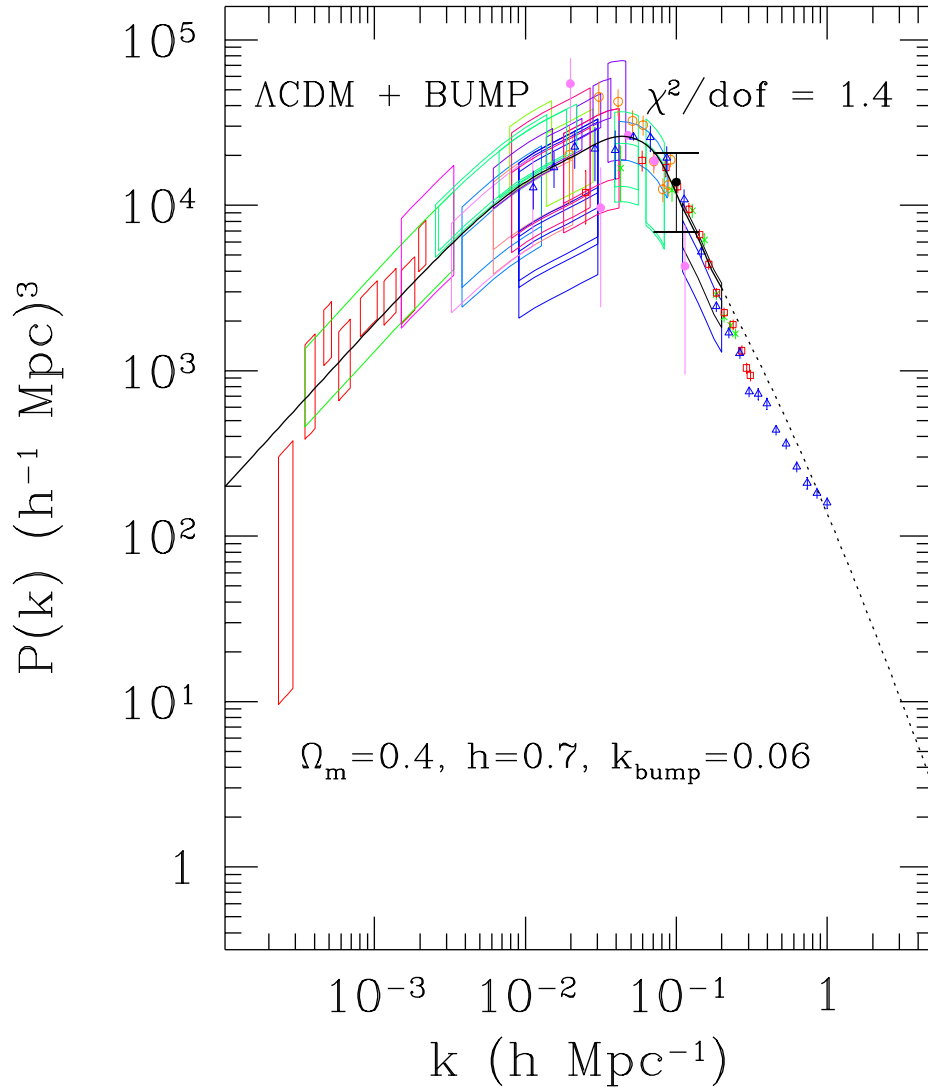


Figure 6.2: Constraints from LSS and CMB on ΛCDM model with a broad enhancement centered at $k = 0.06h^{-1}\text{Mpc}$ added to the primordial power spectrum.

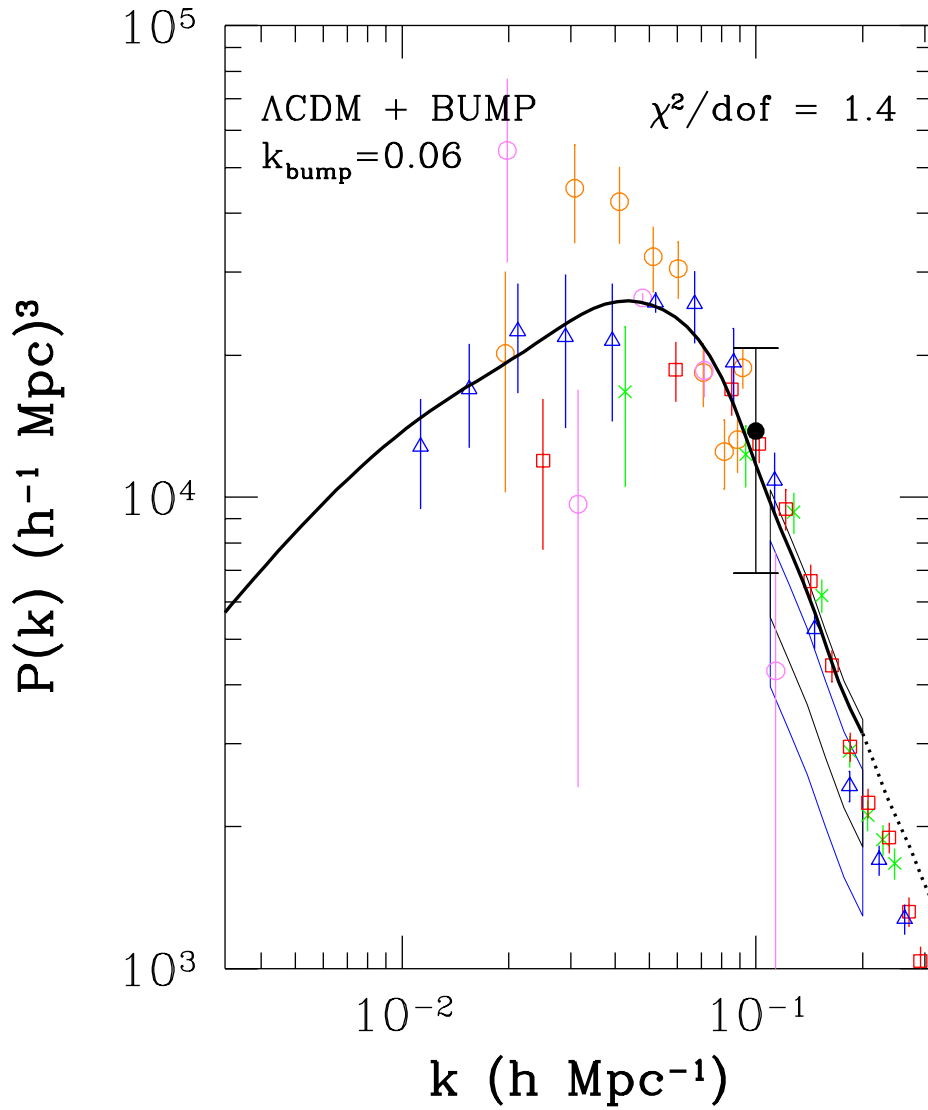


Figure 6.3: Detailed constraints from the peak of the matter power spectrum on ΛCDM model with a broad enhancement centered at $k = 0.06h^{-1}\text{Mpc}$ added to the primordial power spectrum.

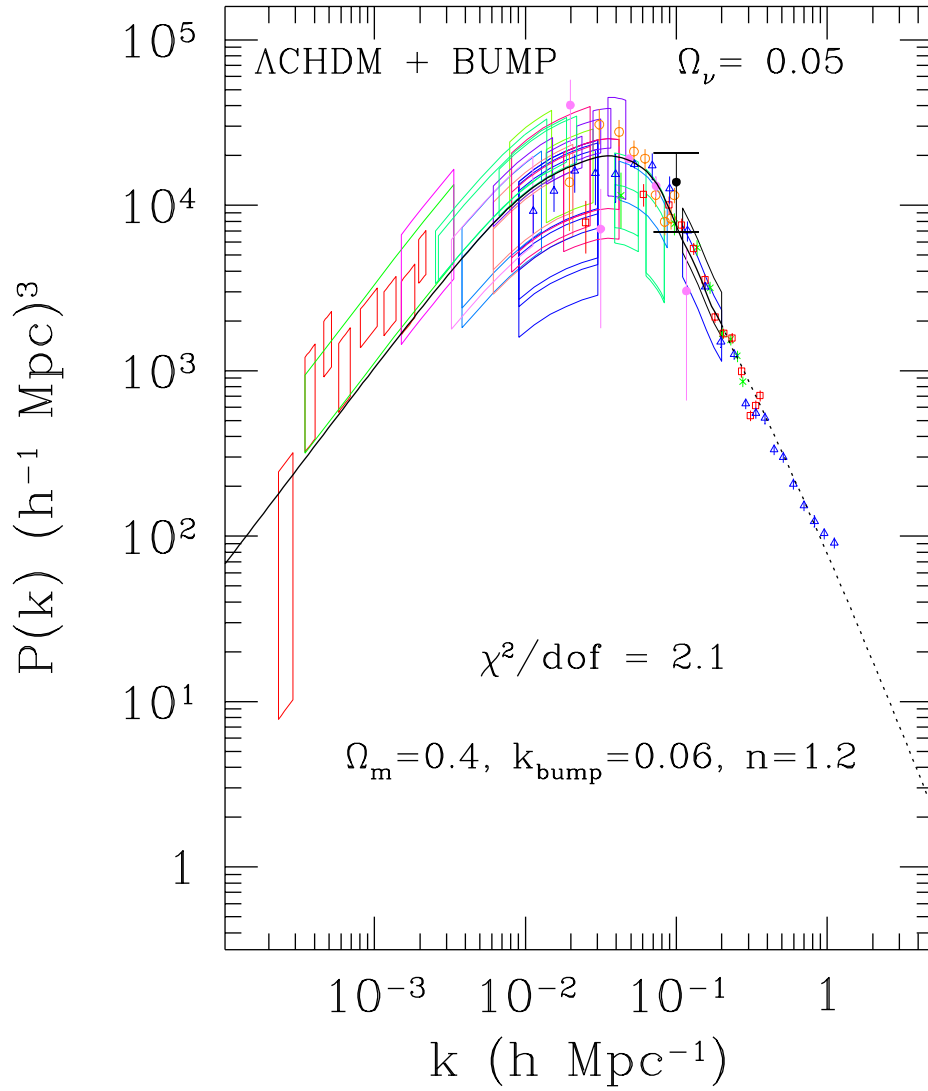


Figure 6.4: Constraints from LSS and CMB on Tilted ΛCHDM model with a broad enhancement centered at $k = 0.06h^{-1}\text{Mpc}$ added to the primordial power spectrum.

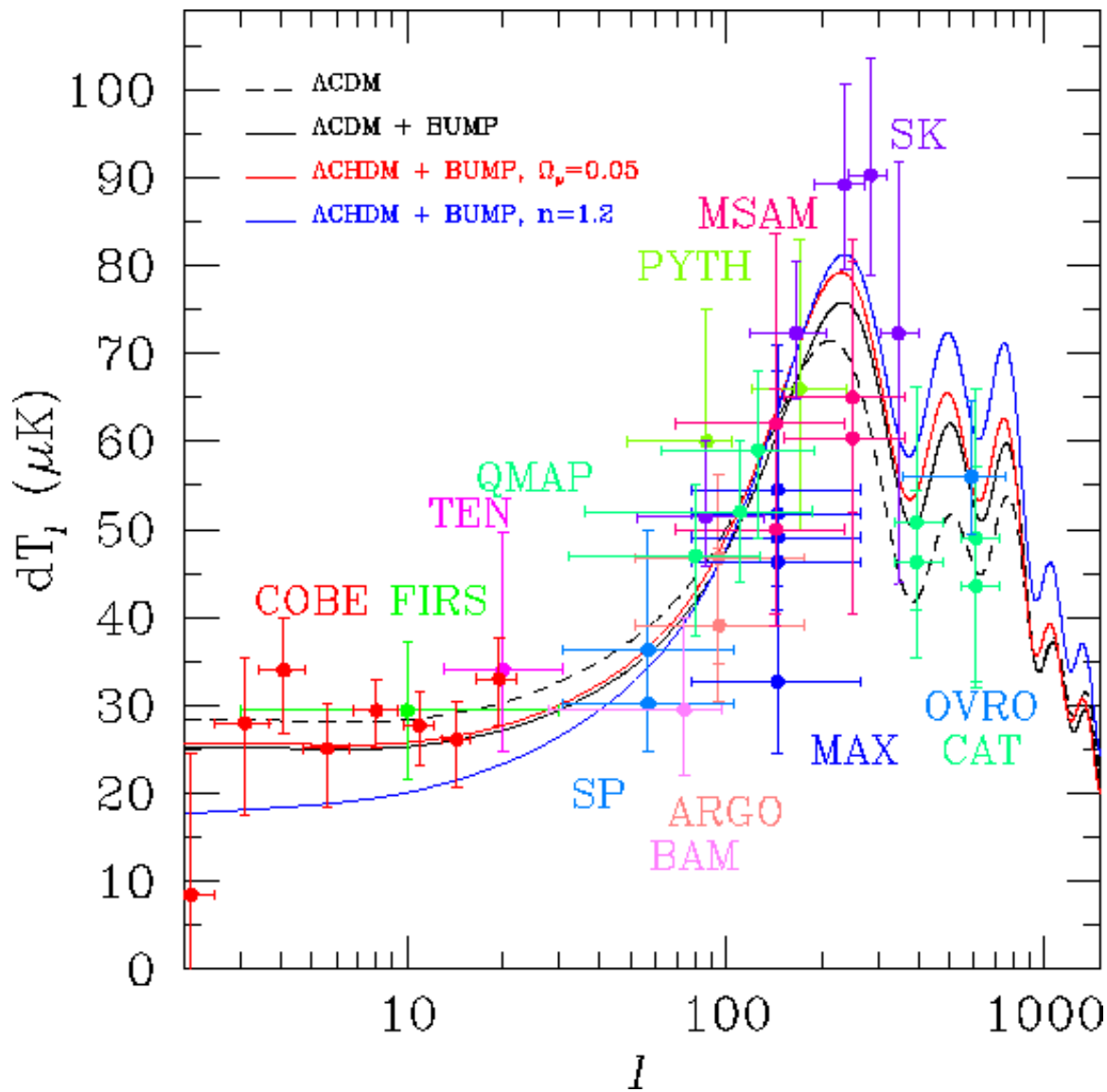


Figure 6.5: Constraints from CMB on tilted Λ CDM + BUMP models.

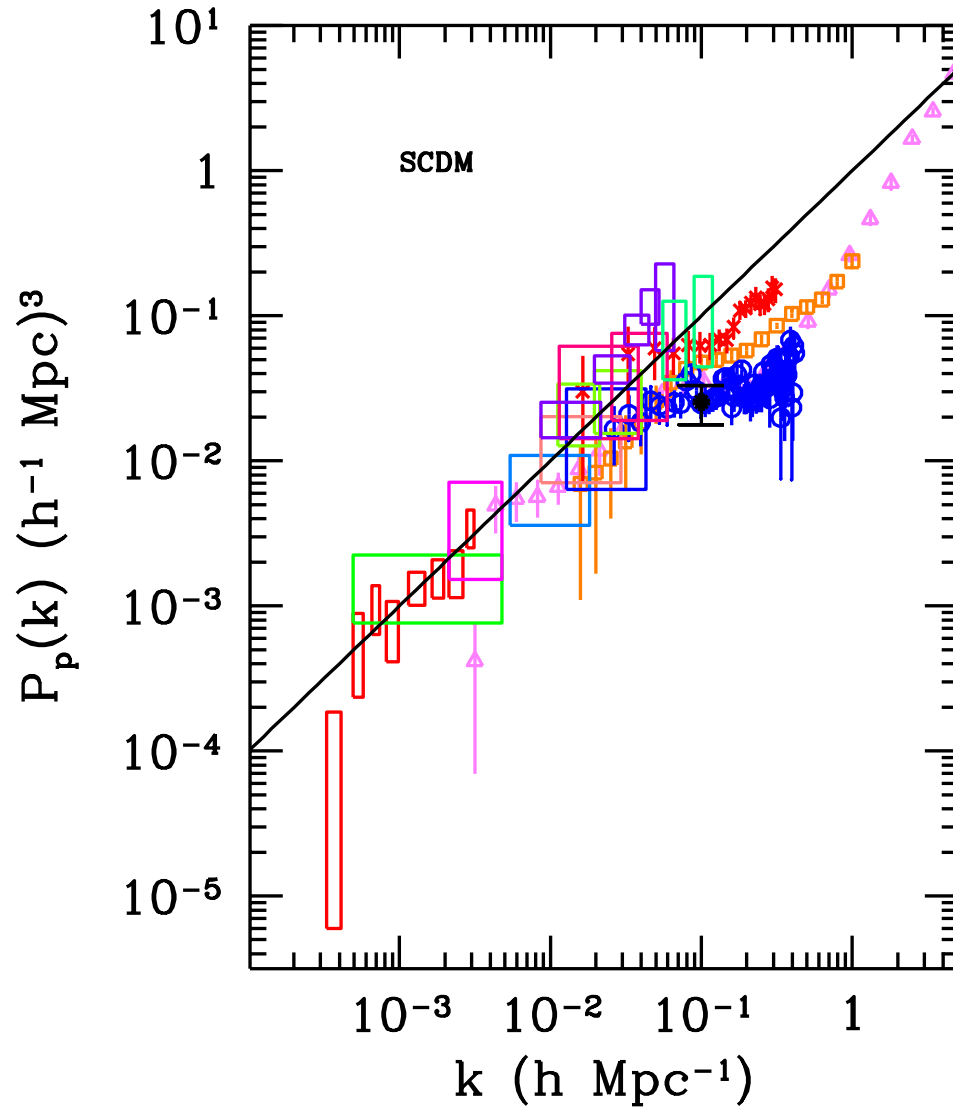


Figure 6.6: Primordial power constraints from LSS and CMB for SCDM model. The solid line is a scale-invariant primordial power spectrum, $n = 1$.

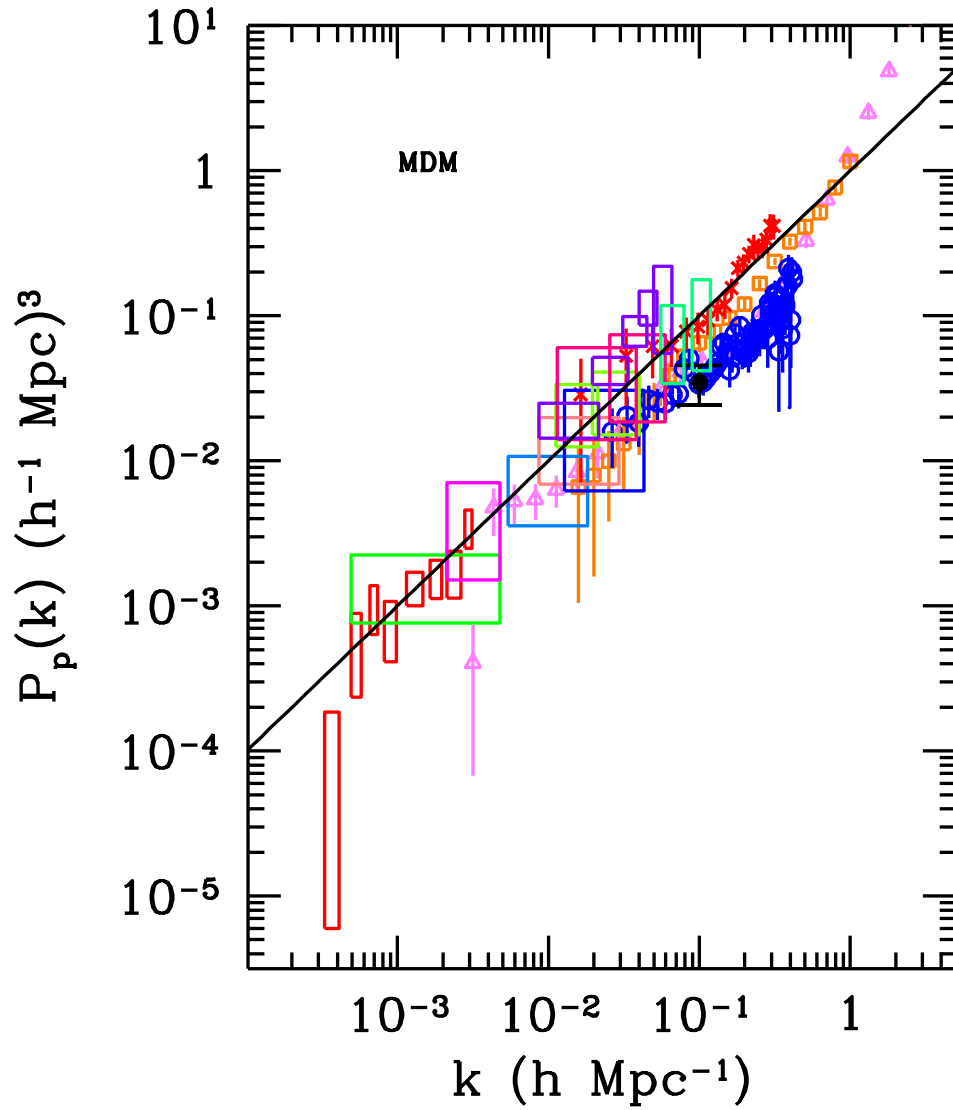


Figure 6.7: Primordial power constraints from LSS and CMB for CHDM model.

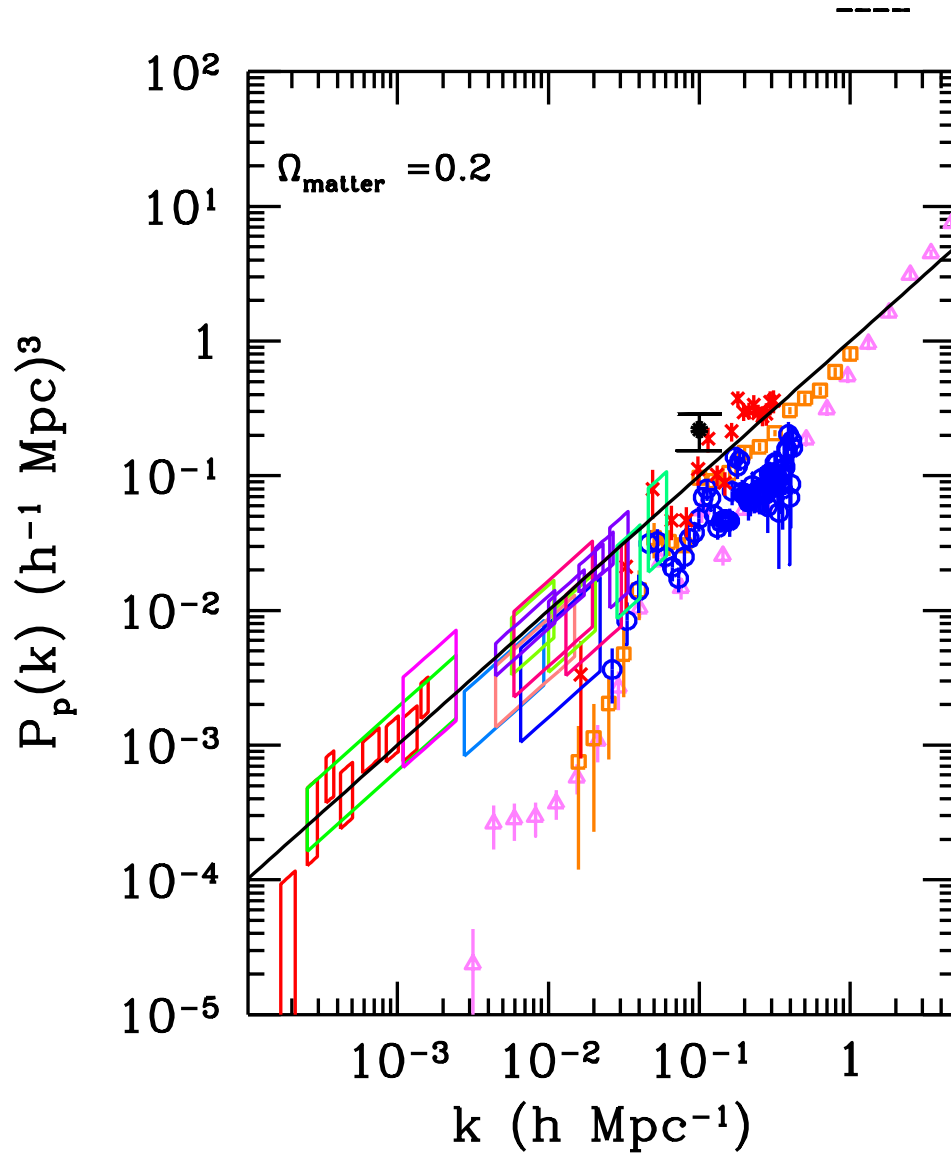


Figure 6.8: Primordial power constraints from LSS and CMB for a high baryon-fraction model similar to BCDM.

Part II

Making Realistic Simulations of the Microwave Sky

Chapter 7

The WOMBAT Challenge

7.1 Motivation

Cosmic Microwave Background (CMB) anisotropy observations during the next decade will yield data of unprecedented quality and quantity. Determination of cosmological parameters to the precision that has been forecast (Jungman et al. 1996; Bond et al. 1997; Zaldarriaga et al. 1997; Eisenstein et al. 1998b) will require significant advances in analysis techniques to handle the large volume of data, subtract foreground contamination, and account for instrumental systematics. To guarantee the accuracy required to improve upon the constraints on models of structure formation that were derived in Part I, we must ensure that the analysis techniques used on these forthcoming high-precision datasets do not introduce unknown biases into the estimation of cosmological parameters.

The Wavelength-Oriented Microwave Background Analysis Team (WOMBAT, see <http://astro.berkeley.edu/wombat>, Gawiser et al. 1998, and Jaffe et al. 1999b) has produced state-of-the-art simulations of microwave foregrounds, using information about the frequency dependence, power spectrum, and spatial distribution of each component. Using the phase information (detailed spatial morphology as opposed to just the power spectrum) of each foreground component offers the possibility of improving upon foreground subtraction techniques that only use the predicted angular power spectrum of the foregrounds to account for their spatial distribution. Most foreground separation techniques rely on assuming that the frequency spectra of the components is constant across the sky, but we provide information on the spatial variation of each component's spectral index whenever possible. The most obvious advantage of this approach is that it reflects our actual sky rather than

just a statistical description of it. With the high precision expected from future CMB maps we must test our foreground subtraction techniques on as realistic a skymap as possible. A second advantage is the construction of a common, comprehensive database for all known CMB foregrounds. The database includes predicted uncertainties in the estimation of the foregrounds. This should prove valuable for all groups involved in measuring the CMB and extracting cosmological information from it. Section 7.2 summarizes methods for generating foreground models which include phase information, and Section 7.3 gives a brief survey of existing subtraction techniques and their limitations.

These microwave foreground models provide the starting point for the WOMBAT Challenge, a “hounds and hares” exercise for which we have simulated skymaps corresponding to various cosmological models and made them available to the cosmology community for analysis without revealing the input parameters. This exercise will test the efficacy of current foreground subtraction, power spectrum analysis, and parameter estimation techniques and will help identify the areas most in need of progress. This challenge is similar to the “Mystery CMB Sky Map challenge” posted by our sister collaboration, COMBAT¹, except that our emphasis is on dealing with realistic foregrounds rather than the ability to analyze large data sets. Our simulations contain CMB anisotropies combined with all major expected foreground components and instrument noise, as described in Section 7.4. Section 7.5 describes our plans to conduct this foreground removal challenge. The WOMBAT Challenge promises to shed light on several open questions in CMB data analysis: What are the best foreground subtraction techniques? Will they allow instruments such as MAP and Planck to achieve the precision in C_ℓ reconstruction which has been advertised, or will the error bars increase significantly due to uncertainties in foreground models? Perhaps most importantly, do some CMB analysis methods produce biased estimates of the radiation power spectrum and/or cosmological parameters?

7.2 Microwave Foregrounds

Phase information is now available for Galactic dust and synchrotron and for the brightest radio galaxies, infrared galaxies, and X-ray clusters on the sky. By incorporating known information on the spatial distribution of the foreground components and spatial variation in their spectral index, we have greatly improved upon previous highly-idealized

¹Cosmic Microwave Background Analysis Tools, <http://cfpa.berkeley.edu/group/cmbanalysis>

foreground models.

There are four major expected sources of Galactic foreground emission at microwave frequencies: thermal emission from dust, electric or magnetic dipole emission from spinning dust grains (Draine & Lazarian 1998a,b, 1999), free-free emission from ionized hydrogen, and synchrotron radiation from electrons accelerated by the Galactic magnetic field. Good spatial templates exist for thermal dust emission (Schlegel et al. 1998) and synchrotron emission (Haslam et al. 1982), although the 0.5 resolution of the Haslam maps means that smaller-scale structure must be simulated or ignored. Extrapolation to microwave frequencies is possible using maps which account for spatial variation of the spectra (Finkbeiner et al. 1999; Platania et al. 1998). The COMBAT collaboration has recently posted a software package called FORECAST² that displays the expected dust foreground for a given frequency, location, and observing strategy. Our best-fit foreground maps will be added to this user-friendly site in the near future, and this should be a useful resource for planning and simulating CMB anisotropy observations.

A spatial template for free-free emission based on observations of H α (Smoot 1998; Marcelin et al. 1998) can be created in the near future by combining WHAM observations (Haffner et al. 1998) with the southern celestial hemisphere H-Alpha Sky Survey (McCullough et al. 1999). While it is known that there is an anomalous component of Galactic emission at 15-40 GHz which is partially correlated with dust morphology (Kogut et al. 1996b; Leitch et al. 1997; de Oliveira-Costa et al. 1997), it is not yet clear whether this is spinning dust grain emission or free-free emission somehow uncorrelated with H α observations. In fact, spinning dust grain emission has yet to be observed directly (see, however, de Oliveira-Costa et al. 1999), so the uncertainties in its amplitude are tremendous. A template for free-free emission can be derived from DMR data but has tremendous uncertainties. A better choice is to use the Galactic dust template multiplied by the appropriate correlation coefficient at a given frequency as a template, but this yields no information on any portion of “anomalous” emission that may be uncorrelated with the structure of Galactic dust.

There exist three nearly separate categories of galaxies that also generate microwave foreground emission; they are radio-bright galaxies, low-redshift infrared-bright galaxies, and high-redshift infrared-bright galaxies. The level of anisotropy produced by

²Foreground and CMB Anisotropy Scan Simulation Tools,
<http://cfpa.berkeley.edu/forecast>

these foregrounds is predicted by Toffolatti et al. (1998) using models of galaxy evolution to produce source counts. Updated models calibrated to recent SCUBA observations are also available (Blain et al. 1998b; Scott & White 1999). For the high-redshift galaxies detected by SCUBA, no spatial template is available, so a simulation of these galaxies with realistic clustering will be necessary. Scott & White and Toffolatti et al. have used very different estimates of clustering to produce divergent results for its impact, so this issue will need to be looked at more carefully. Upper and lower limits on the anisotropy generated by high-redshift galaxies and as-yet-undiscovered types of point sources are given in Chapter 10 using recent observations over a wide range of microwave frequencies. We will need to look for these sources with direct observations and design analysis techniques that might manage to subtract them. The 5319 brightest low-redshift IR galaxies detected at $60\mu\text{m}$ are contained in the IRAS 1.2 Jy catalog (Fisher et al. 1995) and can be extrapolated to 100 GHz with a systematic uncertainty of a factor of a few (see Chapter 8). Chapter 9 discusses the catalog of 2207 bright radio sources which has been compiled by Sokasian et al. (1998). This catalog appears to contain the few hundred brightest sources in the full sky, but at lower fluxes it contains very few sources from the Southern Celestial Hemisphere. We have fixed this deficit by including roughly a thousand sources from the Parkes-MIT-NRAO catalog (Griffith & Wright 1993) in our simulations (see Section 9.5).

The secondary CMB anisotropies that occur when the photons of the Cosmic Microwave Background radiation are scattered after the original last-scattering surface can also be viewed as a type of foreground contamination (see discussion in Chapter 1 for details). The shape of the blackbody spectrum can be altered through inverse Compton scattering by the thermal Sunyaev-Zeldovich (SZ) effect (Sunyaev & Zeldovich 1972). The effective temperature of the blackbody can be shifted locally by a Doppler shift from the peculiar velocity of the scattering medium (the kinetic SZ and Ostriker-Vishniac effects) as well as by passage through nonlinear structure (the Rees-Sciama effect). Simulations have been made of the impact of the SZ effects in large-scale structure (Persi et al. 1995), clusters (Aghanim et al. 1997), groups (Bond & Myers 1996) and reionized patches (Aghanim et al. 1996; Knox et al. 1998; Gruzinov & Hu 1998; Peebles & Juszkievicz 1998). The brightest 200 X-ray clusters are known from the XBACS catalog and can be used to incorporate the locations of the strongest SZ sources (Refregier et al. 1998, see Chapter 11). The SZ effect itself is independent of redshift, so it can yield information on clusters at much higher redshift than does X-ray emission. However, nearly all clusters are unresolved for

$10'$ resolution, so higher-redshift clusters occupy less of the beam and therefore their SZ effect is in fact dimmer. In the $4.5'$ channels of Planck this will no longer be true, and SZ detection and subtraction becomes more challenging and potentially more fruitful as a probe of cluster abundance at high redshift.

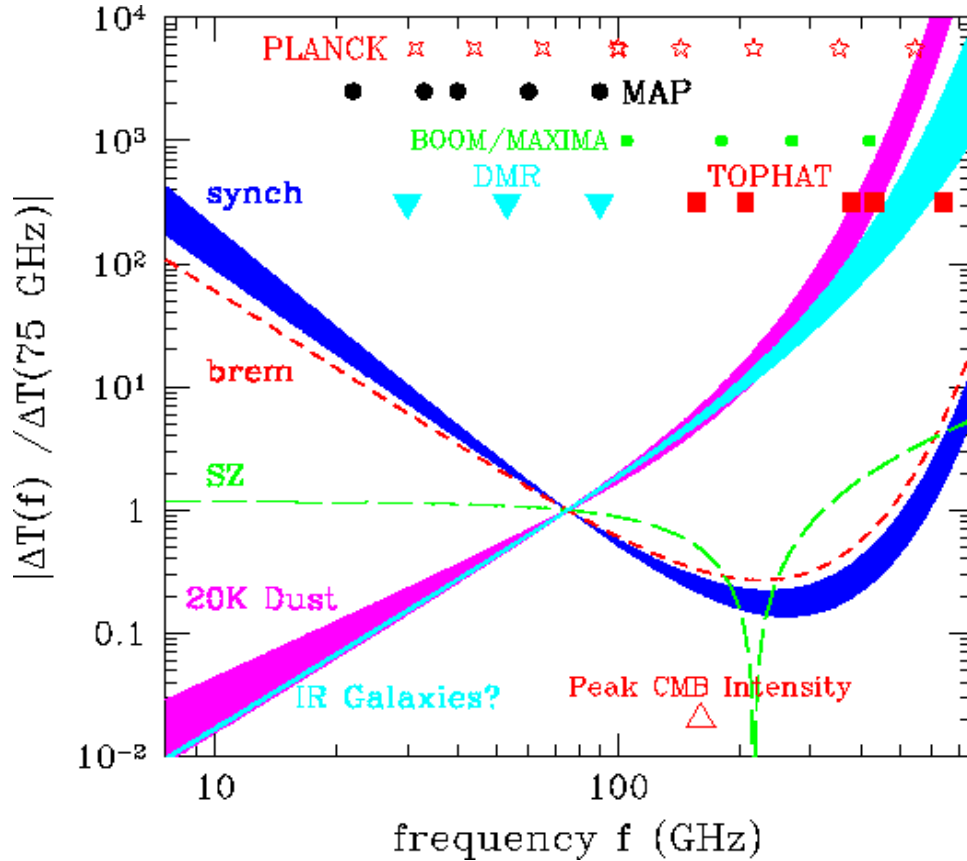


Figure 7.1: Frequency spectra of microwave foregrounds.

7.3 Reducing Foreground Contamination

Figure 7.1 illustrates the spectra, normalized at 75 GHz, of the various foreground components which are expected to contribute significantly to microwave anisotropy. The frequencies of several current and future observing instruments are shown; the amplitude of Galactic foregrounds will decrease at higher resolution whereas the amplitude of extragalactic point sources will increase. Radio galaxies have similar spectra to those shown for synchrotron and brehmsstrahlung emission. The expected minimum of all foreground con-

tamination is near 100 GHz. Various methods have been proposed for reducing foreground contamination. For point sources, it is possible to mask pixels which represent positive 5σ fluctuations since such fluctuations are highly unlikely for Gaussian-distributed CMB anisotropy and Gaussian-distributed instrument noise and can be assumed to be caused by point sources. This pixel masking technique can be improved somewhat by filtering (Tegmark & De Oliveira-Costa 1998; see Tenorio et al. 1999 for a different technique using wavelets). Chapter 9 demonstrates that using prior information from good source catalogs may allow the masking of pixels which contain sources brighter than the 1σ level of CMB fluctuations and instrument noise. For the 90 GHz MAP channel, this could reduce the residual radio point source contamination by a factor of two, which might significantly reduce systematic errors in cosmological parameter estimation. Galactic foregrounds with well-understood frequency spectra can be projected out of multi-frequency observations on a pixel-by-pixel basis (Brandt et al. 1994; Dodelson & Stebbins 1994; Dodelson & Kosowsky 1995; Dodelson 1997). Prior information in the form of spatial templates can be included in this projection, but uncertainty in the spectral index is a cause for concern.

Perhaps surprisingly, the methods for foreground subtraction which have the greatest level of mathematical sophistication and have been tested most thoroughly ignore the known locations on the sky of some foreground components. The multi-frequency Wiener filtering approach uses assumptions about the spatial power spectra and frequency spectra of the foreground components to perform a separation in spherical harmonic or Fourier space (Tegmark & Efstathiou 1996; Bouchet et al. 1999; Bouchet & Gispert 1999; Knox 1999b). However, it does not include any phase information at present. The Fourier-space Maximum Entropy Method (Hobson et al. 1998) can add phase information on diffuse Galactic foregrounds in small patches of sky but treats extragalactic point sources as an additional source of instrument noise, with good results for simulated Planck data (Hobson et al. 1998) and worrisome systematic difficulties for simulated MAP data (Jones et al. 1998). Maximum Entropy has not yet been adapted to handle full-sky datasets. Both methods have difficulty if pixels are masked due to strong point source contamination or the spectral indices of the foreground components are not well known (Tegmark 1998).

Since residual foreground contamination can increase uncertainties and bias parameter estimation, it is important to reduce it as much as possible. Current analysis methods usually rely on cross-correlating the CMB maps with foreground templates at other frequencies (see de Oliveira-Costa et al. 1997 and Jaffe et al. 1999a). It is clearly su-

terior to have region-by-region (or pixel-by-pixel) information on how to extrapolate these templates to the observed frequencies; otherwise this cross-correlation only identifies the emission-weighted average spectral index of the foreground from the template frequency to the observed frequency.

Because each foreground has a non-Gaussian temperature distribution, the covariance matrix of its expected $a_{\ell m}$ coefficients is not diagonal. When a known foreground template is subtracted from a CMB map, it is inevitable that the correlation coefficient used for this subtraction will be slightly different than the true value. This expected under- or over-subtraction of each foreground leads to off-diagonal structure in the “noise” covariance matrix of the remaining CMB map, as opposed to the contributions of expected CMB anisotropies and uncorrelated instrument noise, both of which give diagonal contributions to the covariance matrix of the $a_{\ell m}$. Thus incomplete foreground subtraction, like $1/f$ noise, can introduce non-diagonal correlations into the covariance matrix of the $a_{\ell m}$. These correlations complicate the likelihood analysis necessary for parameter estimation (Knox 1999b). Chapter 12 presents a foreground subtraction method that attempts to account for these correlations in pixel space. Having phase information on the brightness and spectral index of foreground emission should reduce inaccuracies in foreground subtraction, and this motivates us to produce the best estimates we can of these quantities along with estimates of their uncertainties.

The Wavelength-Oriented Microwave Background Analysis Team is dedicated to generating the best possible predictions of microwave emission from Galactic and extragalactic sources along with a clear description of the uncertainties. Those predictions and uncertainties were used in generating the WOMBAT Challenge Simulations, and they are ready to be applied to real-world data as well. We have made our “best-fit” knowledge of the various foreground components available to the public, and each best-fit foreground map (or list of predicted point source fluxes) is accompanied by a map (or list) of its uncertainties and a discussion of possible systematic errors³. Each simulation of that foreground will be different from the best-fit map based upon a realization of those uncertainties. This simulates the real observing process in a way not achieved by previous foregrounds simulations. Observational teams that wish to download our predictions for use in masking pixels, cross-correlating, and subtracting foreground contamination from microwave data

³see <http://astro.berkeley.edu/wombat/foregrounds.html>

are encouraged to do so.

7.4 The WOMBAT Challenge Simulations

We produced simulations analogous to high-resolution balloon observations (e.g. MAXIMA and BOOMERANG; see Hanany et al. 1997 and de Bernardis & Masi 1998) as well as the MAP satellite. We have used the publicly available HEALPIX package of pixelization and analysis routines⁴ for CMB simulation, beam convolution, and basic power spectrum analysis of full-sky maps. We modified several of the routines to input and output files of $a_{\ell m}$ in addition to C_ℓ and to create constrained realizations of CMB anisotropy. We also created basic new routines which bin a HEALPIX map down to a lower level of resolution and perform a weighted sum of several maps.

Our skymaps contain simulated foreground emission from the Galaxy (thermal dust emission, synchrotron, free-free emission, spinning dust grains) and extragalactic sources (radio- and infrared-bright galaxies and the Sunyaev-Zeldovich effect from hot gas in galaxy clusters). Except for a few intentional minor surprises, they are well described by the WOMBAT foreground predictions. Each simulation has foreground contamination which is reasonable given our best-fit models and their uncertainties.

All simulated skymaps have an average of zero (up to slight rounding errors). This simulates the insensitivity of MAP's differential radiometers to the monopole and MAXIMA's subtraction of the average value over time to eliminate $1/f$ noise. The practical effect of this is that for full-sky simulated MAP maps the Galactic plane is bright and positive and the rest of the sky is negative. To see CMB fluctuations (and even instrument noise), it is necessary to use asymmetric minimum and maximum values when displaying the map, especially at low frequencies where the Galaxy is very bright. For the MAXIMA patches, which are at high Galactic latitude where the Galactic emission is much less, setting the average value in the $10^\circ \times 10^\circ$ degree patch to zero has fixed this, and a symmetric color table allows one to see the CMB and instrument noise rather well.

We have not subtracted the dipole from the final maps, but the simulated CMB component has no dipole and the reflex dipole of the Local Group's motion relative to the CMB frame has not been added. In principle, one can therefore use the remaining dipole in the full-sky maps to learn about the foregrounds alone, particularly the Galaxy since the

⁴<http://www.tac.dk/~healpix>

Galactic center is much brighter than the anti-center. This is realistic, since the best fit detection and subtraction of the CMB reflex dipole usually ignores low Galactic latitude and thus allows a Galactic-emission dipole to be analyzed.

7.4.1 Constrained Realizations of CMB Anisotropy

In choosing cosmological models to use for the WOMBAT simulations, we assumed that adiabatic CDM is probably correct but surprises are always possible. Figure 7.2 shows a simulation of CMB anisotropy from the WOMBAT Challenge simulations for a $28'$ beam for the 40 GHz channel of the MAP satellite. This is a constrained realization generated using the method of Bunn et al. (1994), i.e. if smoothed on 7° scales it will roughly match the Wiener filtered COBE DMR map. This is a necessary step of making the most realistic microwave sky simulation possible, since we already know from COBE about the fluctuations in CMB intensity on 7° scales. However, the Wiener-filtered version has a lot less information than the DMR 4-year map might appear to, and there is not yet any indication that having this low- ℓ constraint will prove useful in data analysis. The Wiener filtered map consists of best-fit values and uncertainties in each low- ℓ $a_{\ell m}$, so a simulation consists of adding a realization of these uncertainties to the Wiener filtered map and then generating Gaussian random $a_{\ell m}$ according to the C_ℓ of a given model for all $\ell > 30$ since COBE yields no information on those scales. The C_ℓ of the model being considered are used to perform the Wiener filtering process, as changing the assumed level of signal changes the resulting Wiener filtered map, and we want to be sure that the C_ℓ of the resulting simulation will be smooth around $\ell = 30$ where the transition from large-uncertainty Wiener-filtered coefficients to purely Gaussian random realization occurs. No smaller-scale CMB observations have been used as constraints.

7.4.2 Instrument Noise and Beam Convolution

All skymaps are of temperature fluctuations measured in thermodynamic microKelvin, i.e. variations about the central CMB blackbody with temperature 2.73 K. Instrument noise is also given in thermodynamic μK , hence there is a significant rise in noise in the 390 GHz MAXIMA channel where the blackbody of the CMB is dropping rapidly. The expected bandwidths of the MAP channels are 20%, well-approximated by a tophat in frequency response. The expected bandwidths of the MAXIMA channels are

30%, better approximated by a Gaussian. However, except for extreme spectral behaviors, these bands are well approximated by their central frequency, and we have done so. The resulting error is far smaller than several other sources of systematic uncertainty. The instrument noise is a Gaussian realization, uncorrelated between pixels. For MAXIMA, the noise is uncorrelated and uniform across the map, which is a gross simplification of real-world MAXIMA data. For MAP, we have used a weight map generated using the planned MAP observing strategy to determine the noise variance⁵.

We used beamsize uncertainties of $\pm 1'$ for the Full Width Half Maximum for the three MAXIMA frequencies and slightly different central values for FWHM at each frequency. This is an attempt to model the real-world uncertainty in beam size that is typical for high-precision balloon-borne experiments. Beam calibration using planets and bright point sources should allow the FWHM to be determined to about 10% at each frequency, and the calibrated value will not necessarily be the same at each frequency.

The MAXIMA maps are a gnomonic projection of a $10^\circ \times 10^\circ$ patch of sky centered at Galactic coordinates $(90^\circ, 50^\circ)$ read from a full-sky simulation of CMB anisotropy and foregrounds in HEALPIX pixelization. The instrument noise, however, is realized independently in each of the $4.5'$ width pixels of the 128×128 array. This simulation covers the same patch of sky as the recent MAXIMA flight. Since we are including the known foregrounds on that particular patch of sky in our simulation, this is a very good approximation of the real data set taken by MAXIMA, except that we have modelled the instrument noise as uncorrelated whereas the noise correlations in the real data set are considerable. The gnomonic projection should be flat enough to approximate this patch of sky as 2-dimensional at the 1% level, so two-dimensional Fast Fourier Transforms are a feasible analysis method.

7.4.3 Galactic foregrounds

We have used the best existing map of Galactic dust emission, the $100\mu\text{m}$ emission map of Schlegel et al. (1998). This map has $6'$ resolution and the method of extrapolating it to microwave frequencies was derived using comparison with FIRAS data (Finkbeiner et al. 1999). We use a destriped, point-source-subtracted Haslam map at 408 MHz (Haslam et al. 1982) to determine the synchrotron emission, with maps at 1.4 (Reich & Reich 1988) and 2.3 GHz (Jonas et al. 1998) used to determine the synchrotron spectral index as a

⁵ All information used for MAP, including frequencies, beam sizes, observing strategy, and expected instrument noise, is as shown at <http://map.gsfc.nasa.gov>

function of frequency (see Davies et al. 1996 for cautionary notes). We do not add small-scale structure to this template, since we find that the Haslam maps are smooth enough on their smallest scales that adding simulated structure at higher resolution is unnecessary. The typical method of doing so (Bouchet et al. 1994) involves adding Gaussian random $a_{\ell m}$ which obey the extrapolated power spectrum of synchrotron. This is a poor approximation to the highly correlated phases necessary to construct typical Galactic structure, which is filamentary and therefore highly non-Gaussian. Free-free and spinning dust grain emission with the appropriate spectra were simulated using templates of the dust map and a model of the Local Bubble.

7.4.4 Extragalactic foregrounds

We have put known bright radio and IRAS galaxies and SZ clusters in their proper places on the sky, instead of relying on number counts alone and placing the sources using Poissonian clustering. The real clustering of these sources is thus contained in our models, and it is possible to use knowledge of their locations to mask the pixels containing them. This allows better point source subtraction than does a simple 5σ cutoff. Chapters 8 and 9 describe the process of simulating the microwave contribution from low-redshift infrared-bright galaxies and radio galaxies, respectively. Chapter 11 describes our predictions for the Sunyaev-Zeldovich effect from galaxy clusters and filaments.

We have also included realistic simulations of the numerous high-redshift infrared-bright galaxies whose number counts at 353 GHz were recently determined by SCUBA (Smail et al. 1997). We have simulated their non-Poissonian clustering as well. The population of high-redshift galaxies detected in the sub-mm by SCUBA appears to be the main source of the Far-Infrared Background radiation. Except for the source counts in the flux range seen by SCUBA, little is known about their overall $N(S)$ law, their redshift distribution, or the amplitude of their clustering. The model by Tan et al. (1999) is consistent with observations across a wide range of frequencies and is therefore our current model for predicting source counts as a function of flux and redshift. Alternative models from Blain et al. (1998b), Guiderdoni et al. (1998), and Toffolatti et al. (1998) give a sense of the systematic uncertainties in these models. SCUBA observations constrain $N(S)$ around its break, and the low-flux end is constrained by the level of integrated background radiation. However, the high-flux end is responsible for the vast majority of microwave anisotropy

and it is not yet well constrained because SCUBA has surveyed a very small portion of the sky. Thus there is no available spatial template for these sources, and there are tremendous systematic uncertainties in their number counts and clustering.

An upper limit on the clustering of these sources and its implications for microwave foreground anisotropy is given by Scott & White (1999). They assume that high-redshift infrared-bright galaxies cluster like Lyman break galaxies, even though the Lyman break galaxies are selected using a technique that only allows them to have a narrow redshift distribution. The redshift distribution of high-redshift infrared-bright galaxies is undoubtedly broader, leading us to estimate that their clustering $w(\theta)$ will be between a factor of 4 and 10 less than that assumed by Scott & White. As the amount of sky surveyed by SCUBA increases, an empirical determination of the clustering of these sources will narrow this range of uncertainty. Section 13.1 discusses the prospects for better determining the bright end of the number counts with forthcoming instruments.

Another significant source of uncertainty in predicting these sources' contribution to anisotropy as a function of frequency is that of extrapolation. The 353 GHz (850 μm) detections by SCUBA are almost definitely on the Rayleigh-Jeans side of the peak of their graybody emission, but not at low enough frequencies for the spectrum to be a pure power-law. Thus, although we expect the emissivity of these sources to be between 1 and 2, which leads to a Rayleigh-Jeans spectral index between 3 and 4, their effective spectral index above 100 GHz should be closer to 3, with an uncertainty of 0.5. The spectral index of each source will vary somewhat around this average depending on the specific nature of its emitting dust, with a source-by-source uncertainty again around 0.5. Note, however, that a typical CMB observation pixel receives roughly equal contributions from its several brightest high-redshift infrared-bright sources, so the pixel-to-pixel variation will be less than this except for pixels dominated by a single unusually bright source. Very little is known about the spatial location of high-redshift infrared-bright galaxies, hence the rough characteristics of these high-redshift foreground sources but not their simulated locations have been revealed as part of our foreground predictions.

Figure 7.3 shows our simulation of Galactic and extragalactic foregrounds for the MAP 40 GHz channel at $28'$. Temperature fluctuations are given in thermodynamic μK , with the maximum and minimum at the expected level of $\pm 5\sigma$ fluctuations. The Galaxy dominates at low latitude but strong extragalactic point sources (convolved with the beam) are visible. The SZ decrement is strong enough for a few clusters to turn the otherwise

strong Galactic contamination into a temperature decrement. The WOMBAT Challenge consists of 5 simulated MAP datasets and 5 simulated MAXIMA datasets. Each model has underlying CMB anisotropies corresponding to a particular cosmology, and each contains a different realization of the foreground contamination within the uncertainties of our best-fit foreground models. Figure 7.4 shows one of the WOMBAT simulations for the MAP 50 GHz channel at $28'$, including CMB anisotropy, instrument noise, and Galactic and extragalactic foreground emission. Figure 7.5 shows one of the $10^\circ \times 10^\circ$ MAXIMA simulations at 150 GHz, $11'$ FWHM. This also includes CMB anisotropy, instrument noise, and Galactic and extragalactic foreground emission. The axis labels are pixel numbers within the 128×128 array. Notice the bright point source in the upper left quadrant (40,80); this is the only one of the MAXIMA simulations with such a bright source, which means that it is either a simulated high-redshift galaxy or a known IR-bright or radio-bright galaxy where the realized systematic and statistical errors led to a much higher flux than its predicted value.

7.5 A “Hounds and Hares” Exercise for Cosmology

Our purpose in conducting a “hounds and hares” exercise is to simulate the process of analyzing microwave skymaps as accurately as possible. In real-world observations the underlying cosmological parameters and the exact amplitudes and spectral indices of the foregrounds are unknown, so Nature is the hare and cosmologists are the hounds. We provided a calibration map of CMB anisotropy with a disclosed angular power spectrum (SCDM) in January 1999 so that participants could test the download procedure and become familiar with HEALPIX. The WOMBAT Challenge began on March 15, 1999 with the release of our simulated microwave skymaps on the World Wide Web. Participating groups have four months to analyze the skymaps, subtract the foregrounds and extract cosmological information. Options for reporting results include generating maps of the input CMB and/or foreground components, plotting C_ℓ spectra of these components, and specifying the input cosmological parameters that correspond to the CMB anisotropies in each simulated universe.

Two prizes will be given: a case of champagne to the team or individual who best determines the CMB anisotropy power spectrum and cosmological parameters of each model, and a stuffed animal (guess which kind!) to the team or individual that can determine the most information about the Galactic and extragalactic foreground sources for each

model. The fortnight between the end of the Challenge on July 15, 1999 and the announcement of input parameters on August 1, 1999 will be used to ensure that we understand the answers provided to us. Participants are encouraged to publish any research progress they make as a result of participation, such as algorithms and analysis methods. We ask that participants provide us with a brief description of the analysis techniques they have used. We will publish a summary of the results, indicating which methods of foreground subtraction and parameter estimation appear to be the most successful at present and how well they work. Participants may choose to remain anonymous in our presentation of the results.

7.6 Discussion

One of the biggest challenges in real-world observations is being prepared for surprises, both instrumental and astrophysical (see Scott 1998 for an eloquent discussion). An exercise such as the WOMBAT Challenge is an excellent way to simulate these surprises, and we have included a few in our skymaps. We hope that the results of the WOMBAT Challenge will provide estimates of the effectiveness of current techniques of foreground subtraction, power spectrum analysis, and parameter estimation.

It is unclear how close the community is to being able to handle datasets as large as that of MAP (10^6 pixels at $13'$ resolution for a full-sky map). Given current computing power, complex algorithms appear necessary for analyzing full-sky MAP datasets (Oh et al. 1999), although simpler approximations may be possible (e.g. Wandelt et al. 1998). Even the algorithm of Oh et al. has yet to be tested on the slightly correlated instrument noise which will be present in the real MAP datasets (our simulations contain uncorrelated noise so they will not alleviate this concern).

Undoubtedly the most important scientific contribution of WOMBAT is the production of realistic full-sky maps of all major microwave foreground components with estimated uncertainties. These maps are needed for foreground subtraction and estimation of residual foreground contamination in present and future CMB anisotropy observations. They will allow instrumental teams to conduct realistic simulations of the observing and data analysis process without needing to assume overly idealized models for the foregrounds. By combining various realizations of these foreground maps within the stated uncertainties with a simulation of the intrinsic CMB anisotropies, we have produced the best simulations

so far of the microwave sky. Using these simulations in a “hounds and hares” exercise should test how well the various foreground subtraction and parameter estimation techniques work at present. It is easy to question the existing tests of analysis methods which assume idealized foregrounds in analyzing similarly idealized simulations.

Data analysis techniques will undoubtedly improve with time, and we hope to reduce the current uncertainty in their efficacy such that follow-up simulations by the instrumental teams themselves can generate confidence in the results of real observations. We can test the resilience of CMB analysis methods to surprises such as unexpected foreground amplitude or spectral behavior, correlated instrument noise, and CMB fluctuations from non-gaussian or non-inflationary models. Cosmologists need to know if such surprises can lead to the misinterpretation of cosmological parameters. In the future, we envision producing time-ordered data, simulating interferometer observations, and adding polarization to our microwave sky simulations.

Perhaps the greatest advance we offer is the ability to evaluate the importance of studying the detailed locations of foreground sources. If techniques which ignore this phase information are still successful on our realistic sky maps, that is a significant vote of confidence. Alternatively, it may turn out that techniques which use phase information are needed in order to reduce foreground contamination to a level which does not seriously bias the estimation of cosmological parameters. Combining various techniques may lead to improved foreground subtraction methods, and we hope that a wide variety of techniques will be tested by the participants in the WOMBAT Challenge.

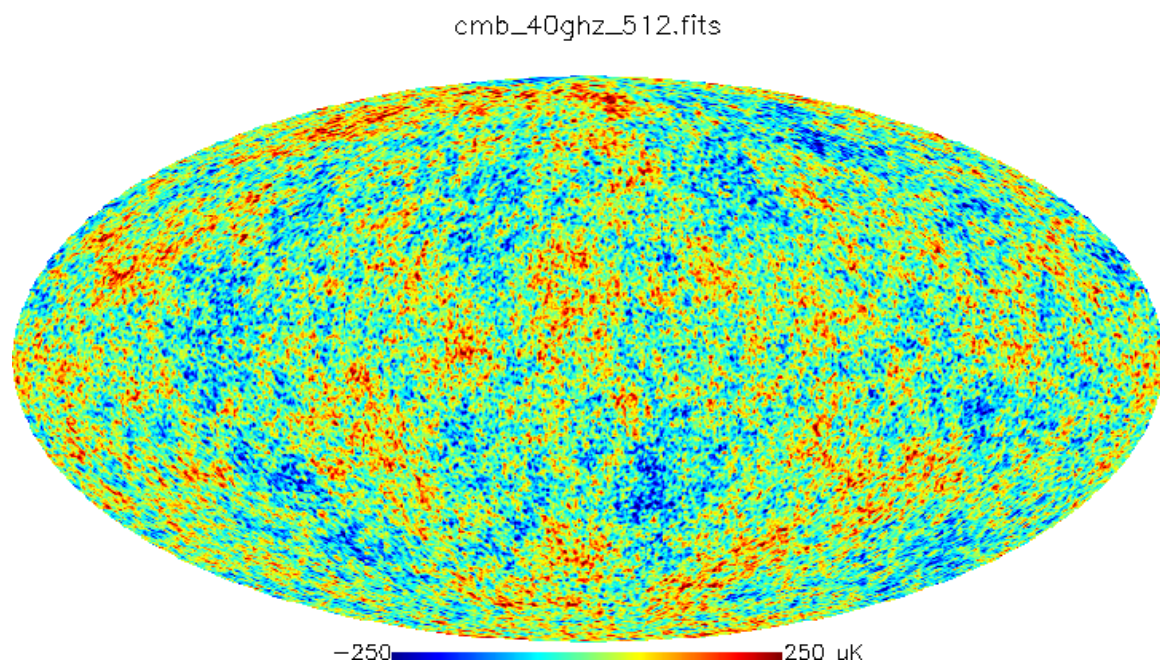


Figure 7.2: Simulated CMB component for MAP 40 GHz channel with 28' FWHM.

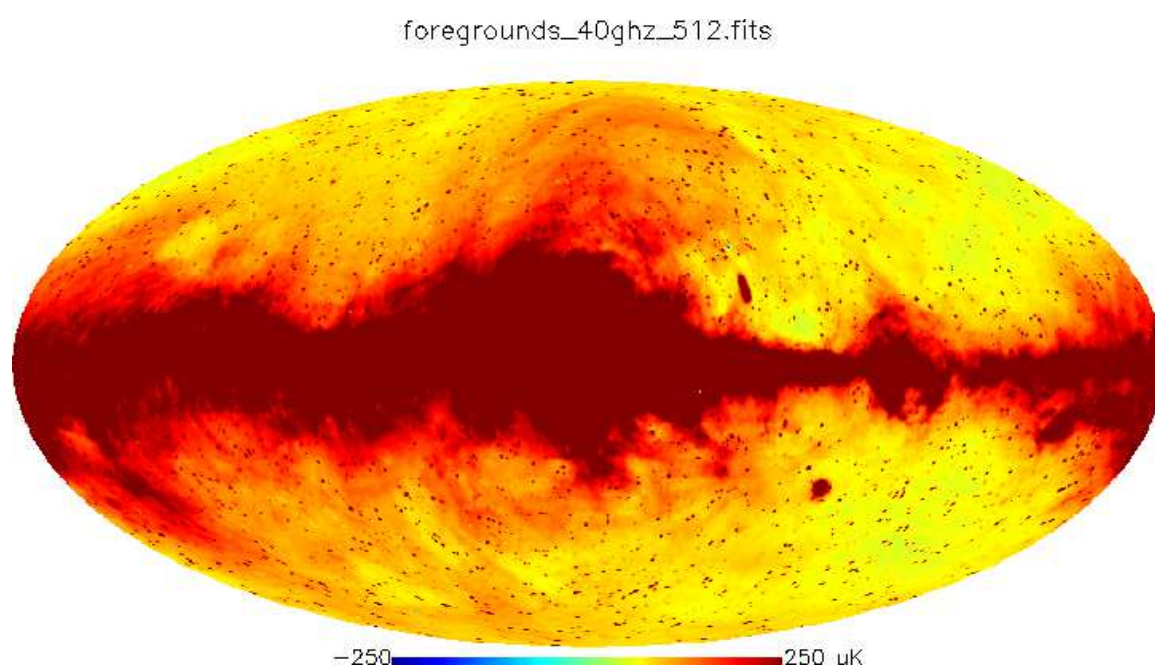


Figure 7.3: Simulated Galactic and extragalactic foregrounds for MAP 40 GHz channel with 28' FWHM.

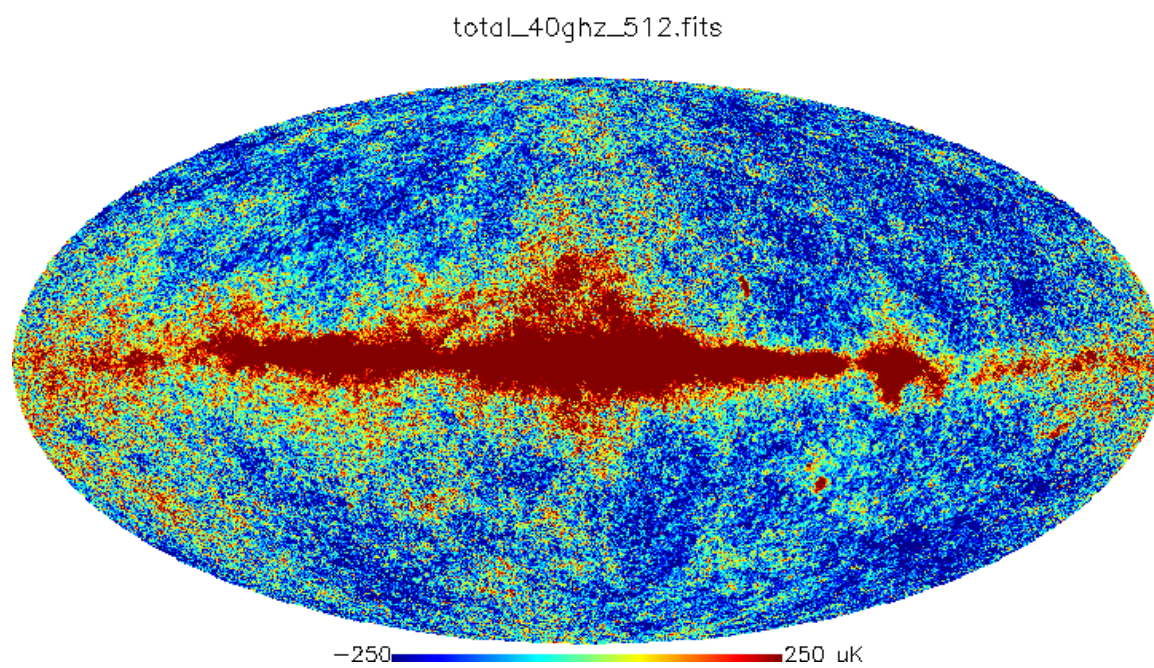


Figure 7.4: A realistic simulation of the microwave sky for MAP 40 GHz channel with 28' FWHM.

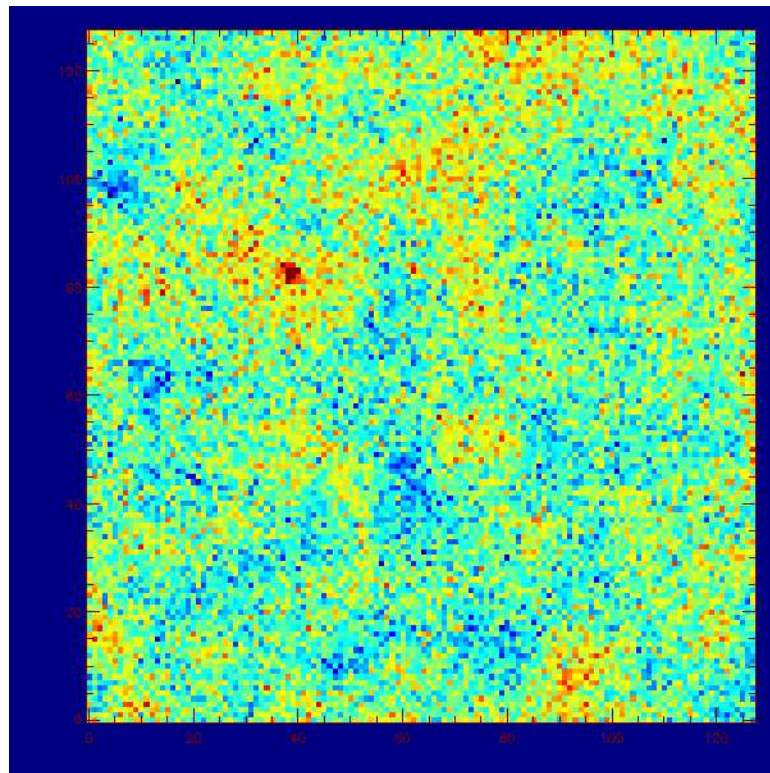


Figure 7.5: WOMBAT Challenge simulation of a MAXIMA dataset at 150 GHz, $11'$ FWHM, $10^\circ \times 10^\circ$.

Chapter 8

Low-redshift Infrared Galaxies

8.1 Motivation

The COBE detection of large-angular scale anisotropy in the Cosmic Microwave Background radiation (Smoot et al. 1992) has sparked a drive to measure the anisotropy on smaller angular scales with the goal of determining crucial information about the density and expansion rate of the universe, the nature of dark matter, and the spectrum of primordial density perturbations. Current anisotropy observations look at sub-degree angular scales which correspond to observable structures in the present universe. Improved instrumentation and the MAP (Microwave Anisotropy Probe) and Max Planck Surveyor (formerly COBRAS/SAMBA) satellite missions focus attention on angular scales between one-half and one-sixth of a degree.

Due to its large beam size, COBE was basically unaffected by extragalactic foreground sources (Banday et al. 1996; Kogut et al. 1994). Because the antenna temperature contribution of a point source increases with the inverse of the solid angle of the beam, observations at higher angular resolution are more sensitive to extragalactic foregrounds, including the low-redshift infrared-bright galaxies examined here. At frequencies above 200 GHz, these infrared galaxies are the dominant extragalactic foreground. Predictions and simulations for high-redshift infrared galaxies were presented in Section 7.4 and limits on their anisotropy will be discussed in Chapter 10.

Previous work in this area (Toffolatti et al. 1995; Franceschini et al. 1989; Wang 1991) used galactic evolution models with specific assumptions about dust temperatures to predict the level of extragalactic foreground. We choose instead a phenomenological

approach using the infrared-bright galaxies detected by the Infrared Astronomical Satellite (IRAS) and the Galactic emission detected by the COBE (Cosmic Background Explorer) satellite. Section 8.3 compares our results with those from galaxy-evolution models.

The FIRAS (Far-Infrared Absolute Spectrophotometer) instrument of COBE gives evidence for the existence of Cold ($< 15\text{K}$) Dust in the Galactic plane (Reach et al. 1995). If the Milky Way has Cold Dust, then it is likely present in other dusty spirals, which comprise the majority of bright low-redshift infrared sources. Some observations (Chini et al. 1995; Block et al. 1994; Devereux & Young 1992) indicate the presence of Cold Dust in other galaxies. Neither galactic evolution models nor pre-FIRAS observations (see Eales et al. 1989) were able to set tight constraints on emission from Cold Dust, but the FIRAS observations do. Emission from dust close in temperature to the 2.73 K background radiation is difficult to separate from real CMB anisotropies. If Cold Dust in spiral galaxies is typically accompanied by the Warm Dust to which IRAS is sensitive, we can use the FIRAS information about the total dust emission spectrum of the Galaxy to overcome this spectral similarity and learn about the amount of Cold Dust in a galaxy by measuring its amount of Warm Dust.

8.2 Extragalactic Infrared Sources

The far-infrared discrete sources detected by IRAS are typically inactive spiral galaxies, although some are quasars, starburst galaxies, and Seyfert galaxies. The IRAS 1.2 Jy catalog (Fisher et al. 1995) provides flux measurements of 5319 galaxies at 12, 25, 60, and 100 μm , where interstellar dust emission is dominant. We compared the locations of these galaxies with those of a thousand of the brightest radio sources, and only 7 possible coincidences resulted. This lack of coincidence shows that radio-loud galaxies can be treated separately (see Chapter 9). The IRAS sources are roughly isotropic in distribution, except for a clear pattern of the Supergalactic Plane. To reduce the possibility of residual galactic contamination, we restrict our analysis to galactic latitude $|b| > 30^\circ$, which includes contributions from 2979 galaxies for a 0.5 beam.¹

The nature of dust in spiral galaxies is still an open question. It seems likely that there is dust at widely varying temperatures and possibly with different emissivities

¹The dependence on beamsize is mild, but for a larger beam more sources centered outside of this area are convolved into it.

(Rowan-Robinson 1992; Franceschini & Andreani 1995). Attempts to fit observational data have yielded a variety of results; it is unclear if far-infrared luminous dust is well described by a one-component or a two-component model, and the emissivity power-law index is only known to be between 1 and 2. We avoid specifying the nature of this dust by using the observed Galactic far-infrared emission spectrum as a template for IRAS galaxies. To check the accuracy of this template, we fit a two-component dust model to IRAS galaxies and to the integrated 12, 25, 60, and 100 μm fluxes of the Milky Way measured by the DIRBE (Diffuse Infrared Background Experiment) instrument of COBE. This produces similar results for the Warm (15-40 K) Dust component to which IRAS and DIRBE are most sensitive; for an emissivity power-law index of 1.5, DIRBE gives a Warm Dust temperature of 28K for the Milky Way, while the 425 IRAS galaxies with highest-quality flux measurements are collectively fit to a Warm Dust temperature of 33K. This Warm Dust accounts for the majority of the far-infrared emission of spiral galaxies.

There is, however, observational evidence that the far-infrared emission of inactive spirals is dominated by dust slightly colder than 20K (Neininger & Guelin 1996; Chini & Kruegel 1993). Fitting the FIRAS spectrum of the Milky Way also leads to a Warm Dust temperature close to 20K. These fits appear to conflict with the temperatures found above using IRAS and DIRBE fluxes at $\lambda \leq 100\mu\text{m}$. Using 60, 100, 140, and 240 μm DIRBE fluxes, however, indicates a Warm Dust temperature for the Galaxy of 24K. This shows that temperature fits to data on one side of the peak of a graybody (modified blackbody) spectrum can be inaccurate. Figure 8.1 shows that the spectra of the Milky Way found by DIRBE and FIRAS are indeed compatible. It may be an oversimplification to represent the Warm Dust in a galaxy by a single temperature.

We recognize that not all IRAS galaxies have the same far-IR spectrum as the Milky Way. Active galaxies are warmer, with an average Warm Dust temperature of 33K (for emissivity index 2, Chini et al. 1995). However, the cirrus emission which dominates Galactic dust is consistent with the emission from the majority of inactive spirals (Andreani & Franceschini 1996; Pearson & Rowan-Robinson 1996). Some observations indicate that our Galaxy is slightly warmer than the average inactive spiral (Chini et al. 1995). None of these observations includes enough frequencies to provide a template microwave emission spectrum, and their results range by a factor of 3 depending on the choice of beam corrections (Franceschini & Andreani 1995). The Milky Way is a good middle-of-the-road choice for a microwave template spectrum; the DIRBE and IRAS dust temperature fits

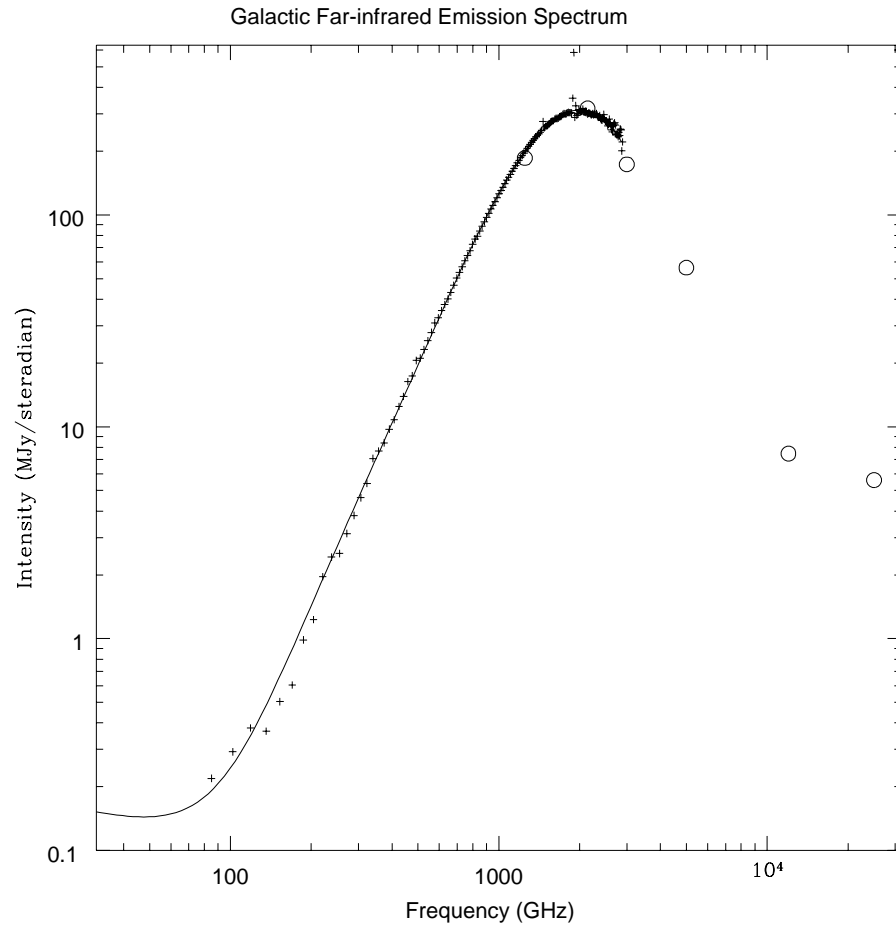


Figure 8.1: Galactic Far-IR Emission Spectrum

The FIRAS Galactic Dust spectrum, including emission lines, is shown by + symbols. The smooth curve is a fit to this spectrum based upon a two-component dust model with synchrotron and free-free emission included using DMR results. The FIRAS error bars are not shown because they are extremely small on this scale. The open circles are DIRBE integrated Galactic fluxes at 12, 25, 60, 100, 140, and 240 μm , normalized to the FIRAS measurements.

given above agree rather well. For extrapolation to microwave frequencies, uncertainty in emissivity is of much greater importance than this level of temperature uncertainty, anyway.

After removing Galactic emission lines (as in Reach et al. 1995), we fit a two-component dust model to the FIRAS dust spectrum. The CO 1-0 emission line at 115 GHz is not clearly detected by FIRAS but could be responsible for increased emission at that frequency. With a ν^2 emissivity law assumed, the best fit is Warm Dust at 19.4K and Cold Dust at 4.3K with an optical depth 12.1 times that of the Warm Dust. It is possible to vary the parameters of the dust model significantly and still have an acceptable fit, so we refrain from assigning any physical importance to the parameters of the fit. We add synchrotron and free-free components with microwave-range spectral indices of -1.0 and -0.15 , respectively, so that these sources of microwave emission match COBE DMR (Differential Microwave Radiometer) observations below 100 GHz (Kogut et al. 1996b; Reach et al. 1995; Bennett et al. 1992). Free-free emission is stronger than dust beyond the low-frequency end of the FIRAS spectrum.

We combine data from DIRBE, FIRAS, and DMR to form the broad Galactic spectrum shown in Figure 8.1. Each IRAS 1.2 Jy source is fit to the DIRBE end of the spectrum and extrapolated to the desired frequency using this template. In fitting each IRAS galaxy to the DIRBE fluxes of the Milky Way, we give more weight to the 60 and 100 μm fluxes, which are most sensitive to Warm Dust, than to the 12 and 25 μm fluxes, which are also sensitive to Hot (100-300 K) Dust. The 1.2 Jy catalog gives redshifts for these galaxies. Most have $z < 0.05$ and all have $z < 0.3$. We take these redshifts into account while fitting and extrapolating.

It would be advantageous to fit each type of galaxy to a specialized far-IR to microwave spectrum, but no other trustworthy template spectrum is currently available, so we use the Galactic far-infrared emission spectrum for all sources. The Galactic spectrum agrees well with observed correlations between radio and IR fluxes of IRAS galaxies (Condon & Broderick 1991; Crawford et al. 1996). Our template spectrum is consistent with detections and upper limits for bright infrared galaxies from DIRBE (Odenwald et al. 1998). This is helpful because DIRBE used 140 and 240 μm channels, which IRAS lacks, allowing it to probe much cooler dust temperatures than IRAS. DIRBE rules out the possibility of extremely bright sources occurring in the 2% of the high Galactic latitude sky not surveyed by IRAS and sees no evidence for sources whose emission comes predominantly from Cold Dust.

8.3 Results

We use the Galactic far-infrared emission spectrum to predict the microwave flux of each IRAS galaxy in Jy (1 Jy = $10^{-26} \text{W/m}^2/\text{Hz}$). To convert from flux S to antenna temperature T_A , we use

$$T_A = S \frac{\lambda^2}{2k_B \Omega} , \quad (8.1)$$

where k_B is Boltzmann's constant, λ is the wavelength, and Ω is the effective beam size of the observing instrument. Antenna temperature is related to thermodynamic temperature by

$$T_A = \frac{x}{e^x - 1} T, \quad (8.2)$$

defining $x \equiv h\nu/kT$. Small fluctuations in antenna temperature can be converted to effective thermodynamic temperature fluctuations using

$$\frac{dT_A}{dT} = \frac{x^2 e^x}{(e^x - 1)^2} . \quad (8.3)$$

Analysis of source counts indicates that the 1.2 Jy sample is complete down to an extrapolated flux of 3 mJy at 100 GHz. We divide the sources logarithmically into groups of similar flux and find a gradual decrease in anisotropy as flux decreases, indicating that dimmer sources will not generate significant anisotropy. This may not hold true for high-redshift infrared galaxies, however, as the k-correction makes sources which are dim at $100\mu\text{m}$ quite bright in the sub-millimeter. Toffolatti et al. (1995) found a negligible contribution from non-Poissonian fluctuations. Poissonian fluctuations should be dominated by those sources prevalent enough to have roughly one source per pixel. If all sources have roughly the luminosity of the Milky Way, then for an instrument with a resolution of $10'$ to have one source per beam, we must look at sources with $z \simeq 0.24$. Assuming $(1+z)^3$ luminosity evolution and including k-correction (see Pearson & Rowan-Robinson 1996; Beichman & Helou 1991), these sources will generate a temperature anisotropy only 2% of that caused by IRAS 1.2 Jy galaxies. We therefore expect the anisotropy generated by low-redshift sources too dim to make the 1.2 Jy catalog to be a small part of the total anisotropy; the brightest sources are generating most of the fluctuations.

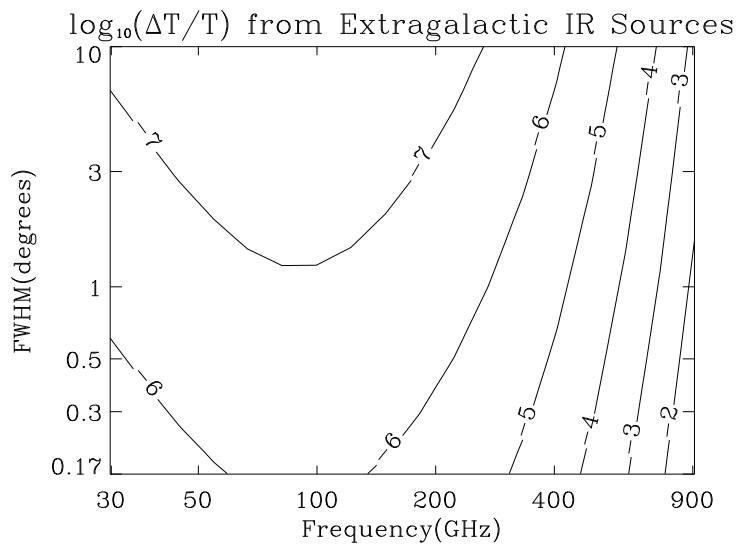


Figure 8.2: Microwave anisotropy from low-redshift infrared galaxies.

A log-log-log contour plot of equivalent thermodynamic temperature fluctuations due to extragalactic infrared sources as a function of frequency in GHz and angular resolution (FWHM) in degrees. The temperature anisotropy shown is $\log_{10} \frac{\Delta T}{T}$ where ΔT is the root mean square equivalent thermodynamic temperature generated by extragalactic infrared sources in Kelvin and T is the temperature (2.73K) of the CMB. The increase in anisotropy at low frequencies occurs because synchrotron and free-free emission are included in our template spectrum.

To simulate observations, we convolved all sources on pixelized skymaps (2X over-sampled) of resolution varying from $10'$ to 10° . The resulting maps, covering a range of frequencies from 30 to 900 GHz, were analyzed to determine the expected contribution of IRAS galaxies to foreground confusion of CMB temperature anisotropy. The information contained in these skymaps can be used to choose regions of the sky in which to observe (Smoot 1995). The contour plot in Figure 8.2 shows the rms thermodynamic temperature anisotropy produced by extragalactic infrared sources over the full range of frequencies and instrument resolution. The minimum value of $\frac{\Delta T}{T}$ is 1.3×10^{-8} at large FWHM and medium frequency and the maximum value is 0.092 at small FWHM and high frequency. For frequency in GHz and FWHM in degrees, our results for temperature anisotropy are fit to within 10% by

$$\log_{10} \frac{\Delta T}{T} = 2.0(\log_{10} \nu)^3 - 8.6(\log_{10} \nu)^2 + 10.3 \log_{10} \nu - 0.98 \log_{10}(FWHM) - 9.2. \quad (8.4)$$

The inverse linear relationship between anisotropy and FWHM results from the combined effects of beam convolving and map pixelization (see Chapter 10 for a derivation). Anisotropy from extragalactic infrared sources dominates expected CMB anisotropy at frequencies above 500 GHz. This makes effective foreground discrimination possible for instruments with a frequency range sufficiently wide to detect the extragalactic infrared foreground directly.

Figure 8.3 shows a summary of our results for several benchmark instrument resolutions. The dashed lines represent the results of subtracting pixels where the fluctuations from extragalactic infrared sources are five times greater than the quadrature sum of the rms CMB anisotropy and the expected instrument noise for the Planck Surveyor at that frequency. These 5σ pixels can be assumed to contain bright point sources. Our results agree closely with those of Toffolatti et al. (1998) for their model of moderate cosmological evolution of all galaxies. Our predictions for anisotropy are about a factor of three lower than those of Franceschini et al. (1989), who assume strong evolution of the brightest IR sources and include early galaxies with heavy starburst activity. Wang (1991) ignores the possibility of cold dust and uses galaxy evolution models to predict anisotropy levels somewhat lower than those found with our phenomenological approach.

The 5σ subtraction has a significant effect for small FWHM at frequencies below 500 GHz. The maximum effect is to subtract 0.002% of the pixels, leading to a factor of 5 reduction in foreground temperature anisotropy. This is further evidence that temperature

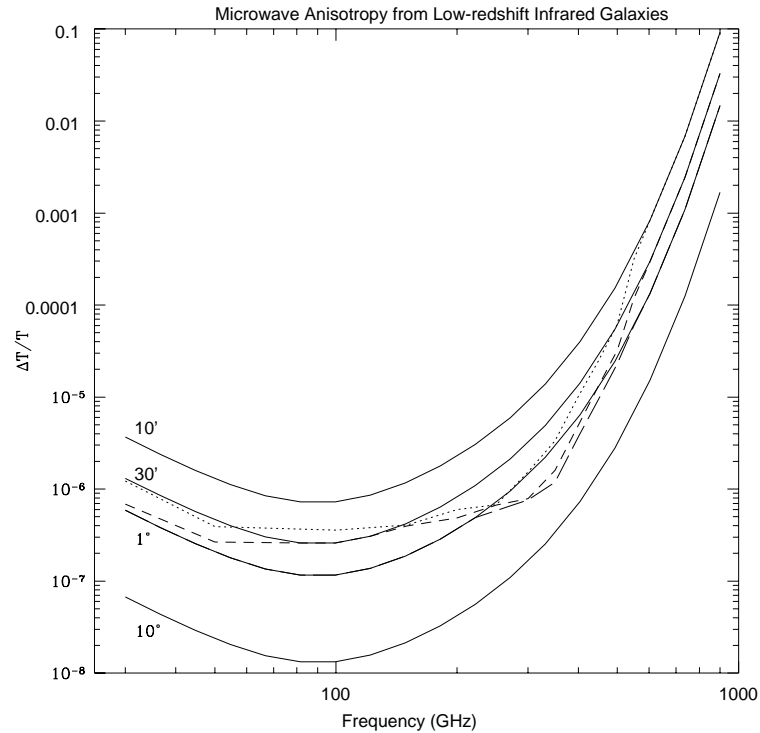


Figure 8.3: Confusion from low-redshift infrared galaxies

Log-log plot of $\frac{\Delta T}{T}$ versus frequency for instrument resolutions of $10'$, $30'$, 1° , and 10° , showing window where foreground confusion should be less than 10^{-6} . Solid lines are for no pixel subtraction. The dotted, dashed, and long-dashed lines show the results with pixels at a level of 5σ removed for resolutions of $10'$, $30'$, and 1° , respectively. This 5σ subtraction makes no difference at any frequency for 10° .

anisotropy from extragalactic infrared sources is dominated by the brightest sources. The bright sources are a mixture of Local Group galaxies and more distant infrared-luminous galaxies such as starburst galaxies. Optimal subtraction of the extragalactic infrared foreground requires the contribution from each bright source to be predicted accurately.

Figure 8.4 shows a skymap of our extrapolated IRAS 1.2 Jy catalog at 100 GHz. Very few of these sources are significant at frequencies below 200 GHz, although the entire 5319 sources should be detected by Planck HFI due to its high resolution at high frequencies. The skymap shows the structure of the Supergalactic Plane, as well as the regions of the sky not included due to Galactic contamination or the IRAS satellite's failure to observe them. Several sources are considerably brighter than the maximum of the color table, which has been set very low to show all of the catalog, even though most sources are quite dim at 100 GHz.

8.4 Discussion

Our usage of the Galactic far-infrared emission spectrum as a template causes systematic errors on a galaxy-by-galaxy basis. Our method can be improved in the future to account for the spectral difference between Ultraluminous Infrared Galaxies and normal spirals. It is easy to place constraints on our results; if all galaxies had only 33K dust as is typical for active galaxies, the resulting anisotropy would be a factor of 100 lower. This is highly unlikely, because we know that most IRAS galaxies are inactive spirals, and galaxies with colder dust will dominate the anisotropy at mm-wavelengths because of the selection effect favoring sources with flatter spectra. A robust upper limit on microwave anisotropy from infrared galaxies can be set by assuming that these IRAS 1.2 Jy galaxies cause the full cosmological far-infrared background (Puget et al. 1996; Burigana & Popa 1998; Fixsen et al. 1998; Schlegel et al. 1998; Hauser et al. 1998). In this case we have underestimated the anisotropy by a factor of 100, but no predictions of the IR background expect these nearby galaxies to produce more than a few percent of it. A more realistic check on our results comes from Andreani & Franceschini (1995), who measured a complete sample of IRAS galaxies at $1300 \mu\text{m}$ (240 GHz). Their average flux ratio of $1300 \mu\text{m}$ over $100 \mu\text{m}$ is half that of the Galaxy, but one of their beam correction methods brings their ratio into agreement with the Milky Way. They find that the $60 \mu\text{m}$ emission of spiral galaxies receives enough contribution from a starburst dust component mostly absent in the

Galaxy that including $60 \mu\text{m}$ fluxes in our fits may have caused a factor of 2 overestimate. Combined, these corrections give us a possible systematic overestimate of anisotropy by a factor of 4. If typical IR-bright galaxies have dust colder than the Milky Way, our results could instead be an underestimate by a factor of a few, but this appears less likely.

We estimate an overall systematic uncertainty of a factor of 2 at 300 GHz, increasing to a factor of 3 at 100 GHz and to a factor of 5 at 30 GHz. As it is hard to predict the typical dust temperature and emissivity in a given galaxy as well as its relative amount of free-free and synchrotron emission, we estimate that our predictions for the microwave spectrum of each source have an overall factor of 5 uncertainty and an independent factor of 1.3 uncertainty at each frequency. The factor of 5 uncertainty preserves a source's spectral shape whereas the factor of 1.3 uncertainties allow for errors in the predicted spectral shape. These uncertainties are quite large, but the extrapolation we have performed is over a factor of 10-100 in frequency. We expect that forthcoming microwave observations will give us better information, especially about the brightest IRAS 1.2 Jy sources.

The recently obtained spectral knowledge of our Galaxy has enabled us to take into account the possible presence of Cold Dust. Our predicted level of temperature anisotropy makes the extragalactic foreground from low-redshift infrared galaxies dominant over the Galactic foregrounds of dust, free-free, and synchrotron for angular resolutions near $10'$ and frequencies above 100 GHz. Below 150 GHz, radio sources are expected to be the dominant extragalactic foreground. The extragalactic low-redshift infrared foreground will not be significant in comparison to CMB anisotropies around 100 GHz but will be dominant above 500 GHz. Despite the possible presence of Cold Dust in infrared-bright galaxies, our results leave a window at intermediate frequencies for the measurement of CMB anisotropies without significant confusion from extragalactic infrared sources.

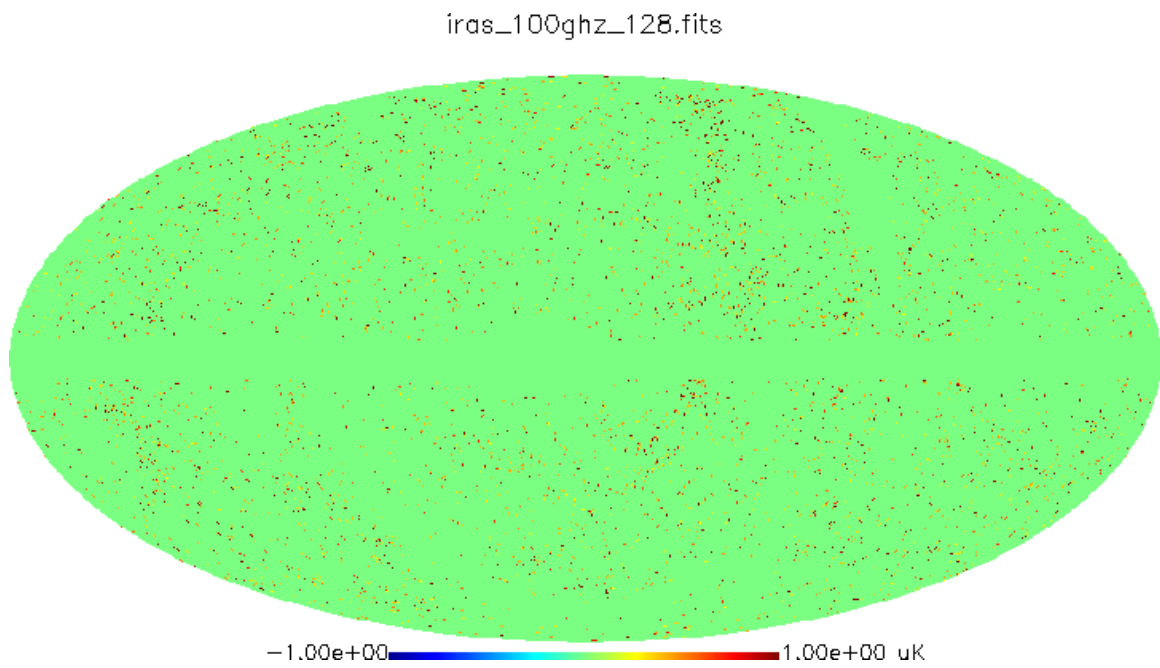


Figure 8.4: Skymap at 100 GHz of predicted contribution from IRAS 1.2 Jy sources.

Chapter 9

Radio Galaxies

9.1 Motivation

High resolution CMB anisotropy observations are sensitive to extragalactic foregrounds, including the radio galaxies considered here, bright infrared galaxies (see Chapter 8), high-redshift infrared galaxies (see Chapter 10), and the Sunyaev-Zeldovich effect from galaxy clusters (see Chapter 11) . Estimates of extragalactic foreground confusion are critical as many ground-based, balloon-borne, and satellite experiments (MAP, Planck Surveyor) plan to study CMB anisotropies at angular scales from $5'$ to $30'$, and preliminary anisotropy results are already available (see Section 2.1).

To evaluate the impact of known radio sources on CMB anisotropy observations, we use flux data from a variety of catalogs (see Section 9.2), including recent measurements, to construct models of source spectra as a function of frequency. We analyze simulated skymaps at frequencies from 10 to 300 GHz to determine the expected contribution of radio galaxies to foreground confusion of CMB temperature anisotropy. This information will be useful when choosing frequencies and regions of the sky to observe CMB fluctuations on small angular scales. This work represents a significant improvement over previous efforts (Toffolatti et al. 1998; Toffolatti et al. 1995; Franceschini et al. 1989) which depended upon galactic evolution models to predict the contribution of simulated radio sources at microwave frequencies. Our catalog contains detailed observations of known sources and hence can be used to make a spatial template for masking out their emission, and we believe that this phenomenological approach will lead to greater accuracy in predicting source counts and the overall level of foreground anisotropy.

9.2 Our Catalog

The discrete radio sources used in this project were compiled from a large number of separate samples. Our current catalog includes flux measurements and their corresponding errors at multiple frequencies for 2207 sources. We have focused our attention on obtaining all available radio observations at millimeter and sub-millimeter wavelengths, resulting in 5766 observations of 758 different sources at 90 GHz, 890 observations of 229 different sources from 100-200 GHz, and 2628 observations of 309 different sources at frequencies above 200 GHz. The sources are roughly isotropic in distribution, except for a significantly greater number of sources in the northern celestial hemisphere due to the anisotropic distribution of radio telescopes on Earth with high-frequency capability. In addition, there are noticeably fewer observations within 10° of the galactic plane and the celestial north pole due to the difficulty of observing extragalactic radio sources in those locations.

Our catalog includes the full-sky 5 GHz-selected 1 Jy sample of Kühr et al. (1981). We add high-frequency (> 90 GHz) measurements (Steppe et al. 1988, 1992, 1995; Tornikoski et al. 1996; Kreysa 1998; Antonucci et al. 1990; Beichman et al. 1981; Chini et al. 1989; Edelson 1987; Gear et al. 1994; Holdaway et al. 1994; Knapp & Patten 1991; Landau et al. 1980, 1983, 1986; Lawrence et al. 1991; Nartallo et al. 1998; Owen et al. 1978, 1980; Stevens et al. 1996; Chandler 1995; VLA 1995) and centimeter-wavelength observations (Herbig & Readhead 1992; Patnaik et al. 1992; Wiren et al. 1992; Stanghellini et al. 1997; Perley 1982; Aller et al. 1985; VLA 1997) . An updated version of the catalog will be described in detail by Gawiser et al. (1999, hereafter GSS) .

9.3 Spectral Fitting

Some extragalactic radio sources have complex spectra which cannot be approximated by simple functional forms due to emission from both compact and extended structures which dominate at different frequencies. In most radio galaxies, the emission comes from radio lobes located symmetrically around the core. The dominant emission mechanism, synchrotron, can be well approximated by a simple power law,

$$S \propto \nu^{-\alpha} \tag{9.1}$$

with a flux spectral index, α , typically between 0.5 and 1.0 (Platania et al. 1998) . Some radio sources have compact active nuclei which generate flat-spectrum radio emission. The

spectra of these sources can be inverted ($\alpha > 0$) for most of the radio frequency range due to self-absorption of the lower frequency emission. Attempts to explain the observational data have yielded a variety of results. The central engine of a typical active galaxy may consist of a supermassive black hole surrounded by an accretion disk and accelerating a jet of relativistic particles perpendicular to the disk plane (e.g. Urry & Padovani 1995). Boettcher et al. (1997) proposed a model in which the inverted spectrum of NGC 3031 is assumed to be the emission of a jet component, becoming optically thin to the radio emission of a monoenergetic pair plasma at decreasing frequencies as it moves outward and expands.

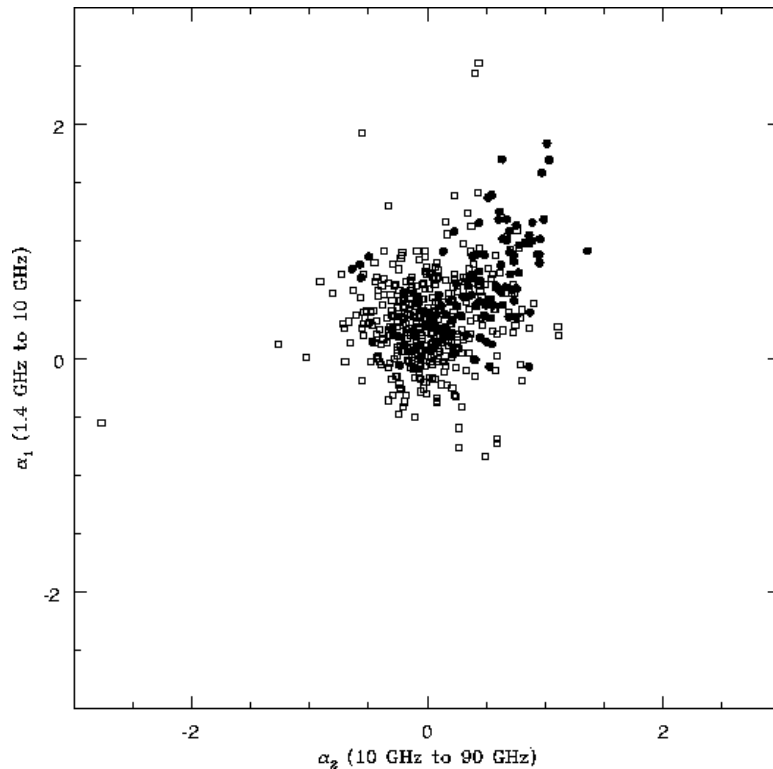


Figure 9.1: Spectral indices α_1 from 1.4 to 10 GHz and α_2 from 10 to 90 GHz. Solid circles represent the brightest sources at 1.4 GHz; open squares represent dimmer sources at 1.4 GHz. Note the lack of clustering into distinct archetypal spectra.

For sources which lack direct high-frequency observations, we avoid trying to determine the nature of the emission mechanism. Instead, we use a phenomenological approach based on the expectation that the spectra of most radio sources approach power law behavior at frequencies higher than $\simeq 5$ GHz (Verschuur & Kellerman 1988). This power law

may then be used to extrapolate the spectrum to typical CMB observation frequencies. To determine if template spectra could be used we use sources that have been measured near 1.4, 10, and 90 GHz and plot each source’s spectral index from 1.4 GHz to 10 GHz versus its index from 10 GHz to 90 GHz in Figure 9.1. There is a vague clustering of bright sources (circles) consistent with the notion that the brightest sources selected at low frequencies tend to have steep spectra. The overall scatter of source spectra in Figure 9.1 shows that it is wrong to categorize radio sources into template spectra or a narrow spectral index range. This motivates us to fit the spectra of each source individually. A previous phenomenological approach (Tegmark & Efstathiou 1996) extrapolated 1.4 GHz source counts by assuming flat-spectrum emission for all sources. Our method has the advantages of using the actual source locations, which can be turned into a template for masking the brightest pixels on the sky, and of choosing the spectrum for extrapolation on a case-by-case basis.

To determine the frequency beyond which a power law (a line on a log-log plot) can be fitted to the spectrum of a given source, we use an iterative model which starts with the best-fit line to the three highest frequency data points and repeatedly includes the next highest frequency data point to the set to which it fits a line. The fitting stops when the reduced χ^2 starts to get worse or becomes acceptable ($\simeq 1$). There is little evidence that inverted spectra are common past 30 GHz (Steppe et al. 1995; Stanghellini et al. 1997), so we set the handful of inverted ($\alpha \leq 0$) high-frequency spectra in the catalog to flat ($\alpha = 0$) spectra. Upon closer inspection, these inverted spectra appear to result from variable sources being observed at different epochs at different frequencies, and we find that most of the sources with $\alpha_2 \leq 0$ in Figure 9.1 based on their mean 10 and 90 GHz fluxes are better fit by an $\alpha \geq 0$ power-law when all observations are taken into account. The average high-frequency spectral index was 0.5 with 27% of the sources in our catalog having steep spectra ($\alpha > 0.75$), and 37% having flat spectra ($\alpha < 0.25$).

To check the accuracy of this technique, we ran our extrapolation method on sources with observations at 90, 150, and/or 230 GHz while ignoring the observations above certain frequencies and then compared the measured fluxes with the extrapolated fluxes. The results (Table 9.3) show that the extrapolation method works best when there is at least one measurement at 20 GHz or greater, as expected since many spectra become power-law past 5 GHz. Table 9.3 shows that on average we overpredict the flux at 90 GHz by a factor of 1.6, even when measurements above 20 GHz are used. However, the median such error factor is only a factor of 1.1 overestimate, so we have roughly an equal number of

Table 9.1: Average Errors from Extrapolation. The average extrapolation error is the mean of $|(S_P - S_O)/S_P|$ where S_P is the predicted flux and S_O is the observation. The average error factor is the mean of S_P/S_0 .

ν tested	ν ignored	Avg. Extrapolation Error	Avg. Error Factor
90 GHz	≥ 2 GHz	209 %	2.5
90	≥ 10	148	2.3
90	≥ 20	133	2.0
90	≥ 90	92	1.6
150	≥ 90	94	1.5
230	≥ 90	250	3.2

over- and under-estimates. This is no longer the case at 230 GHz, where even the median error factor is 1.9; our extrapolation method is overestimating the typical flux due to flat spectra falling off to more typical synchrotron spectra at frequencies around 100 GHz (Gear et al. 1994) . It is difficult to predict how far this fall-off will last, as thermal emission from low levels of dust in these radio-bright galaxies are expected to dominate their spectra by 500 GHz, except for the BL Lacs which have flat spectra up to infrared wavelengths (Knapp & Patten 1991; Chini et al. 1989; Landau et al. 1986) . We therefore only trust our extrapolation in the range that has been tested, up to a maximum frequency of 300 GHz. As the radio sources that have been observed at 30-300 GHz were selected at lower frequencies for brightness and flat spectra, our errors are only good estimates for this type of radio sources. This selection effect is not a great concern, however, as those are exactly the type of radio sources that threaten CMB anisotropy observations. When interpolation is required, we use a cubic spline which passes through the mean fluxes at the observed frequencies. We visually inspected all 2207 sources to check the algorithm and eliminate any serious errors or outliers.

For planned CMB anisotropy experiments, an additional concern is that the flat-spectrum radio sources can vary by up to a factor of ten in flux since their emission comes from a compact, active core. Typical variations occur on timescales of one month to one year. Outbursts are seen first at the highest (most transparent) frequencies and gradually shift to lower frequency, but except for this effect the overall spectrum shape is often preserved for a decade or longer (Tornikoski et al. 1993). We use the scatter in the observed fluxes of a source at each frequency to estimate the typical range of variability, which yields an error bar on the source's flux at that frequency about the mean of all observations. Because the

variations are not periodic, there is little more that can be done, unless sources are observed nearly simultaneously at higher resolution and nearby frequencies. GSS looks at the issue of variability in detail, including the possibility of extrapolating long-term drifts in source flux to the next epoch of observation. Radio sources are typically 4-7% polarized, and this polarization is variable (Nartallo et al. 1998), so radio-source foreground subtraction will be an important consideration for CMB polarization observations as well.

9.4 Results

We use the fitted spectra to predict the microwave flux of each radio galaxy. Equations 8.1 and 8.3 give the conversion from flux to antenna temperature to thermodynamic temperature fluctuations. The intrinsic $\Delta T/T$ of the CMB found by COBE is $\simeq 10^{-5}$ and is expected to vary between that and 3×10^{-5} due to the acoustic oscillations discussed in Chapter 1 at the angular resolutions considered here.

An analysis of source counts shows no indication of incompleteness for the northern celestial hemisphere subset of our catalog down to an extrapolated flux of 1.0 Jy at 90 GHz while the southern hemisphere is incomplete below 2.0 Jy at 90 GHz. For the purposes of statistical analysis we have concentrated on the northern hemisphere where we appear to have measurements of the 200 brightest sources in the hemisphere. We cannot rule out the existence of an unrelated population of sources peaking around 90 GHz which are not bright at lower frequencies, as 90 GHz observations have only been made for sources selected at frequencies below 10 GHz (this hypothetical source population is limited in Chapter 10). The brightest sources will dominate the anisotropy unless they are masked, because uncertainty in their exact fluxes makes subtraction highly inaccurate. After masking, the brightest remaining sources will dominate unless non-Poissonian clustering becomes appreciable. Toffolatti et al. (1998) have shown that non-Poissonian clustering is not expected to make an important contribution to the foreground anisotropy from radio sources.

To simulate observations, we convolve all sources on pixelized sky maps (twice oversampled) of resolution varying from $10'$ to 10° at frequencies between 10 and 300 GHz. To avoid underestimating the anisotropy and to reduce the possibility of residual galactic contamination, we use only the portion of each skymap which covers galactic latitudes $|b| > 30^\circ$ and corresponds to the northern celestial hemisphere to produce estimates of $\Delta T/T$.

Figure 9.2 shows a summary of our results for several relevant instrument resolutions. The inverse relationship between anisotropy and FWHM arises due to the combined effects of beam convolving and pixelization. The exact level of oversampling causes a small change in the measured anisotropy, but the $1/\text{FWHM}$ behavior should hold for extrapolation to smaller resolutions (see Chapter 10).

We also analyze $\frac{\Delta T}{T}$ in the northern hemisphere based on only the 758 sources with 90 GHz measurements. The resulting rms $\frac{\Delta T}{T}$ at 90 GHz with a FWHM of $30'$ is 2×10^{-6} which dominates the anisotropy since the rms $\frac{\Delta T}{T}$ from extrapolating the spectra of the other 1449 sources amounts to only 7×10^{-7} . This indicates that we have flux measurements for the vast majority of bright 90 GHz radio sources, and there is typically less uncertainty in predicting the fluxes of sources which have already been observed at 90 GHz than in extrapolation. Refregier et al. (1998) find that the 5σ source detection limit for 0.3 MAP pixels will be 2 Jy at 90 GHz. We have 108 sources in our catalog which have been observed to be brighter than 2 Jy at 90 GHz at least once, but only 42 sources have a weighted average flux that high, and a total of 52 sources are predicted to be brighter than 2 Jy at 90 GHz. We estimate that there will be 40-50 radio sources on the sky brighter than 2 Jy at 90 GHz. At the 0.4 Jy level, Toffolatti et al. (1998) predict roughly twice as many sources as we do, but our prediction falls within their range of uncertainty. As the source counts we predict at this level based on the northern celestial hemisphere should be nearly complete, we recommend a slight recalibration of the galaxy evolution models used by Toffolatti et al. (1998), although a factor of two represents remarkable agreement for such different approaches.

Table 9.4 lists the expected level of anisotropy and the number of detected radio sources in MAP and Planck channels if this type of straightforward 5σ source detection and subtraction is performed. Since the 90 GHz MAP channel will have a resolution close to 0.2 we expect a 5σ source detection limit of 1 Jy at 90 GHz. These detected sources represent a list of the few hundred brightest radio sources in the sky at each frequency. The anisotropy levels are shown in Figure 9.2. The level of source confusion drops if the brightest sources ($\geq 5\sigma$) are subtracted. Table 9.4 shows how the expected level of temperature anisotropy from radio sources varies with cutoff level, where we use our catalog to obtain prior information on which pixels are expected to contain sources at a given flux level and then mask those pixels. While all 5σ pixels can be masked without such prior information if the CMB anisotropies are assumed to follow a Gaussian distribution, it is impossible to

Table 9.2: Foreground Anisotropy in MAP & Planck channels after source removal. Sources which contribute to the anisotropies at the 5σ level or higher are considered detected and are removed by masking the pixels containing them. No attempt has been made to use multi-frequency information or further prior information to detect and remove dimmer sources.

Frequency (GHz)	FWHM	Source detection limit	# detected	$\Delta T/T$
MAP 20	56'	1.4 Jy	186	8×10^{-6}
30	41	1.2	216	4×10^{-6}
40	28	0.9	265	3×10^{-6}
60	21	1.1	168	2×10^{-6}
90	13	1.0	161	1.5×10^{-6}
Planck 30	33	0.9	290	5×10^{-6}
44	23	0.8	285	3×10^{-6}
70	14	0.6	360	2×10^{-6}
100	10	0.6	304	1.3×10^{-6}
143	7	0.6	323	9×10^{-7}
217	5	0.3	533	7×10^{-7}
353	4.5	0.2	644	9×10^{-7}
545	4.5	0.4	289	8×10^{-6}
857	4.5	0.7	125	4×10^{-4}

remove all 1σ pixels without crippling the analysis. The actual improvements from masking all pixels expected to contain 1σ sources may be less than indicated, unfortunately, due to the effect of incompleteness in our catalog. GSS will attempt to fill in this incompleteness using full-sky PMN and GB6 catalogs at 5 GHz. If we settle for making the southern celestial hemisphere as complete as the northern is now, we could create a mask for all sources expected to contribute at the 3σ level, which is enough to make a significant reduction in radio source contamination versus 5σ subtraction alone.

9.5 Improving Sky Coverage with the PMN Survey

In order to have a roughly isotropic distribution of radio sources, we have added the 1770 brightest sources from the Southern sky Parkes-MIT-NRAO catalog (Griffith & Wright 1993; Griffith et al. 1994, 1995; Wright et al. 1994, 1996) which were not already included in the SGS catalog. These sources have fluxes measured at 4.85 GHz, and some have also been observed at 2.7 GHz allowing for a rough measurement of their radio-frequency spectral index.

Figure 9.4 shows a skymap (in Galactic coordinates) of our extrapolated/interpolated

Table 9.3: Foreground Contamination in 13' MAP channel at 90 GHz. This analysis assumes that our catalog is used to identify sources whose fluxes will be above the threshold and that the pixels containing those sources are masked. The results given are for the northern celestial hemisphere, where our catalog is estimated to be complete for the brightest few hundred sources, so the final line is likely an underestimate of anisotropy.

Threshold (Jy)	# Sources above Threshold	$\Delta T/T$
None	0	4.4×10^{-6}
2 (10σ)	49	2.1×10^{-6}
1 (5σ)	161	1.7×10^{-6}
0.6 (3σ)	346	1.2×10^{-6}
0.2 (1σ)	940	3.8×10^{-7}

radio source predictions at 100 GHz. MAP should detect about 200 of these sources at the 5σ level. The map shows the $|b| > 5$ cut we made in the PMN catalog to eliminate Galactic contamination and the dearth of sources at the celestial North pole, where radio source observations are difficult. Figure 9.3 shows confirmation of the expected power-law power spectrum for radio galaxies at 100 GHz.

We estimate an overall systematic uncertainty of a factor of 1.5 for our predictions at frequencies less than 100 GHz, increasing to a factor of 3 at 200 GHz and a factor of 5 at frequencies above 300 GHz. Two major sources of uncertainty affect these predictions at high frequency: the likelihood that the spectral index will fall off around 100 GHz due to a falloff in each galaxy's electron energy spectrum, and the possibility of appreciable thermal emission from dust in each galaxy contributing at frequencies above 100 GHz. We expect an overall error for each source which preserves the source's predicted spectrum of a factor of 1.5 for sources from the SGS catalog. This overall error is a function of the 4.85 GHz flux error and the spectral index uncertainty for sources from the PMN catalog. The uncertainties for each source are based on an estimated spectral index uncertainty of 0.2 for sources with measured 2.7 GHz fluxes and of 0.5 for others. PMN sources with apparently rising spectra were set to flat spectra and assigned a spectral index uncertainty of 0.5 since radio spectra that rise from 2.7 to 5 GHz typically turn over and fall thereafter. For sources from the original catalog, we expect there to be an additional independent uncertainty at each frequency of a factor of 1.3 at frequencies below 150 GHz, a factor of 2 at frequencies between 150 and 300 GHz, and a factor of 3 at frequencies above 300 GHz. For sources from the PMN catalog, this frequency-by-frequency error is a function of the spectral index uncertainty.

9.6 Discussion

Our results indicate that the brightest radio sources will dominate microwave anisotropy for a wide range of resolutions and frequencies. Our skymaps predict the location and flux of the brightest radio sources at each frequency, making it straightforward to develop a template for masking the pixels containing them. This masking should be sufficient to protect high resolution CMB anisotropy observations from unacceptable radio source confusion.

Spectral analysis of bright radio sources indicates that their spectra are complex and cannot in general be categorized into template spectra or single power-laws. The results from our analysis of extrapolation errors suggest that our phenomenological approach of fitting a power law to the high-frequency end of each spectrum is a reasonable model to use to extrapolate radio sources to microwave frequencies. Although subject to systematic errors on a galaxy-by-galaxy basis, we expect our overall extrapolation results to be accurate to within a factor of two at 90 GHz.

Our analysis of foreground confusion from extragalactic radio sources indicates that they contribute negligibly to COBE resolution observations of the CMB, consistent with the conclusion of Banday et al. (1996). However, they do become problematic at higher resolution. Our results set a lower limit on the anisotropy and provide a list of the brightest sources in the sky which can be used to mask pixels in future high-resolution CMB observations. The contribution of extragalactic radio sources to CMB anisotropy is comparable at 200 GHz to that of bright extragalactic infrared sources (Gawiser & Smoot 1997; Toffolatti et al. 1998). Our current results indicate a valley at around 200 GHz where the anisotropy from radio sources is a minimum; adding in the contribution from infrared-bright galaxies should move that valley towards 150 GHz.

The results of this investigation motivate an expansion of our catalog so that sources which will contribute to anisotropies on the 1σ level can be masked. It is clear that the current generation of CMB anisotropy experiments must pay close attention to the possibility of radio point source contamination at all frequencies. Masking pixels which contain bright radio galaxies should reduce this foreground to a manageable level.

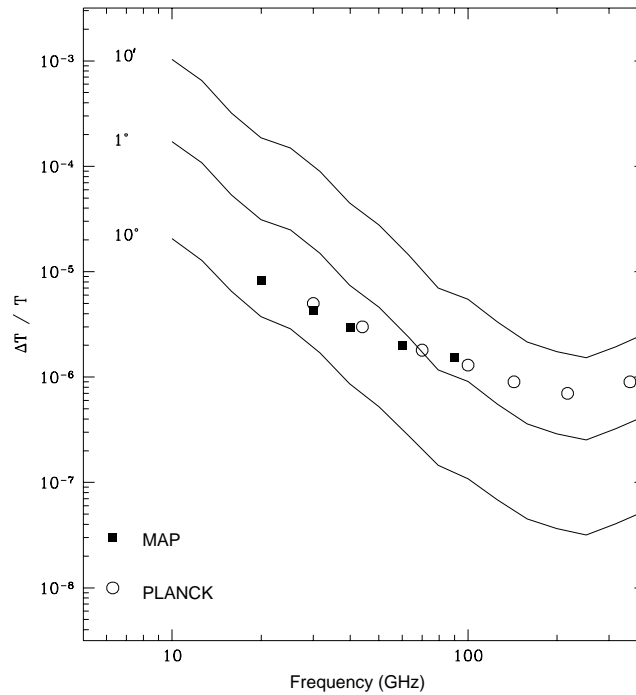


Figure 9.2: Microwave anisotropy from radio sources

Plot of $\log_{10} \frac{\Delta T}{T}$ in the northern celestial hemisphere (without pixel subtraction) versus frequency for instrument resolutions of $10'$, 1° , and 10° , showing window where foreground confusion should be $\simeq 10^{-6}$. The rise beyond 200 GHz is caused by the exponential falloff in CMB antenna temperature beyond 100 GHz. The 5σ -source subtracted predictions for MAP (solid squares) and Planck (open circles) from Table 9.4 are also shown. The $1/FWHM$ scaling will extend to other instrument resolutions but the 5σ source detection threshold is mildly instrument dependent.

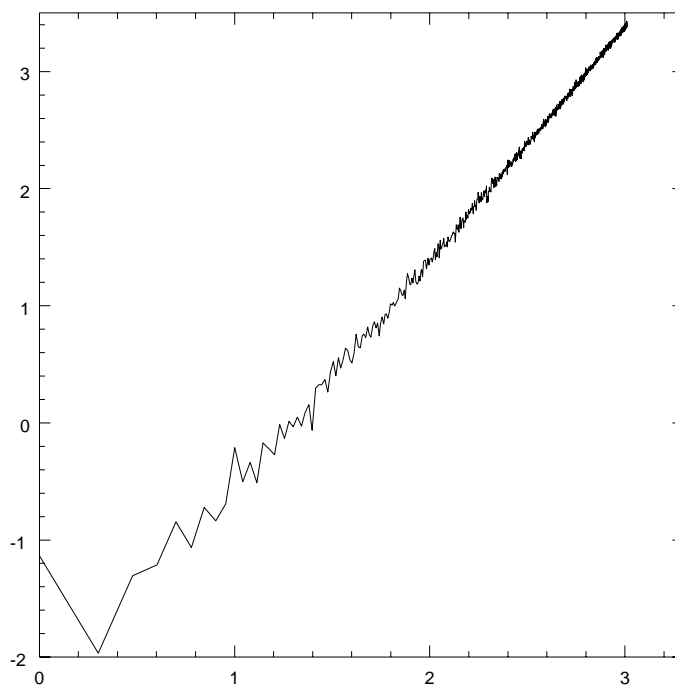


Figure 9.3: Plot of predicted $\log(\ell(\ell + 1)C_\ell)$ vs. $\log_{10}\ell$ for the radio catalog extrapolated to 100 GHz and pixelized at HEALPIX level 1024 (3.4' pixels).

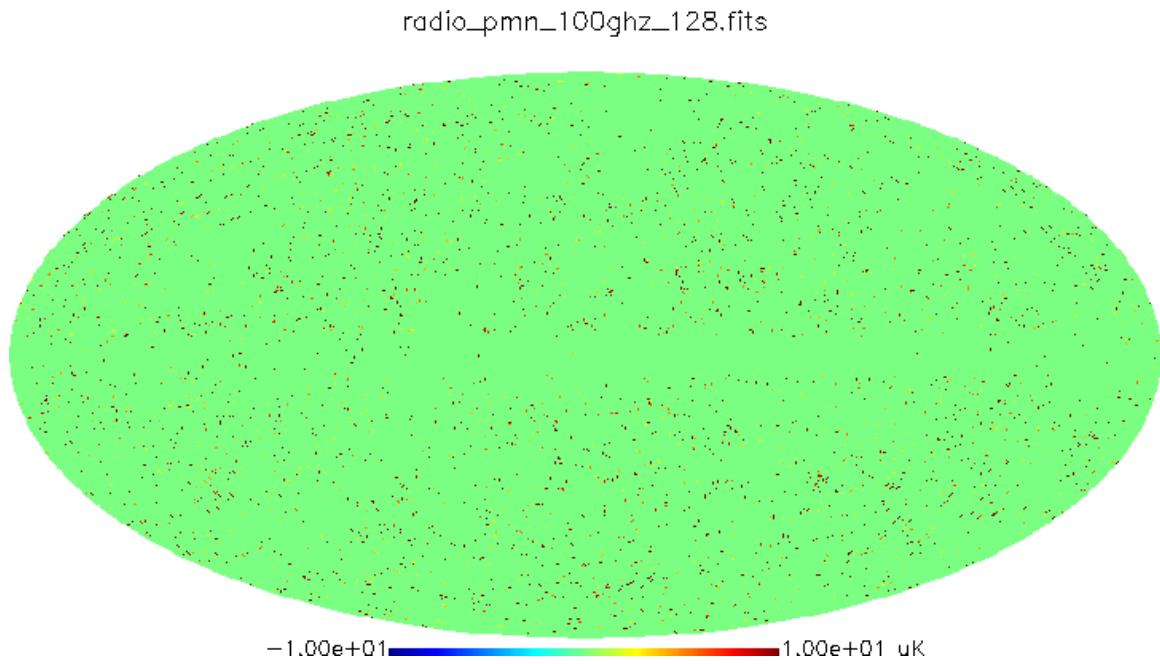


Figure 9.4: Sky map in Galactic coordinates of our catalog of radio sources (including PMN) extrapolated to 100 GHz and pixelized at HEALPIX level 128 ($0^{\circ}.5$). The color table (in units of thermodynamic temperature fluctuations) reaches a maximum for all sources which will be directly detectable by future satellites.

Chapter 10

Observational Limits on Anisotropy from Point Sources

10.1 Motivation

Improved instrumentation and the upcoming MAP (Microwave Anisotropy Probe) and Planck Surveyor satellite missions focus current attention on angular scales between one-half and one-tenth of a degree, and there is theoretical motivation for undertaking future observations at even smaller scales (Hu & White 1997b; Metcalf & Silk 1998; Jaffe & Kamionkowski 1998). Because the antenna temperature contribution of a point source is inversely proportional to the solid angle of the beam, observations at higher angular resolution are more sensitive to foreground contamination from point sources, including the radio sources and low- and high-redshift infrared-bright galaxies which have already been discussed and the Sunyaev-Zeldovich effect from galaxy clusters (see Chapter 11). The dominant contribution of the Galaxy to microwave anisotropy is from diffuse emission (Toffolatti et al. 1998; Finkbeiner 1999).

Until recent SCUBA observations, almost all sources observed from 10-1000 GHz were selected at higher or lower frequencies, so there was little direct knowledge of point source populations with emission peaking in this wide frequency range. Blain et al. (1998a) (see also Blain et al. 1998b and Scott & White 1999) use models for high-redshift galaxies normalized to SCUBA counts at 353 GHz to predict anisotropy from extragalactic point sources down to 100 GHz, but this extrapolation is highly model-dependent. Previous pre-

dictions of the total point source contribution (Toffolatti et al. 1998; Toffolatti et al. 1995; Franceschini et al. 1989; Wang 1991) used galactic evolution models with specific assumptions about dust temperatures and luminosity evolution to predict the level of point source contamination. More phenomenological approaches (see Chapters 8 and 9 and Tegmark & Efstathiou 1996) lack information on infrared galaxies at high redshift and on dim but numerous radio sources.

Cosmic microwave background observations contain contributions to anisotropy from two groups of point sources. The bright sources at a level of at least 5σ (σ is the quadrature sum of instrument noise, CMB fluctuations, diffuse Galactic emission, and underlying point source fluctuations) can be detected individually and eliminated by masking the pixels containing them. This detection limit can be lowered by using prior knowledge of the locations of bright sources obtained from extrapolating far-infrared and radio frequency observations as described in Chapter 8 and 9 (as well as filtering, fourier transform, and wavelet techniques; see Tegmark & De Oliveira-Costa 1998; Ferreira & Magueijo 1997; Tenorio et al. 1999). Numerous dimmer sources will add to anisotropy but cannot be detected without performing further observations at higher resolution at nearby frequencies. For most planned CMB observations, these simultaneous observations will be difficult due to large sky coverage at high resolution of the primary instrument (although Planck's wide frequency coverage will help with foreground subtraction.)

We utilize recent sub-arcminute resolution observations to constrain the contribution to anisotropy from this second group of point sources that will inevitably contaminate measurements of CMB anisotropy. Recent observations using BIMA by Wilner & Wright (1997) detected no sources brighter than 3.5 mJy in the 15 arcmin² of the Hubble Deep Field (HDF) at 4.7'' resolution at 107 GHz. We combine this constraint with the counts of sources detected in blank fields at 353 GHz by SCUBA (Hughes et al. 1998; Barger et al. 1998; Eales et al. 1998) and at 8.4 GHz with the VLA (Richards et al. 1998; Fomalont et al. 1997) , with blank field upper limits from BIMA/OVRO at 28.5 GHz (Holzapfel 1998; Carlstrom 1998) , SuZIE at 142 GHz (Church et al. 1997) , IRAM at 250 GHz (Kreysa 1998; Grewing 1997) , SCUBA at 667 GHz (Hughes et al. 1998) , and CSO at 850 GHz (Phillips 1997) , and with the detection of Far-Infrared Background radiation in FIRAS data (Puget et al. 1996; Burigana & Popa 1998; Fixsen et al. 1998) .

It has long been feared that a population of sources with spectra peaking near 100 GHz, due to self-absorbed radio emission or thermal emission at very high redshift, might

remain undetected by radio and far-infrared observations while contributing significantly to measurements of CMB anisotropy. Now that high-resolution observations are available in the frequency range relevant to CMB anisotropy observation, we set upper and lower limits on point source confusion between 10 and 1000 GHz by assuming that the emission of point sources originates from the well-understood physical processes of synchrotron, free-free, thermal dust, and spinning dust grain emission.

10.2 Extragalactic Point Sources

The main emission mechanism of bright far-infrared sources is graybody reradiation of starlight and/or Active Galactic Nuclei (AGN) radiation absorbed by dust. Chapter 8 predicted the level of microwave anisotropy from the 5319 low-redshift infrared-bright galaxies in the IRAS 1.2 Jy survey. We expect there to be numerous higher-redshift starburst galaxies like the prototypes Arp 220, F 10214+4724, SMM 02399-1236 (Ivison et al. 1998; Frayer et al. 1998), and APM 08279+5255 (Lewis et al. 1998) which generate similar dust emission, and with their spectra redshifted considerably these sources could easily be missed by far-infrared surveys and yet make significant contributions to the microwave sky. There may well exist a population of ultraluminous proto-elliptical galaxies which cannot be described by models using smooth evolution of the IRAS luminosity function. Recent detections of the Far-Infrared Background radiation and of submillimeter sources by SCUBA (Smail et al. 1997, 1998) give us the first clues about the nature and abundance of these high-redshift objects.

A separate population of extragalactic point sources are radio-loud, typically elliptical galaxies or AGN. Radio sources which have nearly flat spectra up through microwave frequencies are called blazars, a class which includes radio-loud quasars and BL Lacertae objects. Chapter 9 examined 2207 bright radio sources in detail, but there are over ten thousand of these sources which are bright enough to have some impact on arcminute-resolution microwave observations.

For instruments of resolution $\geq 10'$, galaxy clusters will be unresolved and will provide an additional family of point sources via the Sunyaev-Zeldovich effect (Sunyaev & Zeldovich 1972). The observations used here are basically insensitive to SZ clusters as the fields have been chosen to avoid known clusters and are typically observed at sub-arcminute resolution. However, anisotropy from SZ sources is not expected to seriously impair CMB

anisotropy observations (Refregier et al. 1998; Aghanim et al. 1997).

10.3 Analysis

We assume for these calculations that observations use pixels of width equal to the FWHM of their beam. A chosen amount of overpixelization will lead to a small, calculable correction in the level of anisotropy and makes it easier to distinguish point sources, which contribute to several pixels, from instrument noise, which is often uncorrelated between neighboring pixels.

We can rigorously predict the fluctuations due to sources using the techniques of $P(D)$ analysis (Scheuer 1957, 1974; Condon 1974; Franceschini et al. 1989; Toffolatti et al. 1998) . To begin, we must estimate the cumulative flux distribution of sources, $N(> S) = \int_S^\infty N(S) dS$. The SCUBA results give a list of sources and their fluxes with error bars; they also provide a limit on the low-flux tail of the distribution from their measured residual fluctuations (Hughes et al. 1998) . We estimate $N(> S)$ directly, using a Gaussian of width given by the error on the observed flux for each source. We calculate 2σ error bars on $N(> S)$ for this estimated distribution by having the fluctuations in number be consistent with Poissonian fluctuations for each cumulative distribution. We use a top-hat experimental beam to convert $N(> S)$ to an observed flux distribution. We then convert this to the probability distribution, $P(D)$, of getting a total flux, D , in the beam (Scheuer 1957, 1974; Condon 1974). Whereas the integrated background is determined by the slope and low-flux cutoff of $N(> S)$, the anisotropy is dominated by the brightest sources seen by SCUBA.

We consider both the detected sources and the rms noise in the instrument. The observed instrument noise is usually roughly Gaussian with mean near zero. This provides a good upper limit on confusion from undetected sources because one can bury only about half that noise in anisotropy from dim sources without increasing the mean noise level by much or making the noise distribution noticeably non-Gaussian. Hughes et al. report a noise level of 0.45 mJy per $8.5''$ beam. To allow for the possibility that a large fraction of this may actually be from sources, we define the total flux, y , the sum of D and this noise contribution. We take the noise distribution to be a zero-mean Gaussian with the reported variance, scaled by the desired beam area. The distribution of y is just the convolution of $P(D)$ and the noise distribution. From $P(D)$ or $P(y)$ we determine the impact on CMB

measurements by estimating the variance (σ_D and σ_y). Our 2σ upper and lower limits from SCUBA at 353 GHz are 67 mJy and 8 mJy respectively. Such careful calculations are not strictly necessary; the following easily-reproduced back-of-the envelope calculation is accurate to within a factor of two, adequate for present purposes.

Our upper and lower limits correspond to 2σ confidence levels from the reported observations. If an observational field contains N_{obs} sources, we estimate the upper/lower limit on the number of sources N in a typical such field on the sky using $N_{obs} = N \pm 2\sqrt{N}$, which leads to limits on the fluctuation of the number of sources in a typical field on the sky of $\sqrt{N} = \sqrt{N_{obs} + 1} \pm 1$.

For N sources with flux S per beam, the rms flux anisotropy on the sky is

$$\Delta S = S\sqrt{N} \quad (10.1)$$

in the Poissonian limit of large N . Toffolatti et al. predict a negligible contribution from non-Poissonian clustering of sources for beams of $10'$ and larger. Scott & White (1999), however, suggest that clustering will lead to fluctuations twice as large as Poissonian fluctuations for a $10'$ beam, with less enhancement at higher resolution. For $N < 1$ (one source per several beams), we have only a few pixels receiving flux, the mean flux is NS , and

$$\Delta S = \sqrt{N(S - NS)^2 + (1 - N)(NS)^2} = S\sqrt{N - N^2} \quad , \quad (10.2)$$

which also tends towards $S\sqrt{N}$ as N becomes small.

We extrapolate our upper and lower limits from an observed frequency by using the most extreme known physical emission mechanisms in that frequency range; the fastest the flux should fall is as very steep spectrum synchrotron emission, i.e. ν^{-2} (Steppe et al. 1995), or above 300 GHz as a Wien tail with ν^1 emissivity, i.e. $\nu^3/(\exp(h\nu/kT_{CMB}) - 1)$, since it is unreasonable for a cosmological object to have an effective temperature less than T_{CMB} . Conversely, the fastest a spectrum should be able to rise is as Rayleigh-Jeans thermal emission with ν^2 emissivity, i.e. as ν^4 . Free-free and spinning dust grain emission (Draine & Lazarian 1998a,b) produce less conservative extrapolations.

The way to maximize anisotropy for the observed integrated Far-Infrared Background is to make individual sources as bright as possible. The low emissivity ($\nu^{0.6}$) fit by Fixsen et al. (1998) means that no one graybody spectrum (emissivity between ν^1 and ν^2) can be responsible for the FIRB. Therefore, we set upper limits on the anisotropy at a

given frequency by making hypothetical sources whose spectra peak at that frequency be as bright as possible. The brightness of these high- z IR sources is constrained by requiring their dust to have temperature greater than 20K (since low- z inactive spirals have 20K dust) and greater than $3K(1+z)$ (so that the dust is never colder than the CMB at that redshift), and to have a bolometric luminosity no greater than that of a quasar (10^{39} W). We also examine a second model where the luminosity constraint is raised to 10^{41} W, the likely luminosity of APM 08279+5255 once lensing is accounted for (Lewis et al. 1998) . Using these constraints, we predict an upper limit of $\Delta T/T = 10^{-6}(10^{-5})$ for a $10'$ beam at 200 GHz for a high- z IR population of luminosity 10^{39} W (10^{41} W) whose total emission generates the FIRB. However, this upper limit is less robust than those from direct observations, because there could be separate source populations, one which yields the integrated background but small fluctuations on the relevant angular scales, and another which dominates the flux anisotropy but produces only a small fraction of the FIRB.

Flux variation is converted to antenna temperature and thermodynamic equivalent temperature fluctuations using Equations 8.1 and 8.3. This yields an equivalent thermodynamic temperature variation which scales as fwhm^{-1} for a given flux anisotropy on $10'$ scales:

$$\frac{\Delta T}{T_{CMB}} = \Delta S_{10'}(Jy) \left(\frac{\text{fwhm}}{10'} \right)^{-1} (5 \times 10^{-4}) \left(\frac{(e^x - 1)^2}{x^4 e^x} \right) . \quad (10.3)$$

The fwhm^{-1} behavior occurs because the number of sources in a beam, N , is proportional to fwhm^2 , the flux variation ΔS due to Poissonian clustering is proportional to \sqrt{N} and the temperature fluctuations after beam convolution are given by $\Delta T \propto (\Delta S)\text{fwhm}^{-2} \propto \text{fwhm}^{-1}$.

10.4 Results

Table 10.3 shows our upper limits for the possibility of dim sources buried in the instrument noise of non-detections, and Table 10.3 lists source detections and the resulting limits on $\Delta S_{10'}$. Figure 10.1 shows our upper and lower limits for flux anisotropy from point sources from 10-1000 GHz, as well as the results for the extreme models of the Far Infrared Background radiation.

We plot the resulting limits on temperature anisotropy in Figure 10.2 for a range of angular scales and frequencies. The less robust nature of the FIRB constraint prevents

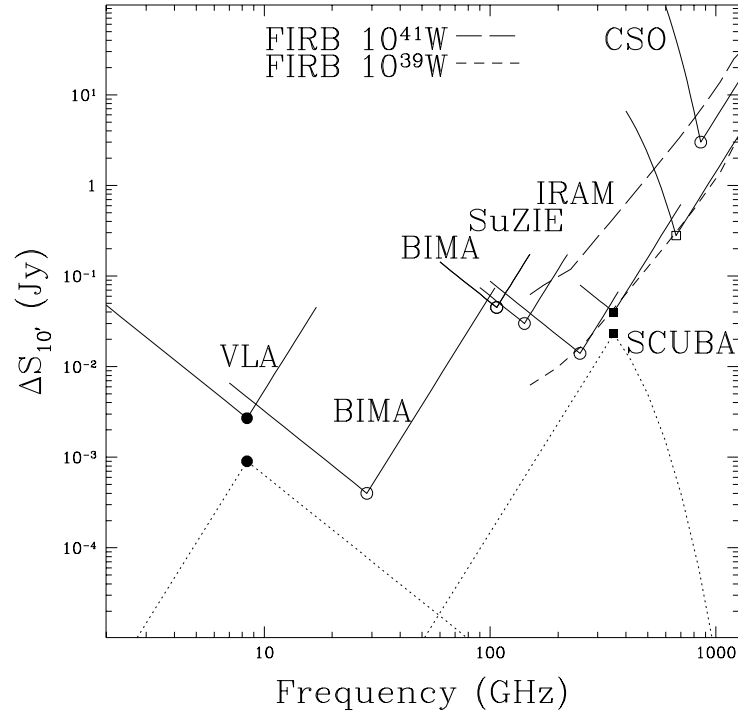


Figure 10.1: Limits on flux anisotropy.

Upper (solid) and lower (dotted) limits on flux anisotropy (in Jy) for a $10'$ beam from VLA, BIMA/OVRO, BIMA, SuZIE, IRAM, SCUBA (squares), and CSO. Filled points indicate detections, open points are non-detections, and the extrapolations are based on steep-spectrum radio emission, Rayleigh-Jeans thermal emission with ν^2 emissivity, and Wien tail thermal emission with ν^1 emissivity. The long (short) dashed lines indicate the upper limit on flux anisotropy derived from extreme models of the Far-Infrared Background radiation with a maximum source luminosity of 10^{41}W (10^{39}W).

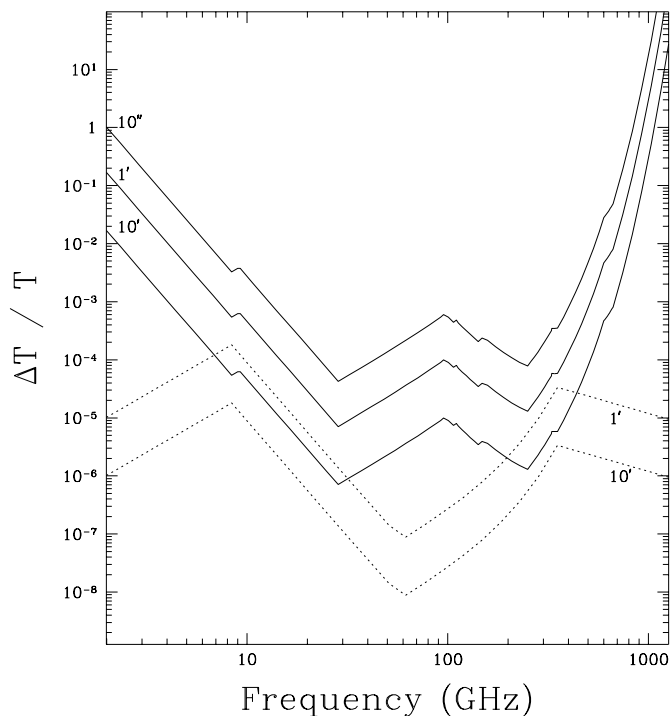


Figure 10.2: Limits on temperature anisotropy.

Net upper and lower limits on $\Delta T/T$ for $10''$, $1'$, and $10'$ based on the observations and extrapolated limits shown in Figure 10.1. The lower limit for $10''$ is zero because all sources detected by SCUBA and the VLA should also be detected and subtracted by future observations at that resolution. The upper limits are based on assuming that the combination of instrument noise and CMB fluctuations is too high to subtract any of the SCUBA or VLA sources.

Table 10.1: Noise levels in high-resolution microwave observations.

We list the frequency, resolution, noise per beam, and the upper limit for $\Delta S_{10'}$ that results from assuming that half of this noise is really produced by unresolved point sources.

Instrument	ν (GHz)	FWHM	Noise/beam	$\Delta S_{10'}^{upper}$
VLA	8.4	6''	0.0028 mJy	0.14 mJy
BIMA	28.5	90''	0.12 mJy	0.4 mJy
BIMA	107	4.7''	0.7 mJy	45 mJy
SuZIE	142	100''	10 mJy	30 mJy
IRAM	250	11''	0.5 mJy	14 mJy
SCUBA	353	15''	0.45 mJy	16 mJy
SCUBA	667	7.5''	7 mJy	280 mJy
CSO	857	10''	100 mJy	3000 mJy

us from using this as an upper limit in Figure 10.2. Because the angular power spectrum C_ℓ of Poissonian distributed point sources increases with multipole ℓ relative to the expected CMB angular power spectrum (Scott & White 1999) and the rms temperature fluctuation is an integral over this power spectrum, an rms $\Delta T/T$ from point sources close to 10^{-5} will seriously impair the measurement of the CMB angular power spectrum on the smallest angular scales. However, a value less than 10^{-6} means that foreground contamination is not a major concern. The $10'$ lower limit shows that $\Delta T/T < 10^{-6}$ is only possible from 20-300 GHz, and the upper limit for $10'$ shows that $\Delta T/T < 10^{-6}$ at 30 GHz and $\Delta T/T \simeq 10^{-6}$ at 250 GHz. The limits are much less stringent near 100 GHz, where a pathological population of point sources could lead to anisotropy closer to 10^{-5} . Typical radio and far-IR sources that fall within these limits at 30 and 250 GHz will end up much closer to the lower limit near 100 GHz, however. Our upper limit constrains all types of point sources, including any hypothetical high-latitude or halo Galactic point sources. Our limits diverge considerably near 100 GHz, so while they are compatible with the model-dependent extrapolations of Blain et al. and Toffolatti et al. , they would also be compatible with significantly different extrapolations.

Scott & White indicate that clustering may lead to a factor of two amplification of our predictions for a $10'$ beam; the correction is less for higher resolution. However, they adopted the angular correlation function of Lyman-break galaxies observed in a narrow redshift range, whereas the SCUBA sources are expected and observed to follow a much

Table 10.2: Microwave source detections.

Upper and lower limits correspond to the observed fields being 2σ Poissonian fluctuations above or below the typical source density on the sky (see text). The totals include the noise totals given in Table 1 added in quadrature with the limits from each source population. The range of sources in the $> 3\text{mJy}$ SCUBA bin allows for the incompleteness correction suggested by Eales et al. and the approximate number in the $1 - 2\text{mJy}$ bin is based on the P(D) analysis of Hughes et al.

Instrument	ν (GHz)	Field size	S_{source}	$N_{sources}$	$\Delta S_{10'}^{upper}$	$\Delta S_{10'}^{lower}$
VLA	8.4	40 sq. '	> 0.5 mJy	3	2.6mJy	0.9 mJy
			0.05-0.5 mJy	8	0.4 mJy	0.2 mJy
			0.009-0.05 mJy	18	0.1 mJy	0.08 mJy
			0.006-0.009 mJy	19	0.04 mJy	0.03 mJy
			TOTAL		2.7 mJy	0.9 mJy
SCUBA	353	46 sq. '	> 3 mJy	15-20	29 mJy	16 mJy
		9 sq. '	2-3 mJy	2	12 mJy	7 mJy
		9 sq. '	1-2 mJy	$\simeq 18$	18 mJy	15 mJy
		TOTAL		40 mJy	23 mJy	

broader redshift distribution (Barger et al. 1999; Richards 1999), leading to a factor of 4-10 reduction in the angular correlation function (as discussed in Section 7.4).

The blank fields observed by VLA, BIMA, IRAM, SCUBA, and CSO were chosen to avoid known bright point sources. Therefore, for observations which avoid known bright sources or mask the pixels containing them, Figure 10.2 gives full upper and lower limits on point source anisotropy. Chapters 8 and 9 have analyzed the contribution of bright infrared and radio point sources, respectively, so for a randomly chosen location on the sky the expected anisotropy is the quadrature sum of the anisotropies from those types of bright sources and our result in Figure 10.2. Figure 10.3 adds in results for known bright sources from Chapters 8 and 9 for a $10'$ beam and shows the results for MAP and Planck after subtracting sources detected at 5σ . Since $\Delta T/T$ is strongly influenced by a few bright pixels due to the highly non-Gaussian distribution, the values are significantly lower after bright source subtraction. Figure 10.3 shows that for a $10'$ beam without source subtraction, the point source anisotropy will be $\geq 10^{-6}$ at all frequencies. From 70-200 GHz, the upper limit from Figure 10.2 dominates the anisotropy from known bright radio and IRAS sources. MAP and Planck can detect the brightest few hundred sources at each frequency (see Chapter 9) so the upper and lower limits for the satellites diverge over a wider frequency

range, making the impact of our uncertainty about the level of anisotropy from dim but numerous point sources a significant problem in predicting foreground contamination. The highest-frequency Planck channels can detect nearly all 5319 IRAS 1.2 Jy sources, so it is the dimmer high-redshift IR galaxies constrained by SCUBA that dominate their source confusion. Our limits here treat each channel independently, but it will be possible to detect bright sources at particular frequencies and mask the corresponding pixels in all channels. This will enhance the importance of dim but numerous sources relative to known bright sources but will reduce the overall level of foreground contamination.

10.5 Discussion

We find impressive agreement between the SCUBA observations, the IRAM and SCUBA upper limits, and the upper limit for flux anisotropy produced by $10^{39}W$ sources which generate the integrated Far-Infrared Background shown in Figure 10.1. This is consistent with the FIRB being produced by the SCUBA sources (since the upper limits and the detections differ by only a factor of two), and this indicates that the FIRB sources must be close to maximizing their anisotropy i.e. they are highly luminous but not too numerous. The $10^{41}W$ model, however, predicts more anisotropy than is consistent with the observed SCUBA source counts and IRAM and SCUBA upper limits, suggesting that starburst galaxies like APM 08279+5255 are more luminous than typical FIRB sources. This conclusion is also supported by the near-blackbody spectrum of APM 08279+5255 in the sub-millimeter; there is no way to sum such spectra at various redshifts and produce a graybody of emissivity 0.6 as is seen for the FIRB (Fixsen et al. 1998). The IRAM upper limit is low enough to show that the far-IR sources detected by SCUBA have rising spectra, so this is further evidence that their emission is thermal in origin.

The CMB anisotropy damping tail on arcminute scales is a sensitive probe of cosmological parameters and has the potential to break degeneracies between models which explain the larger-scale anisotropies (Hu & White 1997b; Metcalf & Silk 1998). The expected level of temperature anisotropy is $\Delta T/T \simeq 10^{-6}$, which Figure 10.2 indicates may be enough to dominate the point source confusion from 30-200 GHz. The upper limit on point source confusion, however, would completely swamp the fluctuations of the damping tail, so more knowledge of dim sources is needed before we can expect such observations to be feasible. A high resolution instrument will probably need to use its highest resolution for point source

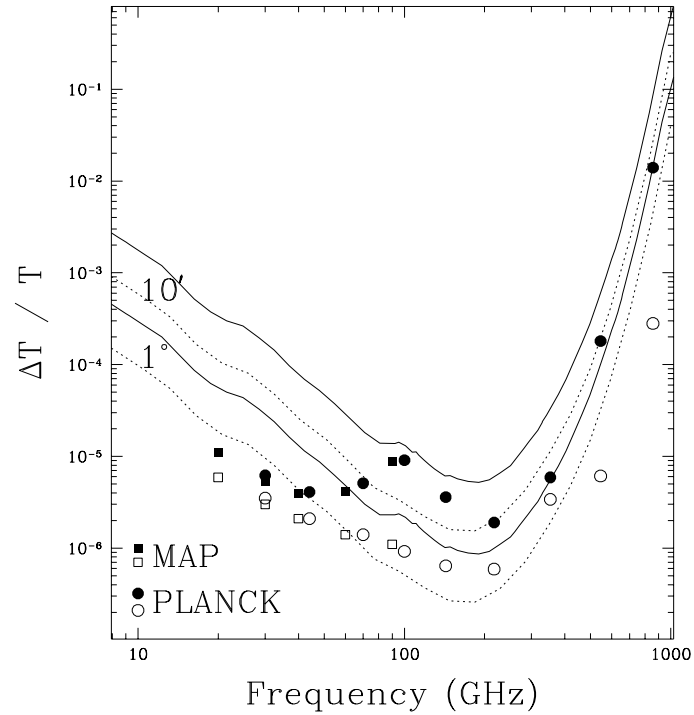


Figure 10.3: Net upper (solid line) and lower (dotted line) limits for $10'$ and 1° .

This includes anisotropy for known bright sources from Figures 8.3 and 9.2 with a factor of three uncertainty shown. 5σ subtracted upper (solid) and lower (open) limits for MAP (squares) and Planck (circles) are also shown. The channels are treated independently here, although in practice they could be combined to produce somewhat lower anisotropy levels. The combination of pixelization and beam-size effects discussed in the text leads to $1/\text{fwhm}$ scaling for all of these point source populations.

detection and subtraction.

The greatest promise for seeing CMB anisotropies through the obscuration of point source confusion occurs near 100 GHz, but this is also the frequency range where we know the least about the true level of foreground anisotropy on the sky. Our upper limits for $10'$ near 100 GHz give us confidence that useful information will be obtained from CMB anisotropy observations, but it remains possible that point sources will cause thermodynamic fluctuations almost equal to the intrinsic CMB fluctuations. Probably the true upper limit near 100 GHz is a factor of a few lower than shown, because the sources responsible for the current upper limit would need to have spectra rising like a graybody but falling off like a steep spectrum radio source; this is either unphysical or requires an effective temperature less than that of the CMB. Since the point source fluctuations come from the highest multipoles, this could seriously impair attempts to measure cosmological parameters from the CMB angular power spectrum. Thus, further high-resolution observations of blank fields at frequencies near 100 GHz are critical in order to determine the actual level of point source confusion, and CMB anisotropy analysis methods must account carefully for contamination from point sources.

Chapter 11

The Sunyaev-Zeldovich Effect

11.1 Theory

Rich clusters of galaxies contain hot electron gas which scatters the Cosmic Microwave Background photons, leading to a temperature decrement at frequencies less than 217 GHz and a temperature increment at higher frequencies (relativistic corrections lead to a slight modification of this spectral signature). This is called the thermal Sunyaev-Zeldovich effect (see Holder & Carlstrom 1999 for a review). There is also a kinetic SZ effect due to a cluster's peculiar velocity; this Doppler shift of the apparent CMB temperature is independent of frequency and is very difficult to detect. The SZ effect may also be produced by the lobes of radio galaxies (see Yamada et al. 1999) or by patchy early reionization around quasars (see Aghanim et al. 1996; Gruzinov & Hu 1998; Knox et al. 1998) and in the Lyman α forest (Loeb 1996).

For long-wavelength observations, the Sunyaev-Zeldovich effect in galaxy clusters will produce a temperature shift of

$$\frac{\delta T}{T} = -2y = -2\tau_0 \frac{kT_x}{m_e c^2} \sim -5 \times 10^{-5} h^{-\frac{1}{2}} \quad (11.1)$$

where T_x is the plasma temperature and τ_0 is the optical depth of the cluster plasma (Peebles 1993). This is comparable to the temperature fluctuations in the CMB observed by COBE and can therefore mask the true CMB temperature anisotropies on scales of several arcminutes corresponding to clusters. The SZ effect is a localized spectral distortion and appears as a temperature anisotropy. One way to distinguish it from the true primordial fluctuations in the CMB is to use several different frequencies, including some in the Wien

tail where the SZ effect will increase the apparent temperature.

The frequency dependence of SZ thermodynamic temperature fluctuations is given by

$$j(x) = 2 \frac{\exp(x)}{(\exp(x) - 1)^2} \left(x \frac{\exp(x) + 1}{\exp(x) - 1} - 4 \right) (\cosh(x) - 1), \quad (11.2)$$

where we have defined

$$x \equiv \frac{h\nu}{k_b T_{cmb}}. \quad (11.3)$$

This allows a temperature decrement at a known frequency ν_0 to be extrapolated to a different frequency using

$$dT(\nu) = dT(\nu_0) \frac{j(x)}{j(x_0)}. \quad (11.4)$$

11.2 Simulations

We use the XBACS cluster catalog (Ebeling et al. 1996) to predict the location on the high-Galactic latitude sky ($|b| > 30$) of the 226 brightest SZ sources. Clusters at higher redshift will have less flux, despite comparable temperature decrements, because they are decreasing in angular size (XBACS only covers up to $z = 0.2$). The MAP satellite can hope to detect about 10 SZ clusters at the 5σ level, and to barely resolve Coma and Virgo (Refregier et al. 1998). Once the minimum of the angular diameter distance is neared, the SZ flux from clusters of a given X-ray temperature becomes effectively independent of redshift. Hence, for beams smaller than $10'$, as will be used in the future with Planck HFI and microwave interferometers, clusters at all redshifts will have an impact. Although Planck will also see nearby clusters as brighter than more distant ones, its high sensitivity and improved resolution present the prospect of detecting numerous high-redshift clusters through their SZ effect.

Previous simulations have ignored the known positions and characteristics of nearby galaxy clusters but offer an illustration of the expected number counts of high-redshift clusters, which is strongly dependent on cosmology (Aghanim et al. 1997). For simulations at Planck resolution, we will need to add a simulation of the clusters not included in XBACS using the $N(S)$ predictions of the Press-Schechter method and adopted temperature and density profiles for clusters of a given mass. A complete realistic simulation of the SZ effect from galaxy clusters on the full-sky requires three components:

- XBACS clusters ($z < 0.2$)

- Low-galactic latitude clusters at $z < 0.2$. These must be simulated since they are not present in the XBACS sample.
- Clusters at $z > 0.2$, which also must be simulated because full-sky X-ray surveys to determine their actual locations and fluxes do not exist.

Refregier et al. (1998) used an isothermal beta-model to fit the X-ray data and predict the flux at 90 GHz due to the thermal SZ effect in XBACS clusters. There are two major sources of systematic errors for the predicted 90 GHz fluxes, the overall normalization, which depends on the gas fraction and on the virialization state, and the error in the X-ray temperatures in the XBACS catalog, which were derived from ROSAT spectra. Data from MAP will be used to improve the overall normalization, which can also be tested against N-body simulations. Pending more detailed analysis, we believe that our overall normalization of the predicted 90 GHz fluxes is uncertain by a factor of 1.5, and that the prediction for each cluster is also uncertain by a factor of 1.5. The spectral dependence of the SZ effect is well-understood and should not be a significant source of error.

One possible advantage of having the actual positions of these clusters from the XBACS catalog is that their non-Poissonian clustering is included. However, when we calculate the angular power spectrum at 90 GHz for the XBACS clusters with positions randomized within $|b| > 30$ we find no noticeable difference in the C_ℓ (see Figure 11.1). There is non-Poissonian clustering noticeable to the human eye in the XBACS catalog, and this randomized version has many fewer cases of multiple clusters located near each other on the sky. This indicates that even mildly non-Poissonian clustering of point sources distinguishable by eye is sometimes not sufficient to alter the C_ℓ spectrum from its Poissonian behavior (constant). This is different for high-redshift infrared galaxies because there are many of them per pixel and the fluctuations themselves are therefore magnified by non-Poissonian clustering rather than just redistributing the fluctuations in a more clustered way.

We also explore whether filaments of hot gas connecting and extending from clusters can have an impact on CMB anisotropy (Persi et al. 1995; Boughn 1998). We use a toy model for the filaments where XBACS clusters that are within $50h^{-1}\text{Mpc}$ of each other are connected by a filament and clusters located too far apart to have neighbors in the catalog are assigned two filaments heading in random directions. Each filament is assigned a total number of baryons equal to its cluster endpoint (or the average of its endpoints). Hence if

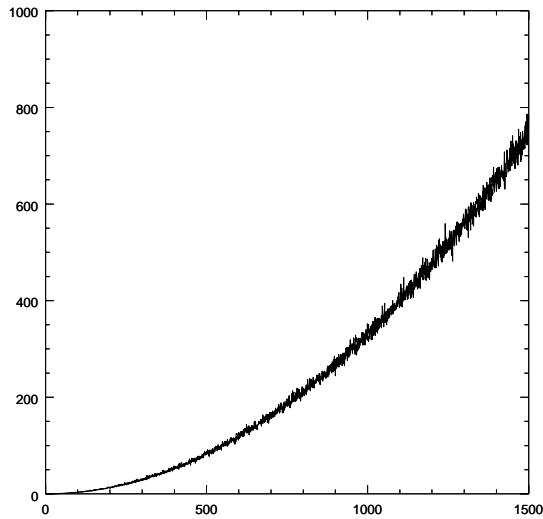


Figure 11.1: Predicted SZ angular power spectra.

$\ell(\ell + 1)C_\ell$ in μK^2 versus ℓ for both the XBACS catalog with clusters at nominal positions and with clusters at random positions. The two curves overlap, illustrating that the visually distinguishable non-Poissonian clustering of the XBACS clusters is insufficient to affect the angular power spectrum of their SZ contribution.

the gas were equally hot in filaments and clusters the total SZ flux from a filament would equal the average of that of its endpoints. This reproduces the rough structure seen in the simulations of Cen & Ostriker (1999)¹. The results of our simulation of the SZ effect from filaments are shown in Figure 11.3. While these filaments look great visually², they are nearly insignificant in comparison to the XBACS clusters themselves in terms of SZ effect because their electron gas temperature is expected to be lower than that of rich clusters by about a factor of 10. Thus even if half of the baryons are in filaments and groups, as predicted, their impact on anisotropy is small. Detecting these filaments by cross-correlating CMB and large-scale structure maps has been discussed by Refregier et al. (1998), and that method can be tested using the WOMBAT Challenge simulations, which contain a variety of models for the filaments as well as systematic variations of the cluster fluxes.

¹ See <http://www.astro.princeton.edu/~cen/PROJECTS/p1/p1.html> for nice visualizations of their simulations.

²and contain the type of patterns that might get significant media attention, especially from the Weekly World News

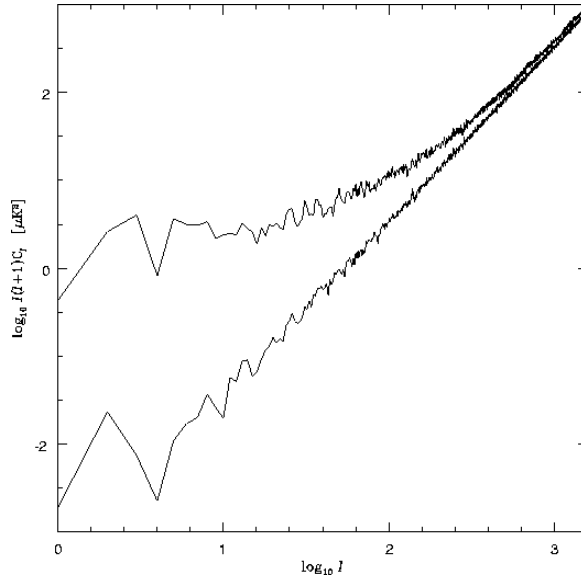


Figure 11.2: Angular power spectra from SZ effect in filaments and clusters.

Log-log plot of $\ell(\ell+1)C_\ell$ versus ℓ for SZ simulation based on XBACS only (lower curve) compared to simulation including filaments as well (upper curve). The high- ℓ behavior is Poissonian, and the filaments have not significantly increased the total power. The filaments lead to significant non-Poissonian clustering on large angular scales, but this effect will be entirely swamped by large-angular CMB fluctuations and Galactic foregrounds.

Combining the SZ effect from clusters and filaments leads to only a small increase in the angular power spectrum, as shown in Figure 11.2. Figure 11.4 shows all of the sources with a wider temperature scale than the plot of filaments alone. The catalog is incomplete at $|b| < 30$ and reveals large-scale structure at $z < 0.2$. However, almost none of the filaments are visible, illustrating that the expected reduction of temperature in the filaments is sufficient to make their SZ effect negligible. The filaments are not detectable by forthcoming CMB instruments, but the XBACS sources are strong. The prediction of Refregier et al. (1998) that MAP can detect about a dozen XBACS clusters is consistent with the results of our simulations.

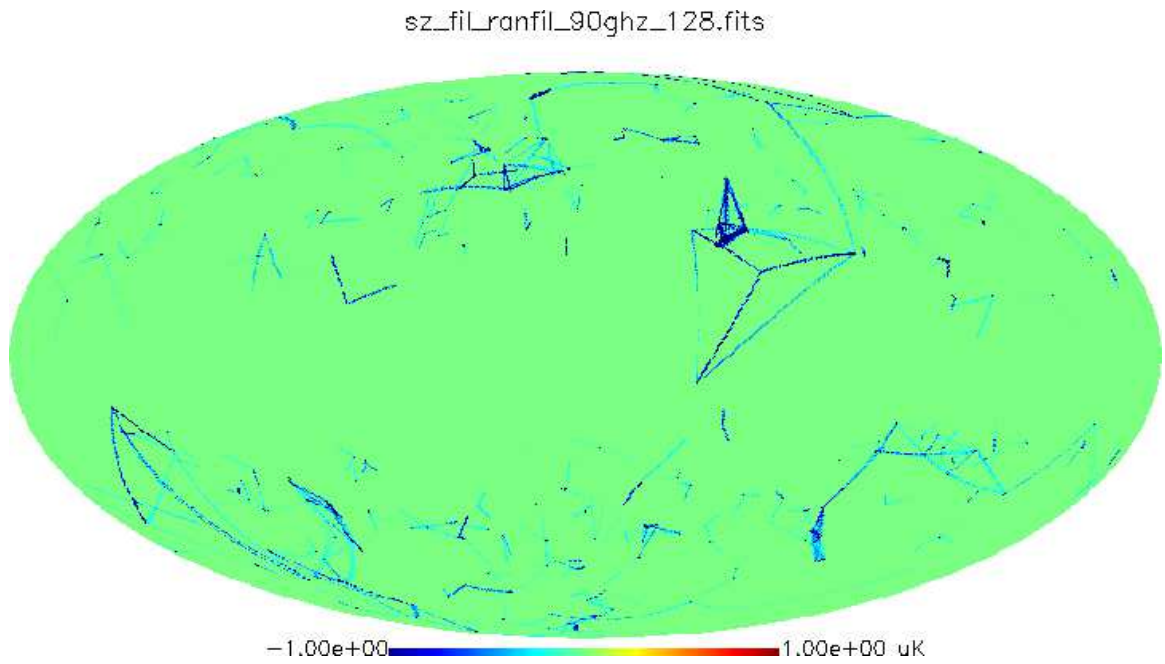


Figure 11.3: Predicted temperature fluctuations at 90 GHz from filaments extending from and connecting XBACS clusters using the toy model described in the text.

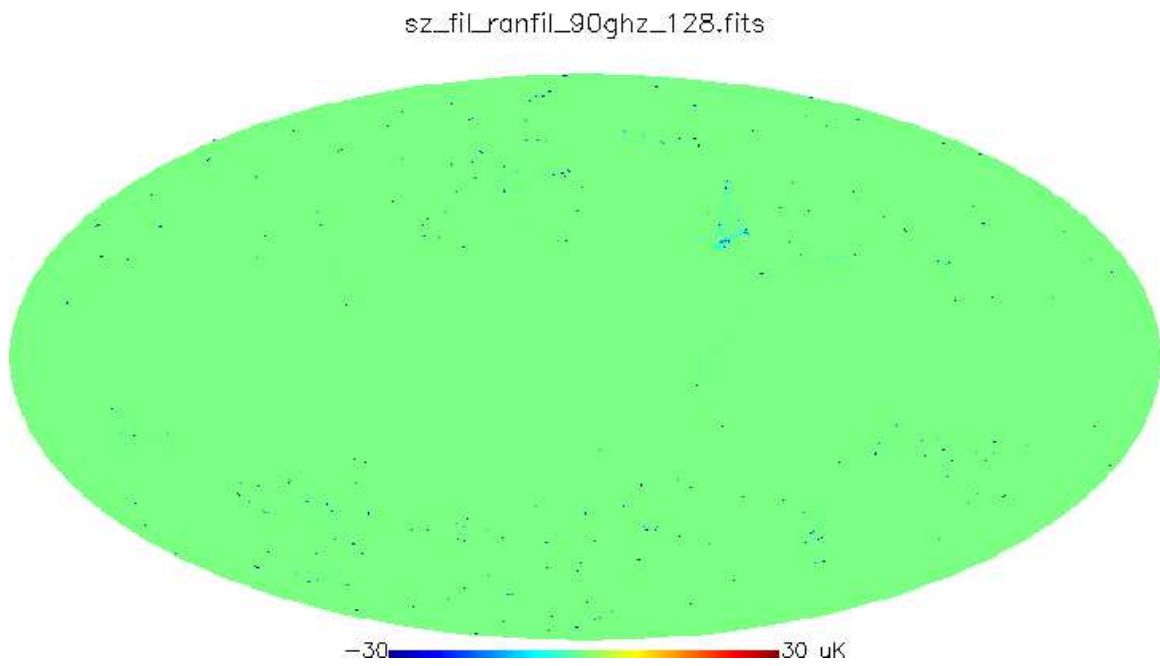


Figure 11.4: Combined prediction of the SZ effect from XBACS clusters and a simulation of the filamentary structure connecting them.

Chapter 12

A Pixel-space Method for Foreground Subtraction

12.1 Motivation

Figure 12.1 shows the anisotropy power spectrum for one of the WOMBAT Challenge simulations at 90 GHz analyzed using the HEALPIX routine `anafast90`. The upper curve is for $|b| > 30$ and the curve below this corresponds to the same region of sky with pixels at the level of 5σ subtracted. As these 5σ pixels are most likely due to extragalactic point sources, this illustrates that extragalactic foreground contamination is considerable but can be reduced significantly by this simple method. The angular power spectrum for Λ CDM is shown for reference (smooth curve). It seems likely that the first acoustic peak of the CMB fluctuations in this simulation is simply higher than that of Λ CDM, as the shape and location of the peak are consistent with a host of models preferred by the current Saskatoon observations, and Galactic and extragalactic foregrounds are unlikely to preserve this shape and amplify it by so much. However, at smaller scales where the second and third acoustic peaks are being sought, it is not certain if the second peak is being seen and no third peak is evident. It is clear that more sophisticated methods are needed to reconstruct the second and third acoustic oscillations to high precision. Figure 12.2 shows these high-Galactic latitude, 5σ pixel-subtracted versions of the anisotropy power spectrum for three additional WOMBAT Challenge simulations. The simulations display a wide range of power at small scales, due to some combination of differences in intrinsic CMB anisotropy,

foreground contamination, and instrument noise.

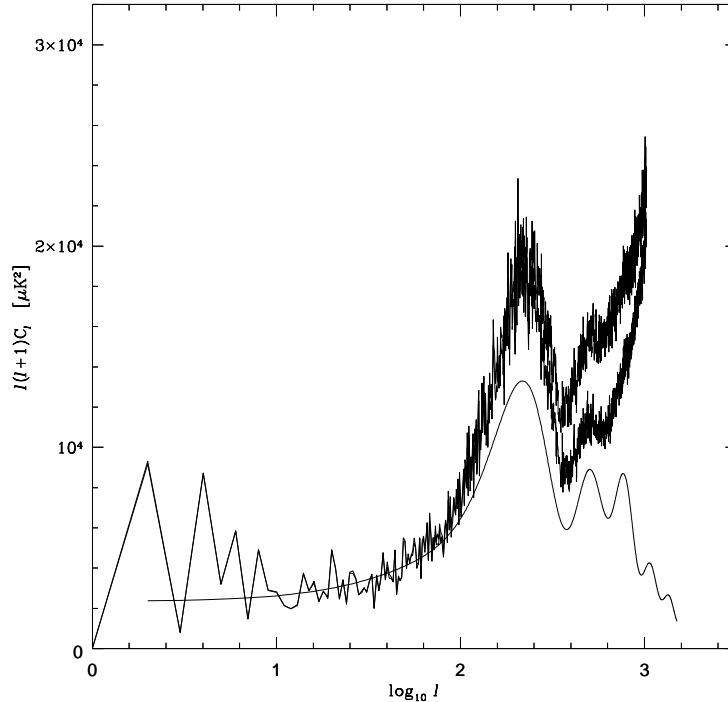


Figure 12.1: C_ℓ for one of the WOMBAT Challenge simulations measured at $|b| > 30$ compared to the expected C_ℓ for Λ CDM.

In practice, foreground contamination of CMB anisotropy observations is typically estimated by cross-correlating template maps at radio or far-IR frequencies with the observations. Either the correlated component proves to be quite small or an attempt is then made to subtract it. On the other hand, most formalized methods of foreground subtraction are performed in Fourier or spherical harmonic space, where phase information about the known spatial distribution of Galactic emission and bright extragalactic point sources is ignored. A fiducial CMB power spectrum must often be assumed, and the risk of aliasing power into or out of the CMB in ℓ -space is great.

The goal here is to design a method for CMB foreground subtraction that is conceptually simple and computationally fast. This is not a detailed method but rather a framework recommending a series of steps and outlining their basic equations; the exact method for a given instrument will require tuning some of the parameters and thresholds of this framework with simulated observations. We will formalize the process of cross-

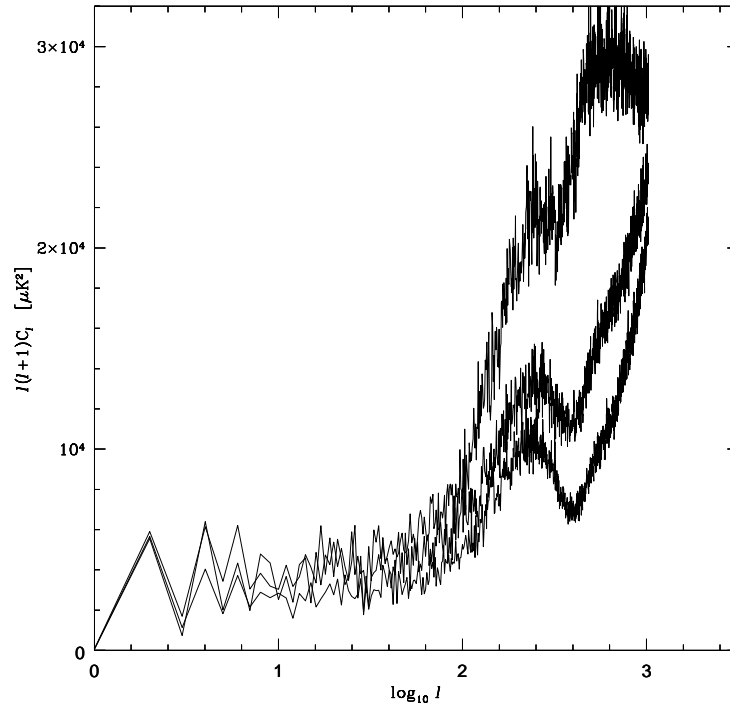


Figure 12.2: C_ℓ for 3 different WOMBAT Challenge simulations, measured at $|b| > 30$ with 5σ pixels subtracted.

correlating and subtracting spatial foreground templates which have been extrapolated to the observing frequency with known systematic uncertainties. Unrealistic idealization of foregrounds can be prevented by keeping a sense of the uncertainties in foreground models and their extrapolations and then admitting that these uncertainties are a source of correlated “noise” in the cleaned map. Where available, we recommend using spatial templates for the foregrounds.

Where spatial foreground templates are not available, one must rely on the thermodynamic nature of CMB fluctuations to distinguish them from foreground contaminants. It is also possible to use the expected difference in angular power spectra but we do not recommend filtering in ℓ -space, as the methods available for that, multi-frequency Wiener filtering and Maximum Entropy (e.g. Tegmark & Efstathiou 1996; Hobson et al. 1998), require a priori assumptions about the CMB power spectrum and can alias power out of true CMB fluctuations. We will be subtracting foregrounds in pixel space; when we cross-correlate with spatial templates this is the same as filtering in $a_{\ell m}$ space (see White 1998)

as the $a_{\ell m}$ of those components are known up to the same correlation coefficient we are determining. An additional phase of ℓ -space filtering could be added, but we prefer working in pixel space where uncorrelated physical processes add and therefore any errors we make in foreground subtraction are uncorrelated with the underlying CMB fluctuations. This means that we can only add power to the CMB map and should never have intrinsic CMB anisotropy power aliased into other components. Since the CMB should dominate the foregrounds at the frequencies and angular resolutions being considered, it makes more sense to allow some foreground power to remain added to the CMB than to let an uncertain fraction of CMB power alias into detected “foregrounds.” Simulations can estimate the residual effect on the C_ℓ , and one should check for the constant- C_ℓ contamination that is characteristic of point sources at high- ℓ .

12.2 Cross-correlation of Foreground Templates

Consider a set of observed CMB skymaps with N_ν channels each at frequency ν . A given map has $N_{p\nu}$ pixels. All maps are assumed to be in units of thermodynamic equivalent temperature fluctuations. Then T_i^ν is the temperature of pixel i at frequency ν . N_i^ν is the expected level of noise in pixel i , with covariance matrix given by $C_{ij,obs}^\nu$. For differential instruments like COBE or MAP, C^ν is nearly diagonal to start, whereas for instruments with significant correlated noise it is already a dense matrix (Dodelson et al. 1995). As we subtract foregrounds we will add uncertainties into the updated covariance matrix C_{ij}^ν but these uncertainties are systematic in nature so the errors are no longer truly Gaussian. Only simulations can tell us how much this matters, because these systematic errors often reflect subjective judgments and do not follow a quantifiable distribution.

Foreground templates for various components μ are F_i^μ and should come with error maps ΔF_i^μ . We envision here using templates for Galactic dust, synchrotron, and free-free emission (from forthcoming $H\alpha$ observations), IRAS galaxies, radio galaxies, and the brightest X-ray clusters. Wherever information is available on the variation of spectral index with position, these templates should be extrapolated to the observational frequencies with the errors increased to reflect uncertainties of the spatial variations.

We can cross-correlate the extrapolated foreground templates $F_i^{\mu\nu}$ which have error maps $\Delta F_i^{\mu\nu}$ and some uncertain overall amplitude of fluctuations, which is acceptable because we will mean-subtract all maps for the purposes of cross-correlation. The value

of $\sum_i F_i^{\mu\nu} T_i^\nu$ or the best-fit line on a basic scatter plot determines the cross-correlation coefficient, $\alpha^{\mu\nu}$, and its uncertainty, $\Delta\alpha^{\mu\nu}$, can be determined from the 1σ uncertainties in the slope of the best-fit line of the scatter plot or from varying the cross-correlation over regions likely to be systematically different such as different Galactic latitudes or opposite celestial hemispheres. Performing this cross-correlation for various patches of sky one at a time (see Jewell et al. 1999) will improve the eventual foreground subtraction but introduces low- ℓ structure in the cleaned map. Some amount of low- ℓ contamination is allowable, so this tradeoff will have to be optimized for each experiment individually. Of course, it is possible to use an observational channel as a foreground template (Dodelson & Kosowsky 1995) but care is needed if that channel contains significant contributions from multiple foregrounds or CMB fluctuations.

Now we can subtract the correlated foreground component (see Jaffe et al. 1999a),

$$T_i^\nu = T_{i,obs}^\nu - \sum_\mu \alpha^{\mu\nu} F_i^{\mu\nu}, \quad (12.1)$$

and account for the added noise using

$$C_{ij}^\nu = C_{ij,obs}^\nu + \sum_\mu (\alpha^{\mu\nu})^2 \Delta F_i^{\mu\nu} \Delta F_j^{\mu\nu} + \sum_\mu (\Delta\alpha^{\mu\nu})^2 F_i^{\mu\nu} F_j^{\mu\nu}. \quad (12.2)$$

One can imagine using multiple templates for the same foreground component sequentially by first subtracting the correlated component of the best template, then forming an orthogonal template using the two best templates and subtracting the component that correlates with this orthogonal template, etc. If many good foreground templates were available, the set of orthogonal templates could be designed from the start, but this is not generally the case, as can be seen by trying to use multiple synchrotron templates to gain more information than is available from the best of them alone.

12.3 Testing for a Thermodynamic Spectrum

Other foreground components (high-redshift IR galaxies, high-redshift clusters, inhomogeneous reionization, and perhaps spinning dust grains) cannot be accounted for with templates. We must therefore scan the dataset to look for non-thermodynamic emission, which is the clearest signal of foreground contamination, as long as the deviation from a thermodynamic spectrum is inconsistent with fluctuations due to the expected instrument

noise (see Brandt et al. 1994). Pixels typically oversample the beam so we can add up to a beam size to reduce the noise and mask suspicious areas. True features on the sky will be convolved by the beam function $B(\theta)$ so we turn that into a symmetric matrix B_{ij} which indicates how much of a signal which fills only pixel i has been convolved into pixel j and vice versa. We will use B_{ij} to choose weights for the pixels around pixel i and form a weighted beam-size average at each frequency:

$$WT_i^\nu = \frac{\sum_j T_j^\nu B_{ij}}{\sum_j B_{ij}} \quad (12.3)$$

with uncertainty given by

$$\Delta WT_i^\nu = \left(\sum_j \frac{B_{ij}}{C_{jj}^\nu} \right)^{-\frac{1}{2}}. \quad (12.4)$$

This formula for the weighted average assumes that the instrument noise is well-approximated as uncorrelated between pixels; if not, the noise covariance matrix can be used to form a more sophisticated set of weights and uncertainties. One could identify 5σ pixels at this point; since sky signals should be as large as the beam this is now the optimal temperature map to use to look for point sources. In fact, this is roughly the method used by available software packages such as DAOPhot, and it may be superior to the wavelet methods which are now being explored (e.g. Tenorio et al. 1999).

Now we can test at location i for a thermodynamic temperature fluctuation, which has the same value of T_i in every channel, by forming the weighted sum over all frequencies of the beam-size weighted temperature at each frequency,

$$WT_i = \frac{\sum_\nu \frac{WT_i^\nu}{(\Delta WT_i^\nu)^2}}{\sum_\nu \frac{1}{(\Delta WT_i^\nu)^2}} \quad (12.5)$$

which we can now test versus the hypothesis that the beam-size weighted temperatures WT_i^ν are all the same by forming

$$\chi^2 = \sum_\nu \frac{(WT_i^\nu - WT_i)^2}{(\Delta WT_i^\nu)^2} \quad (12.6)$$

which should obey a χ^2 distribution with $N_\nu - 1$ degrees of freedom since the mean has been fit to the N_ν data channels.

One decision to be made by each instrumental team is what threshold to use for deciding if a given beam-size area is thermodynamic. We recommend a 3σ detection of non-thermodynamic fluctuations as the threshold, as this should only yield a false positive in one

percent of the beam-size areas of the map, and the cost of losing that much area is small. False negatives are caused by instrument noise conspiring to hide the non-thermodynamic signal, so they become increasingly probable as the amplitude of the non-thermodynamic foreground decreases, which is tolerable. Prior information about point source locations can be used to mask contaminated pixels as well, even if there is great uncertainty in the extrapolated spectrum of the point source. Specifically, any areas where the foreground subtraction uncertainty is greater than the expected level of intrinsic CMB fluctuations should be masked, e.g. on the Galactic plane or at the locations of known 1σ point sources whose fluxes are uncertain by a factor of two.

Typical experiments (like MAP) often have different beam sizes at different frequencies, requiring the smoothing of higher-resolution maps to make the weighted average and test for thermodynamic fluctuations. We advocate an iterative approach where the areas of the high-resolution maps that survive the thermodynamic test at all frequencies are then re-examined with less smoothing. For instruments with broad frequency coverage such as Planck, it may be possible to form a few distinct spectral indices at each beam-size area centered on a given pixel, allowing one to make a color-color plot (Spergel 1998). The advantage of this versus the single χ^2 test is that a beam-size pixel may look thermodynamic at most frequencies and simply have contamination at one extreme of the frequency range. This form of contamination obviously does not require masking at all frequencies, and can even be allowed by setting the “noise” large at the extreme frequencies where the foreground contaminant appears to dominate.

Now we have produced what most methods of power spectrum analysis require as input, a foreground-subtracted map of thermodynamic temperature fluctuations, with all frequency channels combined (although for the highest-resolution analyses it may be preferable to only use the highest-resolution channels). However, our map has a large number of pixels that have been masked. If a method of determining the anisotropy power spectrum requires continuous-sky coverage, these masked areas can be replaced by either zero or the median value of a ring around them with a radius of a few beam widths. This will lose a small amount of high- ℓ structure but that effect can be tested with simulations. However, it is better to utilize a method that will simply ignore the masked pixels (e.g. Oh et al. 1999).

The final “noise” covariance matrix of this weighted average map will have full off-diagonal structure due to uncertainty in foreground subtraction. If an analysis method can

handle large variances, there is no need to fully mask pixels, i.e. their variance can simply be made large. But some methods, such as Fast Fourier Transforms, require assigning equal weight to all pixels, so the ring-replace method or something similar must be used.

This method of foreground subtraction can be tested on the WOMBAT Challenge simulations. This will indicate how feasible it is to subtract foregrounds without appealing to their expected angular power spectra and how much advantage is gained by using known spatial information on the various components.

Chapter 13

Conclusion

13.1 Prospects for Detecting Dusty High-Redshift Galaxies

Figure 13.1 shows that the frequency range covered by FIRST is favorable for the detection of high-redshift star-forming galaxies such as SMM 02399-0136, which was recently detected by Ivison et al. (1998) using SCUBA. SCUBA has good sensitivity but a small field of view, so it will see many dim sources but detect only a few as bright as SMM 02399-0136. FIRST, on the other hand, will be limited by source confusion but can cover a much larger area of sky, leading to a much bigger sample of these ultraluminous objects. The spectrum of the Cosmic Far-Infrared Background detected by Puget et al. (1996) and Schlegel et al. (1998) has a peak indicating dominant contributions from starbursting galaxies near $z = 1 - 3$, and the redshift distribution of sources detected with SCUBA is consistent with this so far (Barger et al. 1999; Hughes et al. 1998; Richards 1999). FIRST source counts and measurements of the spectrum of point source confusion should considerably restrict the set of models of galaxy evolution which are consistent with the FIRB and preliminary SCUBA detections at present.

The 5σ source detection limits plotted in the figure are based on a quadratic sum of instrument sensitivity achievable within a reasonable (10 hour) integration time, confusion from CMB anisotropy, confusion from point sources (see Blain et al. 1998a), and confusion from Galactic cirrus extrapolated as in Toffolatti et al. (1998). The Planck HFI instrument will see thousands of low-redshift galaxies, including all 5319 IRAS 1.2 Jy sources but Planck has too much noise and foreground confusion to see the sources responsible for the far-infrared background radiation. FIRST is the only one of these instruments whose detec-

tion sensitivity limit is dominated by expected Galactic confusion; if that could be further minimized by choosing lower dust-contrast regions, the FIRST detection limits could be up to five times lower (see Figure 13.1), making galaxies like Arp 220 with luminosities around $100 L_*$ which are likely to be missed by SCUBA detectable with FIRST. These limits, combined with FIRST's suitability for wide-area surveys, lead Ivison et al. (1998) to conclude that FIRST could detect about 100 sources similar to SMM 02399-0136 per hour of integration, which would provide us with an invaluable window into the optically-obscured era of star formation which generated the far-infrared background radiation. Because the FIRST frequencies cover the peak of the emission spectrum for galaxies at $z = 3$ (assuming 40K dust), a combination of FIRST photometry with redshifts determined using spectroscopy from optical follow-ups or FIRST itself will allow an examination of the intrinsic luminosity, dust emissivity, and dust mass of these fascinating objects.

13.2 Future Constraints on Structure Formation Models

Figure 13.2 shows the impressive precision with which future observations by the MAP and Planck Surveyor satellites and the Sloan Digital Sky Survey and 2 Degree Field survey should confirm the correct model of structure formation (in this case assumed to be CHDM). Instrumental parameters from Bond et al. (1997) were used to predict the precision of these constraints for CMB anisotropy observations. Hu et al. (1998) look at how well Ω_ν can be determined by SDSS observations, and Wang et al. (1999) examine the ability of combined MAP and SDSS observations to constrain cosmological parameters.

The overlap in scale between microwave background anisotropy detections and large-scale structure observations will increase tremendously in the next several years, and the errors in these measurements will decrease significantly as well. The CMB promises to measure several cosmological parameters to great accuracy, but some parameters such as the fraction of Hot Dark Matter, Ω_ν , are more directly probed by large-scale structure. All of this, of course, assumes that the correct model is one that we will consider, i.e. that we are searching the right parameter space. Instead of searching the adiabatic CDM parameter space to determine the best-fit model (which due to the dangers of relative likelihood analysis might not really be a very good fit), we advocate an empirical approach to structure formation (Gawiser 1998a), where high-precision observations of CMB anisotropy and large-scale structure are first used to determine the validity of the adiabatic CDM

paradigm.

13.3 Conclusions

We have extracted the spectrum of primordial density fluctuations from the current observations of structure formation in the universe and find that it is close to that of the Cold + Hot Dark Matter model and significantly different from that of any other model we have considered. However, a wide range of models agree on a qualitative level with both the high-redshift density variations imprinted in the CMB and the low-redshift inhomogeneities in the galaxy distribution, giving strong evidence for the success of the gravitational instability paradigm of cosmological structure formation. Increasingly precise measurements of the mass density in the universe appear to rule out $\Omega_m = 1$ and the Type Ia supernovae measurements favor a positive cosmological constant. The agreement of Λ CDM with the structure formation data, however, is not particularly good, and it is harmed by adding even a small fraction of Hot Dark Matter. This allows us to set upper limits on the mass of the most massive neutrino of 2 eV, assuming a scale-invariant primordial power spectrum, and of 4 eV, assuming only a scale-free primordial power spectrum (consistent with the vast majority of inflationary models). We have reconciled the Λ CDM model with the existing structure formation observations by appealing to a radically non-scale-invariant primordial power spectrum which features a smooth enhancement on 100-200 Mpc scales. Only further observational data will reveal whether such a feature is actually necessary to explain the origin and nature of structure in the universe. Forthcoming high-precision CMB anisotropy and large scale structure data will provide us with independent probes of the primordial density fluctuations which can be used to test models of structure formation without assuming a particular primordial power spectrum.

We have developed predictions for microwave emission from radio and infrared-bright galaxies and the SZ effect from clusters. These predictions form part of the input information for the WOMBAT Challenge simulations, which are the most realistic simulations to date of the microwave sky. Analysis of these skymaps shows that a reasonable observational window is available for CMB anisotropy measurements. These simulations can be used to test various foreground subtraction methods and to explore systematic errors in cosmological parameter determination. The pixel-space method for foreground subtraction that we have presented may offer an improved method for performing this important task.

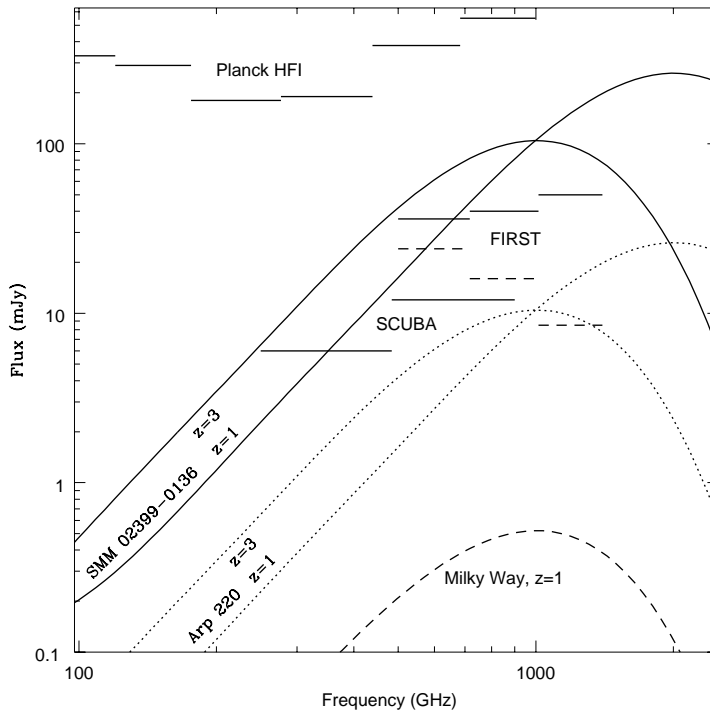


Figure 13.1: Prospects for submillimeter detection of high-redshift galaxies.

The far-IR/sub-mm spectrum of ultraluminous IR galaxies such as SMM 02399-0136 (solid) and Arp 220 (dotted) are shown at $z=1$ and $z=3$, along with a $z=1$ L_* galaxy with the spectrum of the Milky Way (dashed). The expected intensities are compared with the 5σ detection limits of FIRST channels centered at 600, 857, and 1200 GHz, SCUBA channels at 350 and 670 GHz, and Planck HFI channels at 100, 143, 217, 353, 545, and 857 GHz. The dashed version of the FIRST detection limits assumes that the detection limits will be determined by point source confusion rather than Galactic cirrus.

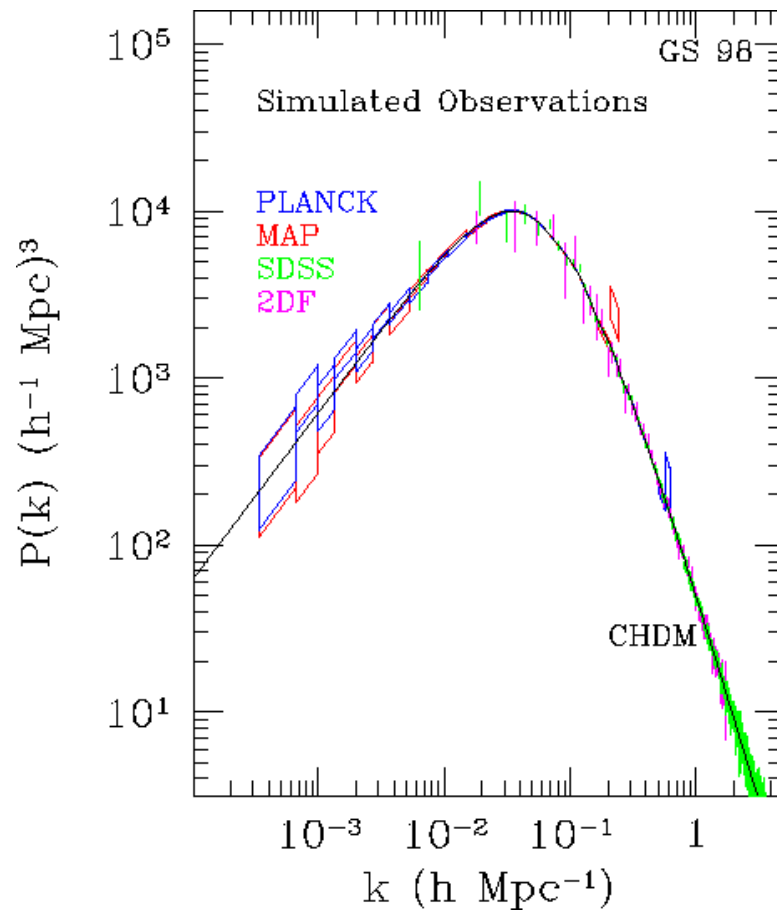


Figure 13.2: Simulation of high-precision future structure formation constraints. Simulated observations of CMB anisotropy are shown for the MAP (red boxes) and Planck Surveyor (blue boxes) satellites, under the assumption that CHDM is in fact the correct model of structure formation. Green error bars show accuracy of the Sloan Digital Sky Survey and magenta are for the 2 Degree Field Survey. All four data sets are indistinguishable from the underlying CHDM model for a wide range of k . No attempt has been made in this figure to account for redshift distortions or non-linear evolution, which will complicate observations at $k > 0.2$.

Bibliography

- Adelberger, K. L., Steidel, C. C., Giavalisco, M., Dickinson, M., Pettini, M., & Kellogg, M. 1998, *Astrophys. J.*, 505, 18
- Aghanim, N., De Luca, A., Bouchet, F. R., Gispert, R., & Puget, J. L. 1997, *Astron. Astrophys.*, 325, 9
- Aghanim, N., Desert, F. X., Puget, J. L., & Gispert, R. 1996, *Astron. Astrophys.*, 311, 1
- Aguirre, A. N. 1999a, *Astrophys. J., Lett.*, 512, L19
- . 1999b, preprint, astro-ph/9904319
- Albrecht, A., Battye, R. A., & Robinson, J. 1997, *Phys. Rev. Lett.*, 79, 4736
- Albrecht, A. & Steinhardt, P. J. 1982, *Phys. Rev. Lett.*, 48, 1220
- Alcock, C. et al. 1997, *Astrophys. J.*, 486, 697
- Aller, H. D., Aller, M. F., Latimer, G. E., & Hodge, P. E. 1985, *Astrophys. J., Suppl. Ser.*, 59, 513
- Amendola, L. & Borgani, S. 1994, *Mon. Not. R. Astron. Soc.*, 266, 191
- Andreani, P. & Franceschini, A. 1996, *Mon. Not. R. Astron. Soc.*, 283, 85
- Antonucci, R., Barvainis, R., & Alloin, D. 1990, *Astrophys. J.*, 353, 416
- Athanassopoulos, C. et al. 1996, *Phys. Rev. Lett.*, 77, 3082
- Avelino, P. P., Caldwell, R. R., & Martins, C. J. A. P. 1997, *Phys. Rev. D*, 56, 4568
- Baccigalupi, C., Amendola, L., & Occhionero, F. 1997, *Mon. Not. R. Astron. Soc.*, 288, 387
- Bahcall, J. N., Krastev, P. I., & Smirnov, A. Y. 1998, *Phys. Rev. D*, 58, 17710
- Bahcall, N. A., Fan, X., & Cen, R. 1997, *Astrophys. J., Lett.*, 485, L53
- Baker, J. C. et al. 1999, preprint, astro-ph/9904415
- Ballinger, W. E. 1997, PhD thesis, University of Edinburgh
- Banday, A. J., Gorski, K. M., Bennett, C. L., Hinshaw, G., Kogut, A., & Smoot, G. F. 1996, *Astrophys. J., Lett.*, 468, L85
- Barger, A. J., Cowie, L. L., Sanders, D. B., Fulton, E., Taniguchi, Y., Sato, Y., Kawara, K., & Okuda, H. 1998, *Nature*, 394, 248

- Barger, A. J., Cowie, L. L., Smail, I., Ivison, R. J., Blain, A. W., & Kneib, J.-P. 1999, *Astron. J.*, 117, 2656
- Bartelmann, M., Huss, A., Colberg, J. M., Jenkins, A., & Pearce, F. R. 1998, *Astron. Astrophys.*, 330, 1
- Bartlett, J. G., Douspis, M., Blanchard, A., & Le Dour, M. 1999, preprint, astro-ph/9903045
- Battye, R. A., Robinson, J., & Albrecht, A. 1998, *Phys. Rev. Lett.*, 80, 4847
- Baugh, C. M. & Efstathiou, G. 1993, *Mon. Not. R. Astron. Soc.*, 265, 145
- Beichman, C. A. & Helou, G. 1991, *Astrophys. J., Lett.*, 370, L1
- Beichman, C. A., Neugebauer, G., Soifer, B. T., Wootten, H. A., Roellig, T., & Harvey, P. M. 1981, *Nature*, 293, 711
- Bennett, C. L., Banday, A. J., Gorski, K. M., Hinshaw, G., Jackson, P., Keegstra, P., Kogut, A., Smoot, G. F., Wilkinson, D. T., & Wright, E. L. 1996, *Astrophys. J., Lett.*, 464, L1
- Bennett, C. L. et al. 1992, *Astrophys. J., Lett.*, 396, L7
- Blain, A. W., Ivison, R. J., & Smail, I. 1998a, *Mon. Not. R. Astron. Soc.*, 296, L29
- Blain, A. W., Ivison, R. J., Smail, I., & Kneib, J. P. 1998b, in *Wide-field surveys in cosmology*, Proc. XIV IAP meeting, astro-ph/9806063
- Block, D. L., Witt, A. N., Grosbol, P., Stockton, A., & Moneti, A. 1994, *Astron. Astrophys.*, 288, 383
- Boettcher, M., Reuter, H. P., & Lesch, H. 1997, *Astron. Astrophys.*, 326, L33
- Bond, J. R., Efstathiou, G., & Silk, J. 1980, *Phys. Rev. Lett.*, 45, 1980
- Bond, J. R., Efstathiou, G., & Tegmark, M. 1997, *Mon. Not. R. Astron. Soc.*, 291, L33
- Bond, J. R. & Jaffe, A. H. 1997, in *Proceedings of XXXIth Moriond Meeting, "Microwave Background Anisotropies"*
- Bond, J. R., Jaffe, A. H., & Knox, L. 1998, preprint, astro-ph/9808264
- Bond, J. R. & Myers, S. T. 1996, *Astrophys. J., Suppl. Ser.*, 103, 63
- Bouchet, F. R. & Gispert, R. 1999, *New Ast.*, 4, 443
- Bouchet, F. R., Prunet, S., & Sethi, S. 1999, *Mon. Not. R. Astron. Soc.*, 302, 663
- Bouchet, F. R. et al. 1994, in *proceedings of the meeting "Far Infrared and Sub-Millimeter Space Missions in the Next Decade"*, Paris, France, ed. M. Sauvage (*Space Science Review*)
- Boughn, S. P. 1998, preprint, astro-ph/9807308
- Branch, D. 1998, *Ann. Rev. Astron. Astrophys.*, 36, 17
- Brandt, W. N., Lawrence, C. R., Readhead, A. C. S., Pakianathan, J. N., & Fiola, T. M. 1994, *Astrophys. J.*, 424, 1

- Bromley, B. C. & Tegmark, M. 1999, *Astrophys. J., Lett.*, 524, L79
- Brustein, R. & Hadad, M. 1999, *Phys. Rev. Lett.*, 82, 3016
- Bunn, E. F., Fisher, K. B., Hoffman, Y., Lahav, O., Silk, J., & Zaroubi, S. 1994, *Astrophys. J., Lett.*, 432, L75
- Bunn, E. F. & White, M. 1997, *Astrophys. J.*, 480, 6
- Burigana, C. & Popa, L. 1998, *Astron. Astrophys.*, 334, 420
- Caldwell, R. R., Dave, R., & Steinhardt, P. J. 1998, *Phys. Rev. Lett.*, 80, 1586
- Carlberg, R. G., Morris, S. L., Yee, H. K. C., & Ellingson, E. 1997, *Astrophys. J., Lett.*, 479, L19
- Carlstrom, J. 1998, priv. communication
- Carroll, S. M., Press, W. H., & Turner, E. L. 1992, *Ann. Rev. Astron. Astrophys.*, 30, 499
- Cayon, L., Martinez-Gonzalez, E., & Sanz, J. L. 1993, *Astrophys. J.*, 403, 471
- . 1994, *Astron. Astrophys.*, 284, 719
- Cen, R. & Ostriker, J. P. 1999, *Astrophys. J.*, 514, 1
- Chaboyer, B., Demarque, P., Kernan, P. J., & Krauss, L. M. 1998, *Astrophys. J.*, 494, 96
- Chandler. 1995, vLA Memo #192
- Chiba, M. & Yoshii, Y. 1997, *Astrophys. J.*, 489, 485
- . 1999, *Astrophys. J.*, 510, 42
- Chiba, T., Sugiyama, N., & Nakamura, T. 1998, *Mon. Not. R. Astron. Soc.*, 301, 72
- Chini, R., Biermann, P. L., Kreysa, E., & Gemuend, H.-P. 1989, *Astron. Astrophys.*, 221, L3
- Chini, R. & Kruegel, E. 1993, *Astron. Astrophys.*, 279, 385
- Chini, R., Kruegel, E., Lemke, R., & Ward-Thompson, D. 1995, *Astron. Astrophys.*, 295, 317
- Chiu, W. A., Ostriker, J. P., & Strauss, M. A. 1998, *Astrophys. J.*, 494, 479
- Choi, E. & Ryu, D. 1998, *Mon. Not. R. Astron. Soc.*, 296, 109
- Church, S. E., Ganga, K. M., Ade, P. A. R., Holzapfel, W. L., Mauskopf, P. D., Wilbanks, T. M., & Lange, A. E. 1997, *Astrophys. J.*, 484, 523
- Coble, K., Dodelson, S., & Frieman, J. A. 1997, *Phys. Rev. D*, 55, 1851
- Coble, K. et al. 1999, preprint, astro-ph/9902195
- Colafrancesco, S., Mazzotta, P., & Vittorio, N. 1997, *Astrophys. J.*, 488, 566
- Condon, J. J. 1974, *Astrophys. J.*, 188, 279
- Condon, J. J. & Broderick, J. J. 1991, *Astron. J.*, 102, 1663

- Cooray, A. R. 1999, *Astron. Astrophys.*, 348, 31
- Copeland, E. J., Grivell, I. J., & Liddle, A. R. 1998, *Mon. Not. R. Astron. Soc.*, 298, 1233
- Crawford, T., Marr, J., Partridge, B., & Strauss, M. A. 1996, *Astrophys. J.*, 460, 225
- Croft, R. A. C., Hu, W., & Dave, R. 1999a, *Phys. Rev. Lett.*, 83, 1092
- Croft, R. A. C., Weinberg, D. H., Katz, N., & Hernquist, L. 1998, *Astrophys. J.*, 495, 44
- Croft, R. A. C., Weinberg, D. H., Pettini, M., Hernquist, L., & Katz, N. 1999b, *Astrophys. J.*, 520, 1
- Da Costa, L. N., Vogeley, M. S., Geller, M. J., Huchra, J. P., & Park, C. 1994, *Astrophys. J., Lett.*, 437, L1
- Davies, R. D., Watson, R. A., & Gutierrez, C. M. 1996, *Mon. Not. R. Astron. Soc.*, 278, 925
- Davis, M., Efstathiou, G., Frenk, C. S., & White, S. D. M. 1985, *Astrophys. J.*, 292, 371
- Davis, M., Summers, F. J., & Schlegel, D. 1992, *Nature*, 359, 393
- de Bernardis, P. & Masi, S. 1998, in "Fundamental parameters in Cosmology", *Rencontres de Moriond*, astro-ph/9804138
- de Oliveira-Costa, A., Kogut, A., Devlin, M. J., Netterfield, C. B., Page, L. A., & Wollack, E. J. 1997, *Astrophys. J., Lett.*, 482, L17
- de Oliveira-Costa, A. et al. 1999, *Astrophys. J., Lett.*, 527, L9
- Devereux, N. A. & Young, J. S. 1992, *Astron. J.*, 103, 1536
- Dodelson, S. 1997, *Astrophys. J.*, 482, 577
- Dodelson, S., Gates, E., & Stebbins, A. 1996, *Astrophys. J.*, 467, 10
- Dodelson, S., Gates, E., & Turner, M. S. 1996, *Science*, 274, 69
- Dodelson, S. & Kosowsky, A. 1995, *Phys. Rev. Lett.*, 75, 604
- Dodelson, S., Kosowsky, A., & Myers, S. T. 1995, *Astrophys. J., Lett.*, 440, L37
- Dodelson, S. & Stebbins, A. 1994, *Astrophys. J.*, 433, 440
- Draine, B. T. & Lazarian, A. 1998a, *Astrophys. J., Lett.*, 494, L19
- . 1998b, *Astrophys. J.*, 508, 157
- . 1999, *Astrophys. J.*, 512, 740
- Eales, S. et al. 1998, preprint, astro-ph/9808040
- Eales, S. A., Wynn-Williams, C. G., & Duncan, W. D. 1989, *Astrophys. J.*, 339, 859
- Ebeling, H., Voges, W., Bohringer, H., Edge, A. C., Huchra, J. P., & Briel, U. G. 1996, *Mon. Not. R. Astron. Soc.*, 281, 799

- Edelson, R. A. 1987, *Astron. J.*, 94, 1150
- Efstathiou, G., Bond, J. R., & White, S. D. M. 1992, *Mon. Not. R. Astron. Soc.*, 258, 1P
- Einasto, J., Einasto, M., Gottloeber, S., Mueller, V., Saar, V., Starobinsky, A. A., Tago, E., Tucker, D., Andernach, H., & Frisch, P. 1997, *Nature*, 385, 139
- Eisenstein, D. J., Hu, W., Silk, J., & Szalay, A. S. 1998a, *Astrophys. J., Lett.*, 494, L1
- Eisenstein, D. J., Hu, W., & Tegmark, M. 1998b, *Astrophys. J., Lett.*, 504, L57
- Evrard, A. E. 1997, *Mon. Not. R. Astron. Soc.*, 292, 289
- Fan, X., Bahcall, N. A., & Cen, R. 1997, *Astrophys. J., Lett.*, 490, L123
- Ferreira, P. G. & Joyce, M. 1998, *Phys. Rev. D*, 58, 05bcf
- Ferreira, P. G. & Magueijo, J. 1997, *Phys. Rev. D*, 55, 3358
- Ferreira, P. G., Magueijo, J., & Gorski, K. M. 1998, *Astrophys. J., Lett.*, 503, L1
- Ferreira, P. G., Magueijo, J., & Silk, J. 1997, *Phys. Rev. D*, 56, 4592
- Finkbeiner, D. P. 1999, PhD thesis, U.C. Berkeley
- Finkbeiner, D. P., Davis, M., & Schlegel, D. 1999, *Astrophys. J.*, 524, 867
- Fisher, K. B., Huchra, J. P., Strauss, M. A., Davis, M., Yahil, A., & Schlegel, D. 1995, *Astrophys. J., Suppl. Ser.*, 100, 69
- Fixsen, D. J., Dwek, E., Mather, J. C., Bennett, C. L., & Shafer, R. A. 1998, *Astrophys. J.*, 508, 123
- Fomalont, E. B., Kellermann, K. I., Richards, E. A., Windhorst, R. A., & Patridge, R. B. 1997, *Astrophys. J., Lett.*, 475, L5
- Franceschini, A. & Andreani, P. 1995, *Astrophys. J., Lett.*, 440, L5
- Franceschini, A., Toffolatti, L., Danese, L., & De Zotti, G. 1989, *Astrophys. J.*, 344, 35
- Frayer, D. T., Ivison, R. J., Scoville, N. Z., Yun, M., Evans, A. S., Smail, I., Blain, A. W., & Kneib, J. P. 1998, *Astrophys. J., Lett.*, 506, L7
- Fukuda, Y. et al. 1998, *Phys. Rev. Lett.*, 81, 1562
- Ganga, K., Page, L., Cheng, E., & Meyer, S. 1994, *Astrophys. J., Lett.*, 432, L15
- Gardner, J. P., Katz, N., Weinberg, D. H., & Hernquist, L. 1997, *Astrophys. J.*, 486, 42
- Garnavich, P. M. et al. 1998, *Astrophys. J., Lett.*, 493, L53
- Gawiser, E. 1998a, American Astronomical Society Meeting, 193, 10902
- Gawiser, E. 1998b, in *Proc. of 18th Texas Symp. on Relativistic Astrophysics*, Chicago, December 1996, ed. A. Olinto, J. Frieman, & D. N. Schramm (Singapore: World Scientific), 285

- Gawiser, E., Finkbeiner, D., Jaffe, A., Baker, J. C., Balbi, A., Davis, M., Hanany, S., Holzzapfel, W., Krumholz, M., Moustakas, L., Robinson, J., Scannapieco, E., Smoot, G. F., & Silk, J. 1998, astro-ph/9812237
- Gawiser, E., Jaffe, A., & Silk, J. 1998, preprint, astro-ph/9811148
- Gawiser, E. & Silk, J. 1998, *Science*, 280, 1405
- Gawiser, E. & Smoot, G. F. 1997, *Astrophys. J., Lett.*, 480, L1
- Gawiser, E., Sokasian, A., & Smoot, G. F. 1999, in preparation
- Gaztañaga, E. & Baugh, C. M. 1998, *Mon. Not. R. Astron. Soc.*, 294, 229
- Gaztañaga, E., Fosalba, P., & Elizalde, E. 1998, *Mon. Not. R. Astron. Soc.*, 295, L35
- Gear, W. K. et al. 1994, *Mon. Not. R. Astron. Soc.*, 267, 167
- Gialvalisco, M., Steidel, C. C., Adelberger, K. L., Dickinson, M. E., Pettini, M., & Kellogg, M. 1998, *Astrophys. J.*, 503, 543
- Goldberg, D. M. & Strauss, M. A. 1998, *Astrophys. J.*, 495, 29
- Gramann, M. 1998, *Astrophys. J.*, 493, 28
- Grewing, M. 1997, in *Proceedings of the ESA Symposium 'The Far Infrared and Submillimeter Universe'*, 15-17 April 1997, Grenoble, France, 219
- Griffith, M. R. & Wright, A. E. 1993, *Astron. J.*, 105, 1666
- Griffith, M. R., Wright, A. E., Burke, B. F., & Ekers, R. D. 1994, *Astrophys. J., Suppl. Ser.*, 90, 179
- . 1995, *Astrophys. J., Suppl. Ser.*, 97, 347
- Gruzinov, A. & Hu, W. 1998, *Astrophys. J.*, 508, 435
- Guiderdoni, B., Hivon, E., Bouchet, F. R., & Maffei, B. 1998, *Mon. Not. R. Astron. Soc.*, 295, 877
- Gundersen, J. O. et al. 1995, *Astrophys. J., Lett.*, 443, L57
- Guth, A. 1981, *Phys. Rev. D*, 23, 347
- Gutierrez, C. M., Hancock, S., Davies, R. D., Rebolo, R., Watson, R. A., Hoyland, R. J., Lasenby, A. N., & Jones, A. W. 1997, *Astrophys. J., Lett.*, 480, L83
- Haehnelt, M. G., Steinmetz, M., & Rauch, M. 1998, *Astrophys. J.*, 495, 647
- Haffner, L. M., Reynolds, R. J., & Tufte, S. L. 1998, *Astrophys. J., Lett.*, 501, L83
- Haimann, Z. & Knox, L. 1999, in *Microwave Foregrounds*, ed. A. de Oliveira-Costa & M. Tegmark (San Francisco: ASP), astro-ph/9902311
- Halpern, M. & Scott, D. 1999, in *Microwave Foregrounds*, ed. A. de Oliveira-Costa & M. Tegmark (San Francisco: ASP), astro-ph/9904188
- Hanany, S. et al. 1997, in *Proceedings of the 18th Texas Symposium on Relativistic Astrophysics*, astro-ph/9702200

- Hancock, S., Gutierrez, C. M., Davies, R. D., Lasenby, A. N., Rocha, G., Rebolo, R., Watson, R. A., & Tegmark, M. 1997, *Mon. Not. R. Astron. Soc.*, 289, 505
- Harrison, E. R. 1970, *Phys. Rev. D*, 1, 2726
- Haslam, C. G. T., Stoffel, H., Salter, C. J., & Wilson, W. E. 1982, *Astron. Astrophys. Suppl. Ser.*, 47, 1
- Hauser, M. G. et al. 1998, *Astrophys. J.*, 508, 25
- Herbig, T. & Readhead, A. C. S. 1992, *Astrophys. J., Suppl. Ser.*, 81, 83
- Hobson, M. P., Jones, A. W., Lasenby, A. N., & Bouchet, F. R. 1998, *Mon. Not. R. Astron. Soc.*, 300, 1
- Hobson, M. P. et al. 1998, *Mon. Not. R. Astron. Soc.*, 306, 232
- Holdaway, M. A., Owen, F. N., & Rupen, M. P. 1994, nRAO Report, MMA Memo #123
- Holder, G. P. & Carlstrom, J. E. 1999, in *Microwave Foregrounds*, ed. A. de Oliveira Costa & M. Tegmark (San Francisco: ASP), astro-ph/9904220
- Holzappel, W. 1998, priv. communication
- Hu, W. 1995, PhD thesis, U. C. Berkeley, astro-ph/9508126
- Hu, W. 1998, *Astrophys. J.*, 506, 485
- Hu, W., Eisenstein, D. J., & Tegmark, M. 1998, *Phys. Rev. Lett.*, 80, 5255
- Hu, W., Eisenstein, D. J., Tegmark, M., & White, M. 1999, *Phys. Rev. D*, 59, 05bd8
- Hu, W., Scott, D., & Silk, J. 1994, *Astrophys. J., Lett.*, 430, L5
- Hu, W. & White, M. 1997a, *New Astronomy*, 2, 323
- . 1997b, *Astrophys. J.*, 479, 568
- Hughes, D. H. et al. 1998, *Nature*, 394, 241
- Hui, L. 1998, preprint, astro-ph/9807068
- Iverson, R. J., Smail, I., Le Borgne, J. F., Blain, A. W., Kneib, J. P., Bezecourt, J., Kerr, T. H., & Davies, J. K. 1998, *Mon. Not. R. Astron. Soc.*, 298, 583
- Jaffe, A., Finkbeiner, D. P., & Bond, J. R. 1999a, in preparation
- Jaffe, A., Gawiser, E., Finkbeiner, D., Baker, J. C., Balbi, A., Davis, M., Hanany, S., Holzappel, W., Krumholz, M., Moustakas, L., Robinson, J., Scannapieco, E., Smoot, G. F., & Silk, J. 1999b, in *Microwave Foregrounds*, ed. A. de Oliveira Costa & M. Tegmark (San Francisco: ASP), astro-ph/9903248
- Jaffe, A. H. & Kamionkowski, M. 1998, *Phys. Rev. D*, 58, 7f9
- Jewell, J., Lawrence, C. R., & Levin, S. 1999, in *Microwave Foregrounds*, ed. A. de Oliveira-Costa & M. Tegmark (San Francisco: ASP), astro-ph/9903201

- Jing, Y. P., Mo, H. J., & Boerner, G. 1998, *Astrophys. J.*, 494, 1
- Jonas, J. L., Baart, E. E., & Nicolson, G. D. 1998, *Mon. Not. R. Astron. Soc.*, 297, 977
- Jones, A. W., Hobson, M. P., & Lasenby, A. N. 1998, preprint, astro-ph/9810236
- Jungman, G., Kamionkowski, M., Kosowsky, A., & Spergel, D. N. 1996, *Phys. Rev. D*, 54, 1332
- Kaiser, N. 1984, *Astrophys. J., Lett.*, 284, L9
- . 1987, *Mon. Not. R. Astron. Soc.*, 227, 1
- Kamionkowski, M. & Kosowsky, A. 1998, *Phys. Rev. D*, 57, 685
- Kamionkowski, M., Kosowsky, A., & Stebbins, A. 1997, *Physical Review Letters*, 78, 2058
- Kantowski, R. 1998, *Astrophys. J.*, 507, 483
- Kauffmann, G., Nusser, A., & Steinmetz, M. 1997, *Mon. Not. R. Astron. Soc.*, 286, 795
- Klypin, A., Holtzman, J., Primack, J., & Regos, E. 1993, *Astrophys. J.*, 416, 1
- Klypin, A., Primack, J., & Holtzman, J. 1996, *Astrophys. J.*, 466, 13
- Knapp, G. R. & Patten, B. M. 1991, *Astron. J.*, 101, 1609
- Knox, L. 1999a, *Phys. Rev. D*, 60, 103516
- . 1999b, *Mon. Not. R. Astron. Soc.*, 307, 977
- Knox, L., Scoccimarro, R., & Dodelson, S. 1998, *Phys. Rev. Lett.*, 81, 2004
- Kochanek, C. S. 1996, *Astrophys. J.*, 466, 638
- Kogut, A., Banday, A. J., Bennett, C. L., Gorski, K. M., Hinshaw, G., Smoot, G. F., & Wright, E. I. 1996b, *Astrophys. J., Lett.*, 464, L5
- Kogut, A., Banday, A. J., Bennett, C. L., Gorski, K. M., Hinshaw, G., Smoot, G. F., & Wright, E. L. 1996a, *Astrophys. J., Lett.*, 464, L29
- Kogut, A., Banday, A. J., Bennett, C. L., Hinshaw, G., Loewenstein, K., Lubin, P., Smoot, G. F., & Wright, E. L. 1994, *Astrophys. J.*, 433, 435
- Kolatt, T. & Dekel, A. 1997, *Astrophys. J.*, 479, 592
- Kolb, E. W. & Turner, M. S. 1990, *The Early Universe* (Reading, MA: Addison-Wesley Publishing Company)
- Kosowsky, A. & Turner, M. S. 1995, *Phys. Rev. D*, 52, 1739
- Kosowsky, A. B. 1994, PhD thesis, Univ. of Chicago
- Kreysa, E. 1998, priv. communication
- Landau, R., Epstein, E. E., & Rather, J. D. G. 1980, *Astron. J.*, 85, 363
- Landau, R. et al. 1983, *Astrophys. J.*, 268, 68

- . 1986, *Astrophys. J.*, 308, 78
- Landy, S. D., Shectman, S. A., Lin, H., Kirshner, R. P., Oemler, A. A., & Tucker, D. 1996, *Astrophys. J., Lett.*, 456, L1
- Landy, S. D., Szalay, A. S., & Broadhurst, T. J. 1998, *Astrophys. J., Lett.*, 494, L133
- Lawrence, A., Rowan-Robinson, M., Efstathiou, A., Ward, M. J., Elvis, M., Smith, M. G., Duncan, W. D., & Robson, E. I. 1991, *Mon. Not. R. Astron. Soc.*, 248, 91
- Lee, A. T. et al. 1999, in proceedings of "3K Cosmology", ed. F. Melchiorri, astro-ph/9903249
- Leitch, E. 1997, PhD thesis, Caltech
- Leitch, E. M., Readhead, A. C. S., Pearson, T. J., & Myers, S. T. 1997, *Astrophys. J., Lett.*, 486, L23
- Leitch, E. M. et al. 1998, *Astrophys. J.*, 518
- Lesgourgues, J., Polarski, D., & Starobinsky, A. A. 1998, *Mon. Not. R. Astron. Soc.*, 297, 769
- Lewis, G. F., Chapman, S. C., Ibata, R. A., Irwin, M. J., & Totten, E. J. 1998, *Astrophys. J., Lett.*, 505, L1
- Liddle, A. R., Lyth, D. H., Roberts, D., & Viana, P. T. P. 1996a, *Mon. Not. R. Astron. Soc.*, 278, 644
- Liddle, A. R., Lyth, D. H., Schaefer, R. K., Shafi, Q., & Viana, P. T. P. 1996b, *Mon. Not. R. Astron. Soc.*, 281, 531
- Liddle, A. R., Lyth, D. H., Viana, P. T. P., & White, M. 1996c, *Mon. Not. R. Astron. Soc.*, 282, 281
- Lim, M. A. et al. 1996, *Astrophys. J., Lett.*, 469, L69
- Lin, H., Kirshner, R. P., Shectman, S. A., Landy, S. D., Oemler, A., Tucker, D. L., & Schechter, P. L. 1996, *Astrophys. J.*, 471, 617
- Linde, A. D. 1982, *Phy. Lett.*, B108, 389
- Lineweaver, C. H. & Barbosa, D. 1998, *Astrophys. J.*, 496, 624
- Loeb, A. 1996, *Astrophys. J., Lett.*, 471, L1
- Ma, C. P., Bertschinger, E., Hernquist, L., Weinberg, D. H., & Katz, N. 1997, *Astrophys. J., Lett.*, 484, L1
- Mann, R. G., Peacock, J. A., & Heavens, A. F. 1998, *Mon. Not. R. Astron. Soc.*, 293, 209
- Marcelin, M., Amram, P., Bartlett, J. G., Valls-Gabaud, D., & Blanchard, A. 1998, *Astron. Astrophys.*, 338, 1
- Martinez-Gonzalez, E., Sanz, J. L., & Cayon, L. 1997, *Astrophys. J.*, 484, 1
- Masi, S., De Bernardis, P., De Petris, M., Gervasi, M., Boscaleri, A., Aquilini, E., Martinis, L., & Scaramuzzi, F. 1996, *Astrophys. J., Lett.*, 463, L47
- Mather, J. C. et al. 1994, *Astrophys. J.*, 420, 439

- McCullough, P. R. et al. 1999, in *Microwave Foregrounds*, ed. A. de Oliveira-Costa & M. Tegmark (San Francisco: ASP), astro-ph/9902248
- Meiksin, A., White, M., & Peacock, J. 1999, *Mon. Not. R. Astron. Soc.*, 304, 851
- Metcalf, R. B. & Silk, J. 1997, *Astrophys. J.*, 489, 1
- 1998, *Astrophys. J., Lett.*, 492, L1
- Moffat, J. W. & Tatarski, D. C. 1995, *Astrophys. J.*, 453, 17
- Nartallo, R., Gear, W. K., Murray, A. G., Robson, E. I., & Hough, J. H. 1998, *Mon. Not. R. Astron. Soc.*, 297, 667
- Neininger, N. & Guélin, M. 1996, in proceedings of the "Dust-Morphology" Conference, Johannesburg, 22-26 January 1996, ed. D. Block (Kluwer Dordrecht), astro-ph/9603005
- Netterfield, C. B., Devlin, M. J., Jarosik, N., Page, L., & Wollack, E. J. 1997, *Astrophys. J.*, 474, 47
- Odenwald, S., Newmark, J., & Smoot, G. 1998, *Astrophys. J.*, 500, 554
- Oh, S. P., Spergel, D. N., & Hinshaw, G. 1999, *Astrophys. J.*, 510, 551
- Owen, F. N., Porcas, R. W., Mufson, S. L., & Moffett, T. J. 1978, *Astron. J.*, 83, 685
- Owen, F. N., Spanger, S. R., & Cotton, W. D. 1980, *Astron. J.*, 85, 351
- Padmanabhan, T. 1993, *Structure Formation in the Universe* (Cambridge, UK: Cambridge University Press)
- Pando, J., Valls-Gabaud, D., & Fang, L. Z. 1998, *Phys. Rev. Lett.*, 81, 4568
- Park, C., Vogeley, M. S., Geller, M. J., & Huchra, J. P. 1994, *Astrophys. J.*, 431, 569
- Partridge, R. B., Richards, E. A., Fomalont, E. B., Kellermann, K. I., & Windhorst, R. A. 1997, *Astrophys. J.*, 483, 38
- Patnaik, A. R., Browne, I. W. A., Wilkinson, P. N., & Wrobel, J. M. 1992, *Mon. Not. R. Astron. Soc.*, 254, 655
- Peacock, J. A. 1997, *Mon. Not. R. Astron. Soc.*, 284, 885
- Peacock, J. A. & Dodds, S. J. 1994, *Mon. Not. R. Astron. Soc.*, 267, 1020
- 1996, *Mon. Not. R. Astron. Soc.*, 280, L19
- Pearson, C. & Rowan-Robinson, M. 1996, *Mon. Not. R. Astron. Soc.*, 283, 174
- Peebles, P. J. E. 1993, *Principles of Physical Cosmology* (Princeton, NJ: Princeton University Press)
- Peebles, P. J. E. 1997, *Astrophys. J., Lett.*, 483, L1
- 1999a, *Astrophys. J.*, 510, 523
- 1999b, *Astrophys. J.*, 510, 531
- Peebles, P. J. E. & Juszkievicz, R. 1998, *Astrophys. J.*, 509, 483

- Peebles, P. J. E. & Yu, J. T. 1970, *Astrophys. J.*, 162, 815
- Penzias, A. A. & Wilson, R. W. 1965, *Astrophys. J.*, 142, 419
- Perley, R. A. 1982, *Astron. J.*, 87, 859
- Perlmutter, S. et al. 1998, *Nature*, 391, 51
- Persi, F. M., Spergel, D. N., Cen, R., & Ostriker, J. P. 1995, *Astrophys. J.*, 442, 1
- Phillips, T. G. 1997, in *Proceedings of the ESA Symposium 'The Far Infrared and Submillimeter Universe'*, 15-17 April 1997, Grenoble, France, 223
- Platania, P., Bensadoun, M., Bersanelli, M., De Amici, G., Kogut, A., Levin, S., Maino, D., & Smoot, G. F. 1998, *Astrophys. J.*, 505, 473
- Platt, S. R., Kovac, J., Dragovan, M., Peterson, J. B., & Ruhl, J. E. 1997, *Astrophys. J., Lett.*, 475, L1
- Pogosyan, D. Y. & Starobinsky, A. A. 1993, *Mon. Not. R. Astron. Soc.*, 265, 507
- Primack, J. R. & Gross, M. A. K. 1998, in *Xth Rencontres de Blois, "The Birth of Galaxies"*, 28 June - 4 July 1998
- Primack, J. R., Holtzman, J., Klypin, A., & Caldwell, D. O. 1995, *Phys. Rev. Lett.*, 74, 2160
- Puget, J. L., Abergel, A., Bernard, J. P., Boulanger, F., Burton, W. B., Desert, F. X., & Hartmann, D. 1996, *Astron. Astrophys.*, 308, L5
- Reach, W. T. et al. 1995, *Astrophys. J.*, 451, 188
- Readhead, A. C. S., Lawrence, C. R., Myers, S. T., Sargent, W. L. W., Hardebeck, H. E., & Moffet, A. T. 1989, *Astrophys. J.*, 346, 566
- Refregier, A. 1999, in *Microwave Foregrounds*, ed. A. de Oliveira-Costa & M. Tegmark (San Francisco: ASP), astro-ph/9904235
- Refregier, A., Spergel, D. N., & Herbig, T. 1998, preprint, astro-ph/9806349
- Reich, P. & Reich, W. 1988, *Astron. Astrophys. Suppl. Ser.*, 74, 7
- Richards, E. A. 1999, *Astrophys. J., Lett.*, 513, L9
- Richards, E. A., Kellermann, K. I., Fomalont, E. B., Windhorst, R. A., & Partridge, R. B. 1998, *Astron. J.*, 116, 1039
- Riess, A. G. et al. 1998, *Astron. J.*, 116, 1009
- Robinson, J., Gawiser, E., & Silk, J. 1998, preprint, astro-ph/9805181
- . 1999, preprint, astro-ph/9906156
- Rowan-Robinson, M. 1992, *Mon. Not. R. Astron. Soc.*, 258, 787
- Scherrer, R. J. & Weinberg, D. H. 1998, *Astrophys. J.*, 504, 607
- Scheuer, P. A. G. 1957, *Proc. Camb. Phil. Soc.*, 53, 764

- Scheuer, P. A. G. 1974, *Mon. Not. R. Astron. Soc.*, 166, 329
- Schlegel, D. J., Finkbeiner, D. P., & Davis, M. 1998, *Astrophys. J.*, 500, 525
- Scott, D. 1998, in *Proceedings of the MPA/ESO Conference, "Evolution of Large-scale Structure: From Recombination to Garching"*, ed. A. J. Bandy et al., astro-ph/9810330
- Scott, D., Silk, J., & White, M. 1995, *Science*, 268, 829
- Scott, D., Srednicki, M., & White, M. 1994, *Astrophys. J., Lett.*, 421, L5
- Scott, D. & White, M. 1999, *Astron. Astrophys.*, 346, 1
- Scott, P. F. et al. 1996, *Astrophys. J., Lett.*, 461, L1
- Seljak, U. & Zaldarriaga, M. 1996, *Astrophys. J.*, 469, 437
- . 1997, *Phys. Rev. Lett.*, 78, 2054
- Seljak, U. & Zaldarriaga, M. 1999, *Phys. Rev. Lett.*, 82, 2636
- Shi, X. & Turner, M. S. 1998, *Astrophys. J.*, 493, 519
- Shi, X., Widrow, L. M., & Dursi, L. J. 1996, *Mon. Not. R. Astron. Soc.*, 281, 565
- Shu, F. H. 1991, *The Physics of Astrophysics, Volume I: Radiation* (Mill Valley, CA: University Science Books)
- Silk, J. 1967, *Nature*, 215, 1155
- Smail, I., Ivison, R. J., & Blain, A. W. 1997, *Astrophys. J., Lett.*, 490, L5
- Smail, I., Ivison, R. J., Blain, A. W., & Kneib, J. P. 1998, *Astrophys. J., Lett.*, 507, L21
- Smith, C. C., Klypin, A., Gross, M. A. K., Primack, J. R., & Holtzman, J. 1998, *Mon. Not. R. Astron. Soc.*, 297, 910
- Smoot, G. F. 1995, *Planet. Space Sci.*, 43, 1345
- Smoot, G. F. 1998, preprint, astro-ph/9801121
- Smoot, G. F., Bennett, C. L., Kogut, A., Wright, E. L., et al. 1992, *Astrophys. J., Lett.*, 396, L1
- Smoot, G. F. & Scott, D. 1998, in *Review of Particle Properties*, astro-ph/9711069
- Sokasian, A., Gawiser, E., & Smoot, G. F. 1998, preprint, astro-ph/9811311
- Souradeep, T., Bond, J. R., Knox, L., Efstathiou, G., & Turner, M. S. 1998, in *Proceedings of COSMO-97, Ambleside, England, September 1997*, ed. L. Roszkowski (World Scientific), astro-ph/9802262
- Spergel, D. N. 1998, priv. communication
- Stanghellini, C., O'Dea, C. P., Baum, S. A., Dallacasa, D., Fanti, R., & Fanti, C. 1997, *Astron. Astrophys.*, 325, 943

- Steidel, C. C., Adelberger, K. L., Dickinson, M., Giavalisco, M., Pettini, M., & Kellogg, M. 1998, *Astrophys. J.*, 492, 428
- Steigman, G., Hata, N., & Felten, J. E. 1999, *Astrophys. J.*, 510, 564
- Steppe, H., Jeyakumar, S., Saikia, D. J., & Salter, C. J. 1995, *Astron. Astrophys. Suppl. Ser.*, 113, 409
- Steppe, H., Liechti, S., Mauersberger, R., Koempe, C., Brunswig, W., & Ruiz-Moreno, M. 1992, *Astron. Astrophys. Suppl. Ser.*, 96, 441
- Steppe, H., Salter, C. J., Chini, R., Kreysa, E., Brunswig, W., & Lobato Perez, J. 1988, *Astron. Astrophys. Suppl. Ser.*, 75, 317
- Stevens, J. A., Robson, E. I., & Holland, W. S. 1996, *Astrophys. J., Lett.*, 462, L23
- Stirling, A. 1998, PhD thesis, University of Edinburgh
- Subrahmanyam, R., Ekers, R. D., Sinclair, M., & Silk, J. 1993, *Mon. Not. R. Astron. Soc.*, 263, 416
- Suginohara, M., Suginohara, T., & Spergel, D. N. 1998, *Astrophys. J.*, 495, 511
- Sugiyama, N. & Silk, J. 1999, in preparation
- Sunyaev, R. A. & Zeldovich, Y. B. 1972, *Astron. Astrophys.*, 20, 189
- Tadros, H. 1999, priv. communication
- Tadros, H., Efstathiou, G., & Dalton, G. 1998, *Mon. Not. R. Astron. Soc.*, 296, 995
- Tadros, H. et al. 1999, *Mon. Not. R. Astron. Soc.*, 305, 527
- Tan, J. C., Silk, J., & Balland, C. 1999, *Astrophys. J.*, 522, 579
- Tanaka, S. T. et al. 1996, *Astrophys. J., Lett.*, 468, L81
- Taylor, A. N. & Rowan-Robinson, M. 1992, *Nature*, 359, 396
- Tegmark, M. 1998, *Astrophys. J.*, 502, 1
- Tegmark, M. & De Oliveira-Costa, A. 1998, *Astrophys. J., Lett.*, 500, L83
- Tegmark, M. & Efstathiou, G. 1996, *Mon. Not. R. Astron. Soc.*, 281, 1297
- Tegmark, M. & Hamilton, A. 1997, preprint, astro-ph/9702019
- Tenorio, L., Jaffe, A. H., Hanany, S., & Lineweaver, C. H. 1999, preprint, astro-ph/9903206
- Toffolatti, L., Argueso Gomez, F., De Zotti, G., Mazzei, P., Franceschini, A., Danese, L., & Burigana, C. 1998, *Mon. Not. R. Astron. Soc.*, 297, 117
- Toffolatti, L. et al. 1995, in *Proc. of the Workshop "The cosmic microwave background"*, Capri(NA), 20-24 September 1993, *Astrophys. Lett. & Comm.*
- Tolman, R. C. 1934, *Relativity, Thermodynamics, and Cosmology* (Oxford, UK: Clarendon Press)

- Tornikoski, M., Valtaoja, E., Terasranta, H., Lainela, M., Bramwell, M., & Botti, L. C. L. 1993, *Astron. J.*, 105, 1680
- Tornikoski, M. et al. 1996, *Astron. Astrophys. Suppl. Ser.*, 116, 157
- Tucker, G. S., Griffin, G. S., Nguyen, H. T., & Peterson, J. B. 1993, *Astrophys. J., Lett.*, 419, L45
- Tucker, G. S., Gush, H. P., Halpern, M., Shinkoda, I., & Towlson, W. 1997, *Astrophys. J., Lett.*, 475, L73
- Turner, E. L., Cen, R., & Ostriker, J. P. 1992, *Astron. J.*, 103, 1427
- Turner, M. S. & White, M. 1997, *Phys. Rev. D*, 56, 4439
- Tytler, D., Fan, X. M., & Burles, S. 1996, *Nature*, 381, 207
- Urry, C. M. & Padovani, P. 1995, *Publ. Astron. Soc. Pac.*, 107, 803
- Valdarnini, R., Kahniashvili, T., & Novosyadlyj, B. 1998, *Astron. Astrophys.*, 336, 11
- Verschuur, G. L. & Kellerman, K. I., eds. *Galactic and Extragalactic Radio Astronomy*, 2nd edn. (New York: Springer-Verlag)
- Viana, P. T. P. & Liddle, A. R. 1996, *Mon. Not. R. Astron. Soc.*, 281, 323
- . 1998, *Phys. Rev. D*, 57, 674
- . 1999, *Mon. Not. R. Astron. Soc.*, 303, 535
- Vittorio, N. & Silk, J. 1992, *Astrophys. J., Lett.*, 385, L9
- VLA. 1995, vLA Memo #193
- . 1997, vLA Calibrator Manual, unpublished
- Wandelt, B., Hivon, E., & Górski, K. 1998, preprint, astro-ph/9808292
- Wang, B. 1991, *Astrophys. J.*, 374, 465
- Wang, Y., Spergel, D. N., & Strauss, M. A. 1999, *Astrophys. J.*, 510, 20
- Wang, Y., Spergel, D. N., & Turner, E. L. 1998, *Astrophys. J.*, 498, 1
- Webster, A. M., Bridle, S. L., Hobson, M. P., Lasenby, A. N., Lahav, O., & Rocha, G. 1998, *Astrophys. J., Lett.*, 509, L65
- Weinberg, S. 1972, *Gravitation and Cosmology* (New York: Wiley), (15.3.11, 15.3.20)
- White, M. 1998, *Phys. Rev. D*, 57, 5273
- White, M. & Bunn, E. 1995, *Astrophys. J., Lett.*, 443, L53
- White, M. & Scott, D. 1996, *Comments on Astrophysics*, 8
- White, M., Scott, D., & Silk, J. 1994, *Ann. Rev. Astron. Astrophys.*, 32, 319
- White, M., Scott, D., Silk, J., & Davis, M. 1995, *Mon. Not. R. Astron. Soc.*, 276, L69

- White, M. & Srednicki, M. 1995, *Astrophys. J.*, 443, 6
- White, M., Viana, P. T. P., Liddle, A. R., & Scott, D. 1996, *Mon. Not. R. Astron. Soc.*, 283, 107
- Wilner, D. J. & Wright, M. C. H. 1997, *Astrophys. J., Lett.*, 488, L67
- Wilson, G. W. et al. 1999, preprint, astro-ph/9902047
- Wiren, S., Valtaoja, E., Terasranta, H., & Kotilainen, J. 1992, *Astron. J.*, 104, 1009
- Wright, A. E., Griffith, M. R., Burke, B. F., & Ekers, R. D. 1994, *Astrophys. J., Suppl. Ser.*, 91, 111
- Wright, A. E., Griffith, M. R., Hunt, A. J., Troup, E., Burke, B. F., & Ekers, R. D. 1996, *Astrophys. J., Suppl. Ser.*, 103, 145
- Wu, X.-P., Qin, B. F., & Fang, L.-Z. 1996, *Astrophys. J.*, 469, 48
- Yamada, M., Sugiyama, N., & Silk, J. 1999, *Astrophys. J.*, 522, 66
- Zaldarriaga, M. & Seljak, U. 1997, *Phys. Rev. D*, 55, 1830
- Zaldarriaga, M. & Seljak, U. 1998, preprint, astro-ph/9810257
- Zaldarriaga, M., Seljak, U., & Bertschinger, E. 1998, *Astrophys. J.*, 494, 491
- Zaldarriaga, M., Spergel, D. N., & Seljak, U. 1997, *Astrophys. J.*, 488, 1
- Zaroubi, S., Zehavi, I., Dekel, A., Hoffman, Y., & Kolatt, T. 1997, *Astrophys. J.*, 486, 21
- Zehavi, I., Riess, A. G., Kirshner, R. P., & Dekel, A. 1998, *Astrophys. J.*, 503, 483
- Zeldovich, Y. B. 1972, *Mon. Not. R. Astron. Soc.*, 160, 1P